Fetal Cardiovascular Magnetic Resonance Imaging - Technical development and clinical utility

Ryd, Daniel

2022

Document Version:
Publisher's PDF, also known as Version of record

Link to publication

Citation for published version (APA):
Ryd, D. (2022). *Fetal Cardiovascular Magnetic Resonance Imaging - Technical development and clinical utility*. [Doctoral Thesis (compilation), Department of Clinical Sciences, Lund]. Lund University, Faculty of Medicine.

Total number of authors:
1

LUND UNIVERSITY

PO Box 117
221 00 Lund
+46 46-222 00 00

Fetal Cardiovascular Magnetic Resonance Imaging

Technical development and clinical utility

DANIEL RYD
DEPARTMENT OF CLINICAL PHYSIOLOGY | FACULTY OF MEDICINE | LUND UNIVERSITY

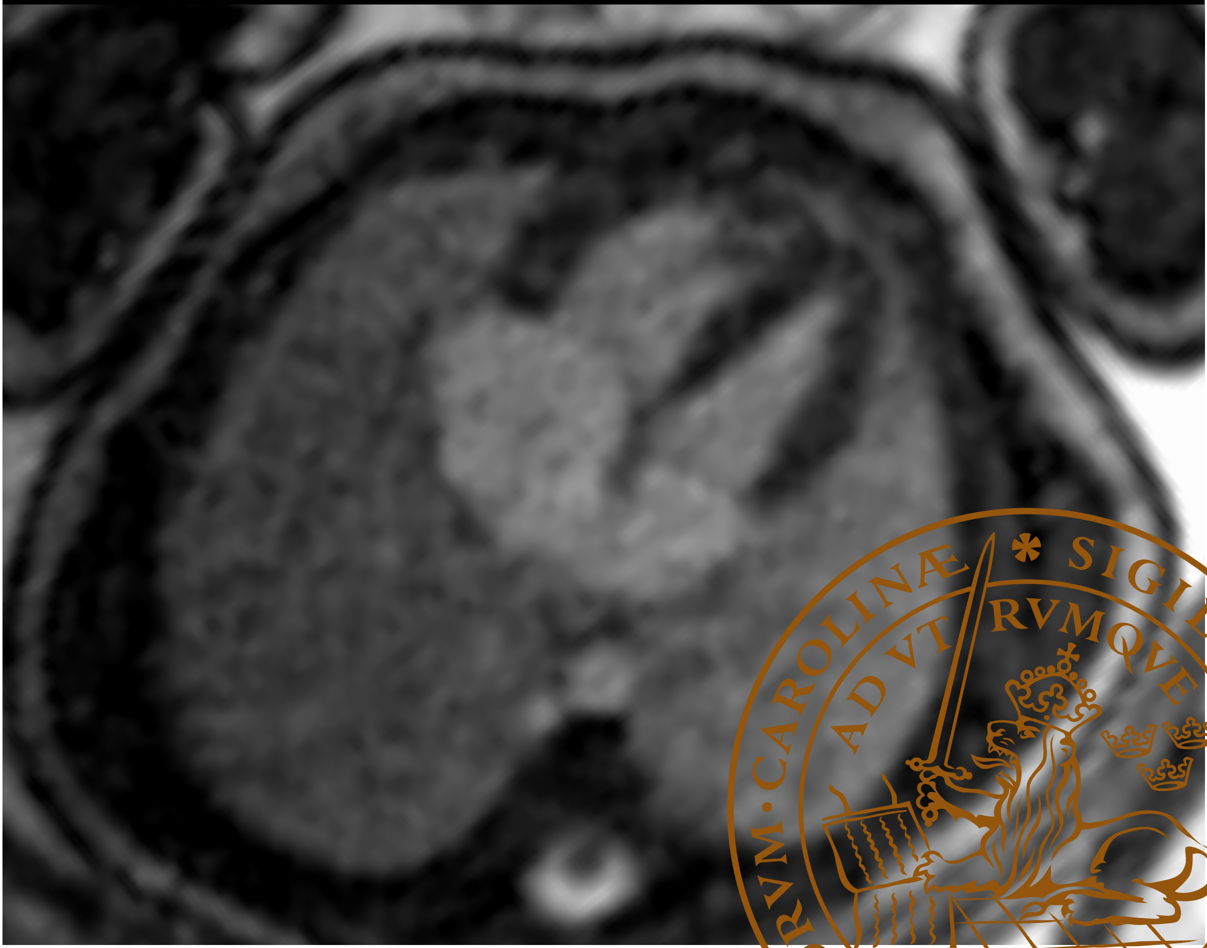

LUND UNIVERSITY

FACULTY OF MEDICINE

Department of Clinical Physiology

Lund University, Faculty of Medicine
Doctoral Dissertation Series 2022:51
ISBN 978-91-8021-212-0
ISSN 1652-8220

Printed by Media-Tryck, Lund 2021 NORDIC SWAN ECOLABEL 3041 0903

Fetal Cardiovascular Magnetic Resonance Imaging

Technical development and clinical utility

Fetal Cardiovascular Magnetic Resonance Imaging

Technical development and clinical utility

Daniel Ryd, M.D.

LUND
UNIVERSITY

Thesis for the degree of Doctor of Philosophy

Thesis advisors: Associate professor Erik Hedström, Associate professor Katarina Steding-Ehrenborg

Faculty opponent: Professor Vivek Muthurangu

To be presented, with the permission of the Faculty of Medicine at Lund University, for public criticism in the Lecture Hall 1 (Föreläsningssal 1) at Skåne University Hospital, Entrégatan 7, Lund, Sweden on Wednesday, 20th of April 2022 at 13:00.

Organization
LUND UNIVERSITY
Clinical Physiology Department of clinical sciences Lund

Document name
DOCTORAL DISSERTATION

Date of issue

Author(s)
Daniel Ryd

Sponsoring organization

Title and subtitle
Fetal Cardiovascular Magnetic Resonance Imaging - Technical development and clinical utility

Abstract

This thesis applied and developed new techniques in cardiovascular magnetic resonance (CMR) imaging for assessment of the fetal heart and circulation.

Study I evaluated phase-contrast quantitative flow measurements in the fetal descending aorta and umbilical vein using Doppler-ultrasound (DUS) gating. Fetal blood flow was also quantified using the previous reference method metric optimized gating (MOG) for comparison. Measurements by DUS gating and MOG were found to agree in general, although with significant variability. Intra- and interobserver variability were generally low for fetal blood flow measurements.

Study II applied artificial neural networks for automatic quantification of fetal volume using high-resolution magnetic resonance images. The agreement was good between automatic and manual measurements, and the automatic method typically saves 1 - 2 hours of analysis time per case. This makes fetal volume quantification using high-resolution magnetic resonance images clinically feasible. Fetal volume can be used to estimate fetal weight. Fetal weight estimation by magnetic resonance imaging can be used to index blood flow measurements for more accurate assessment of fetal physiology, and could potentially improve the detection of small and large for gestational age fetuses.

Study III investigated the clinical utility of fetal CMR for diagnosing congenital heart defects in fetuses where diagnostic questions remained after fetal ultrasound examination performed by a pediatric cardiologist. Fetal CMR added diagnostic information in the majority of cases, and showed a direct impact on patient management in selected cases.

Study IV applied artificial neural networks to increase resolution in low-resolution images with a reduced acquisition time. The proposed methods showed no statistically significant differences in image quality versus fully sampled images for up to three times accelerated image acquisition. A faster image acquisition reduces the risk of fetal movement, thereby increasing the chance of a successful examination.

Key words
Fetal cardiovascular magnetic resonance, Congenital heart disease, Magnetic resonance imaging

Classification system and/or index terms (if any)

Supplementary bibliographical information

Language

ISSN and key title
1652-8220

ISBN
978-91-8021-212-0

Recipient's notes

Number of pages

Price

Security classification

I, the undersigned, being the copyright owner of the abstract of the above-mentioned dissertation, hereby grant to all reference sources permission to publish and disseminate the abstract of the above-mentioned dissertation.

Signature ____ Date____________________

Fetal Cardiovascular Magnetic Resonance Imaging

Technical development and clinical utility

Daniel Ryd, M.D.

LUND
UNIVERSITY

Faculty Opponent

Professor Vivek Muthurangu
Institute of Cardiovascular Science
University College London
London, United Kingdom

Evaluation Committee

Associate professor Mats Mellander
Gothenburg University
Gothenburg, Sweden

Associate professor Kerstin Lagerstrand
Gothenburg University
Gothenburg, Sweden

Associate professor Elin Trägårdh
Lund University
Lund, Sweden

Cover: Magnetic resonance image of the fetal heart

Typeset in LaTeX

Faculty of Medicine, Department of Clinical Physiology
ISBN: 978-91-8021-212-0
ISSN: 1652-8220
Lund University, Faculty of Medicine Doctoral Dissertation Series 2022:51

Printed in Sweden by Media-Tryck, Lund University, Lund 2022

Printed matter
3041 0903

Media-Tryck is a Nordic Swan Ecolabel
certified provider of printed material.
Read more about our environmental
work at www.mediatryck.lu.se

MADE IN SWEDEN

Contents

I Research context

Appendix

II Research Papers

Author contributions

Papers

This thesis is based on the following papers:

I **Quantification of blood flow in the fetus with cardiovascular magnetic resonance imaging using Doppler ultrasound gating: validation against metric optimized gating**

Daniel Salehi, Liqun Sun, Katarina Steding-Ehrenborg, Sebastian Bidhult, Fabian Kording, Christian Ruprecht, Christopher K. Macgowan, Michael Seed, Anthony H. Aletras, Håkan Arheden, Erik Hedström

Journal of Cardiovascular Magnetic Resonance 21, 74 (2019). https://doi.org/10.1186/s12968-019-0586-8. © The Authors.

II **Automatic segmentation of the fetus in 3D magnetic resonance images using deep learning: Accurate and fast fetal volume quantification for clinical use**

Daniel Ryd, Amanda Nilsson, Einar Heiberg, Erik Hedström

Submitted manuscript

III **Utility of fetal cardiovascular magnetic resonance for prenatal diagnosis of complex congenital heart defects**

Daniel Ryd, Katrin Fricke, Misha Bhat, Håkan Arheden, Petru Liuba, Erik Hedström

JAMA Network Open. 2021;4(3):e213538. doi:10.1001/jamanetworkopen.2021.3538. © The Authors.

IV **Super-resolution cine image enhancement for fetal cardiac magnetic resonance imaging**

Klas Berggren, Daniel Ryd, Einar Heiberg, Anthony H. Aletras, Erik Hedström

Journal of Magnetic Resonance Imaging. 2021. https://doi.org/10.1002/jmri.27956. © The Authors.

Abbreviations

CMR cardiovascular magnetic resonance. 11, 24, 29, 30, 36, 38, 42, 49, 54–60, 65

CNN convolutional neural network. 20, 21

DAo descending aorta. 30, 31, 41, 42, 44, 45, 47

DUS Doppler ultrasound. 30, 32, 41–43, 45–48

MOG metric optimized gating. 30, 32, 41–43, 45, 46, 48

MR magnetic resonance. 4–6, 8–10, 12, 24, 30, 34, 36, 49, 50, 54

MRI magnetic resonance imaging. 4, 11, 12, 14, 24, 34, 52

RF radio frequency. 4

UV umbilical vein. 30, 31, 41, 42, 44, 45, 47

Popular summary

Pregnancy-related complications such as congenital heart defects, fetal growth restriction and preeclampsia cause significant fetal and neonatal mortality and morbidity. Treatment of these conditions have improved significantly over the last decades and include surgery for congenital heart defects, careful delivery planning and neonatal intensive care. In order to provide the best possible care for the patients, a prenatal diagnosis can be crucial. In Sweden, all pregnant women are offered fetal ultrasound screening. While fetal ultrasound will provide a diagnosis in the majority of cases, ultrasound may be unable to clearly visualize fetal anatomy, particularly in late pregnancy or obese pregnant women. Therefore, there is a need for improved diagnostic methods to improve the management of complicated pregnancies.

Cardiovascular magnetic resonance imaging (CMR) is considered to be the gold standard method for measuring cardiac volumes and blood flow in adults and children, and could potentially overcome the limitations of fetal ultrasound imaging. However, CMR requires a synchronization of acquired image data and the cardiac rhythm for optimal image quality. In adults and children, this is usually achieved by recording an electrocardiogram during image acquisition. In fetuses however, an electrocardiogram of sufficient quality for CMR is not available, which has limited the usefulness of CMR for fetal examinations. In recent years, a new method for recording the fetal heart rhythm using a magnetic resonance compatible ultrasound device has been developed. This has enabled imaging of the fetal heart and measurements of blood flow in fetal vessels using state-of-the-art CMR techniques. The overall aim of this thesis was to apply and develop new methods in fetal CMR for assessment of the fetal heart and circulation.

Paper I evaluated a new method for quantifying blood flow in fetal blood vessels using CMR. This new method was found to be feasible and could potentially provide important insights into fetal disease mechanisms.

Paper II applied artificial neural networks to automatically measure fetal volume in high-resolution magnetic resonance images. The agreement between automatic and manual measurements was good and the automatic method typically saves 1-2 hours per case. Fetal volume can be used to estimate fetal weight, which is an important factor for accurate interpretation of blood flow measurements and for delivery planning.

Paper III investigated the clinical utility of fetal CMR in fetuses where ultrasound examination was unable to answer all diagnostic questions. Fetal CMR added diagnostic information in the majority of cases, and had a direct impact on patient management in some cases.

Paper IV applied artificial neural networks to increase resolution in fetal CMR images acquired with reduced resolution to shorten the image acquisition time. A shorter image acquisition time reduces the risk of fetal movement during image acquisition, which in turn increases the chance of a successful examination.

In summary, this work has applied and developed new methods for assessment of the fetal heart and circulation using fetal CMR. Fetal CMR had a direct impact on clinical decision-making in selected cases. Furthermore, this thesis evaluated a new method for measuring fetal blood flow using CMR, and a method for automatic fetal weight estimation based on high-resolution magnetic resonance images. Future research using these methods is warranted to increase the understanding of fetal physiology and further improve the diagnostic methods for complicated pregnancies.

Populärvetenskaplig sammanfattning

Graviditetsrelaterade komplikationer som medfödda hjärtfel, tillväxthämning hos fostret och havandeskapsförgiftning kan medföra allvarlig sjukdom eller död hos barnet. Behandlingen har förbättrats de senaste årtiondena och innefattar bland annat kirurgi för medfödda hjärtfel, noggrann förlossningsplanering samt neonatal intensivvård. En korrekt diagnos före förlossning kan vara avgörande. I Sverige erbjuds alla gravida kvinnor ultraljudsundersökning av fostret. Ultraljud ger i de flesta fall korrekt diagnos men det är i vissa fall inte möjligt att tydligt visualisera fostrets anatomi, särskilt i sen graviditet och hos överviktiga kvinnor. Det finns därför ett behov av förbättrade metoder för fosterdiagnostik.

Magnetisk resonanstomografi (MR) anses vara den icke-invasiva metod som med störst noggrannhet kan mäta hjärtvolymer och blodflöde hos barn och vuxna, och skulle kunna övervinna vissa begränsningar hos fosterultraljud. Vid hjärt-MR krävs synkronisering av insamlad bildinformation och hjärtats rytm för att få bra bildkvalitet. Detta görs vanligtvis genom att ett elektrokardiogram (EKG) registreras under bildtagning. Det är dock inte möjligt att registrera ett foster-EKG av tillräcklig kvalitet för hjärt-MR-undersökning, vilket har begränsat möjligheterna att undersöka fostrets hjärta och kärl med MR. På senare år har en ny metod för att registrera fostrets hjärtrytm vid MR-undersökning utvecklats. Denna metod bygger på en MR-kompatibel ultraljudsapparat som kan detektera fostrets hjärtslag. Detta har möjliggjort att undersöka fostrets hjärta och kärl med hjärt-MR-tekniker som rutinmässigt används hos barn och vuxna. Det övergripande målet med denna avhandling var att använda och utveckla nya tekniker inom hjärt-MR för att utvärdera fostrets hjärta och cirkulation.

Studie I utvärderade en ny metod för att mäta blodflöde i fosterkärl med hjärt-MR. Den nya metoden visade sig vara genomförbar och skulle kunna ge viktig kunskap om sjukdomsmekanismer hos foster.

Studie II applicerade artificiella neuronnät för att automatiskt mäta fostrets volym med hjälp av högupplösta MR-bilder. Överensstämmelsen mellan automatiska och manuella mätningar var god och den automatiska metoden sparar cirka 1 – 2 timmar per foster. Fostrets volym kan användas för att uppskatta fostrets vikt, vilket är en viktig faktor att ta hänsyn till både för att tolka blodflödesmätningar och för att planera förlossning.

Studie III undersökte den kliniska nyttan av fosterhjärt-MR för patienter där fosterultraljud inte kunde besvara alla diagnostiska frågeställningar. Fosterhjärt-MR tillförde diagnostisk information i en majoritet av patienterna, och hade en direkt påverkan på klinisk handläggning i vissa fall.

Studie IV applicerade artificiella neuronnät för att öka upplösningen i fosterhjärt-MR-bilder som samlats in med låg upplösning för att förkorta bildinsamlingstiden. En kortare bildinsamling minskar risken för fosterrörelser under bildinsamlingen, vilket i sin tur ökar chanserna för en framgångsrik undersökning.

Sammanfattningsvis har denna avhandling applicerat och utvecklat nya metoder för att utvärdera fostrets hjärta och cirkulation med hjälp av fosterhjärt-MR. Fosterhjärt-MR hade en direkt påverkan på klinisk handläggning i utvalda fall. Denna avhandling utvärderade en ny metod för att mäta blodflöde i fosterkärl, och en metod för att automatiskt uppskatta fostrets vikt med hjälp av högupplösta MR-bilder. Dessa metoder skulle på sikt kunna leda till ökad förståelse för fostrets fysiologi och förbättrad diagnostik avseende komplicerade graviditeter.

Acknowledgements

I would like to thank everyone in the Lund Cardiac MR group and everyone at the Department of Clinical Physiology in Lund for giving me the opportunity to work with you for the last several years. It has been a joy working with you all and I hope we will continue working together for years to come. Special thanks to:

My supervisors **Erik Hedström** and **Katarina Steding-Ehrenborg** for excellent supervision and for important discussions about leadership.

Sebastian Johansson, for teaching me how to use the MR scanner, explaining MR physics, for always supporting your colleagues and for sharing your sense of humor. **Johannes Töger**, for taking your time to discuss MR physics and for providing feedback on my thesis summary. **Håkan Arheden** for important reflections and discussions about leadership. **Tom Gyllenhammar**, for supervising me as a semester five medical student, and for all support thereafter. **Per Arvidsson**, for countless interesting discussions and for providing feedback on my thesis summary. **David Nordlund, Robert Jablonowski and Jonathan Berg**, for great collaboration. **Anthony Lindholm**, for many interesting discussions and for your bravery at Dracula's castle in 2015. **Petter Frieberg**, for being a great colleague and for sharing your sense of humor. **Misha Bhat** and **Katrin Fricke**, for great collaboration. **Henrik Engblom** and **Ellen Ostenfeld**, for always being encouraging and for excellent clinical supervision. **Marjolein Piek**, **Johanna Koul** and **Charlotte Åkesson**, for great collaboration and for performing fetal CMR examinations. **Reza Farazdaghi**, for being a great colleague and for always making people laugh. **Anders Nelsson**, for excellent clinical supervision. **Jonas Liefke**, for great collaboration and important discussions. **Einar Heiberg**, for great collaboration and for providing feedback on my thesis summary. **Anthony Aletras**, for helping me understand basic MR physics and for great collaboration. **Barbro Kjellström**, for being a great colleague and for providing feedback on my thesis summary.

Everyone I have worked with in research and at the clinical department for all support and collaboration. **Henrik Mosén**, **Pia Sjöberg**, **Marcus Carlsson**, **Björn Östenson**, **Jonathan Edlund**, **Mikael Kanski**, **Mariam Al-mashat**, **Kristian Dimovski Anna Székely**, **Elsa Bergström**, **Jane Tufvesson**, **Karin Pola**, **Johan Lundeberg**, **Fredrik Hedeer**, **Ida**

Skarping, **Jonas Jögi**, **Martin Johansson**, **Julius Åkesson**, **Tania Lala**, **Petru Liuba**, **Ann-Helen Arvidsson**, **Håkan Månsson**, **Christel Carlander**, **Annmarie Svensson** and **Anna Sakaria**.

Finally, I would like to thank my beloved wife **Julia Ryd** for all support and for sharing life.

Part I

Research context

Chapter 1

Introduction

1.1 The fetal circulation

The fetal circulation is different from the postnatal circulation (Figure 1.1). A central difference is that the fetal lungs do not take part in gas exchange. Instead, gas exchange occurs in the placenta [1]. The placenta is an organ which is attached to the wall of the pregnant uterus and whose main function is to allow gas exchange and transfer of nutrients between the pregnant woman and the fetus. The umbilical cord contains the umbilical arteries and umbilical vein, which transfer fetal blood to and from the placenta respectively [2–4]. Maternal arteries carry oxygenated blood, whereas fetal umbilical arteries carry deoxygenated blood to the placenta. In the placenta oxygen is transferred from the maternal blood to the fetal blood by diffusion over a membrane separating the maternal and fetal placental blood [1]. Oxygenated fetal blood is returned to the fetus through the umbilical vein, which has the highest saturated blood in the fetus [1]. The umbilical vein is directly connected to the inferior vena cava through the ductus venosus (Figure 1.1) [1]. Thus, oxygenated blood flows through the umbilical vein into the ductus venosus to the inferior vena cava and continues to the right atrium. Through streaming within the inferior vena cava and through a ridge, the eustachian valve, in the right atrium, the highly oxygenated blood from the placenta is preferentially directed towards an opening in the atrial septum called the foramen ovale (Figure 1.1) [1, 5, 6]. This opening allows for oxygenated blood to be transferred directly from the right atrium to the left atrium and subsequently to the left ventricle and ascending aorta (Figure 1.1). This ensures that the blood with highest oxygen saturation reaches the coronary arteries and brain as these are supplied by the ascending aorta. As the fetal lungs are collapsed and filled with amniotic fluid, and does not contribute to gas exchange, blood flow to the fetal lungs is limited [3]. Instead, there is another fetal connection between the pulmonary trunk and descending aorta called the ductus arteriosus (Figure 1.1) [2–4]. Blood from the superior vena cava mixed with some of the blood from the inferior vena cava reaches the right ventricle, which pumps blood through the pulmonary trunk, where flow continues mainly through the ductus arteriosus

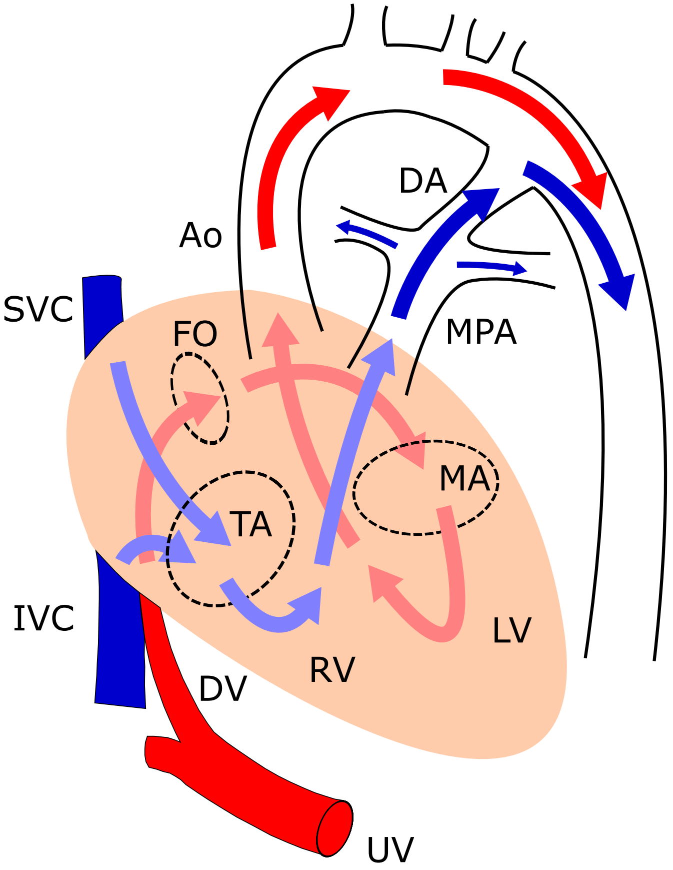

Figure 1.1: The fetal circulation. Oxygenated blood returns from the placenta to the fetus through the umbilical vein. The umbilical vein forms the ductus venosus, which passes through the liver and connects the umbilical vein directly to the inferior vena cava. Blood from the ductus venosus preferentially flows through the foramen ovale to the left side of the heart and subsequently to the fetal ascending aorta (red arrows). Less oxygenated blood (blue arrows) from the right ventricle flows to the main pulmonary artery and continues through the ductus arteriosus directly into the descending aorta and is distributed to the placenta and lower body. *Ao, aorta; DA, ductus arteriosus; DV, ductus venosus; FO, foramen ovale; IVC, inferior vena cava; LV, left ventricle; MA, mitral annulus; MPA, main pulmonary artery; RV, right ventricle; SVC, superior vena cava; TA, tricuspid annulus; UV, umbilical vein.*

to the fetal descending aorta. This flow of blood is distributed mainly to the lower body of the fetus and to the placenta [3], mixed with residual blood from the left ventricle through the transverse aorta. Transition from fetal to postnatal circulation occurs by closure of the ductus arteriosus and ductus venosus as well as the foramen ovale within the first few days after birth [7–11]. The connections in the fetal circulation allow for blood with the highest oxygen saturation and nutrient content to be delivered to the brain and heart. The fetal connections however also allow for one side of the heart to compensate for the other in severe cases of congenital heart defects.

1.2 Congenital heart defects

Congenital heart defects are a group of congenital malformations affecting the cardiovascular system. These cardiovascular malformations affect approximately 1% of infants [12] and vary in severity. The most common congenital heart defect is the ventricular septal defect [13]. In this condition, there is a hole in the ventricular septum. The vascular resistance of the downstream circulation determine flow across the ventricular septal defect [14]. In the postnatal circulation, the lower vascular resistance of the pulmonary circulation compared to the systemic circulation causes oxygenated blood to flow from the left ventricle directly into the right ventricle [14]. This oxygenated blood continues through the pulmonary circulation and returns to the left ventricle without being delivered to the intended organs. The volume of blood flowing from the left ventricle directly to the right ventricle, called shunt volume, therefore leads to unnecessary work performed by the left ventricle, and a fluid load to the lungs which causes increased work of breathing [15, 16]. Clinical manifestations depend on shunt size and range from no symptoms to heart failure [13].

In several severe congenital heart defects, the survival of the newborn is dependent on patency of the ductus arteriosus [17]. These defects are said to be duct dependent. An example of a duct dependent congenital heart defect is hypoplastic left heart syndrome. In hypoplastic left heart syndrome, the left ventricle is severely underdeveloped and unable to provide sufficient blood flow to the organs [18]. Blood that has been oxygenated in the lungs must therefore be able to pass from the left side of the heart to the right side of the heart [18]. This occurs through an interatrial communication [18], the foramen ovale. After entering the right side of the heart, the oxygenated blood must be able to pass from the right side of the heart to the systemic arteries. This occurs through the ductus arteriosus [18]. The closure of the ductus arteriosus during the transition from fetal to postnatal circulation leads to lack of blood supply to vital organs, circulatory shock, and death of the infant unless treatment is promptly initiated. This is done by starting prostaglandin infusion, which maintains patency of the ductus arteriosus, until the patient can undergo surgery [19].

Ultrasound screening of fetuses has enabled prenatal detection of congenital heart defects. A correct prenatal diagnosis has been shown to reduce mortality and morbidity, as well as improve parental counseling [20–25]. This is particularly the case in duct-dependent malformations. However, detection rates vary among different malformations and between centers [26]. While ultrasound examination is successful in the majority of cases, ultrasound may be unable to visualize fetal cardiovascular structures, particularly in late pregnancy or obese pregnant women. In addition, ultrasound has limitations in quantitative measurements of blood flow [27], an important indicator of cardiovascular pathophysiology. Therefore, there is a need for improved methods for prenatal assessment of congenital heart defects. In this thesis, newly developed magnetic resonance imaging (MRI) techniques were used to assess the fetal heart and circulation.

1.3 Magnetic resonance imaging

Main components of the magnetic resonance system

In a magnetic resonance (MR) scanner, a strong static magnetic field in the direction of the bore is created by current through a superconducting coil. The MR system has additional coils which are used for imaging. One such coil is the transmitting radio frequency (RF) coil [28]. A radiofrequency pulse can be transmitted through this coil, which creates a new magnetic field perpendicular to the main magnetic field and which rotates around the main magnetic field at a certain frequency [28]. Furthermore, the MR system has three gradient coils [29]. These coils can create magnetic field gradients in all directions in space, where field strength vary linearly with position along the direction of the magnetic field gradient. Finally, the MR system has receiver RF coils which receive the MR signal described in the following section [28].

The magnetic resonance signal

The most common source of MR signal is protons, which are ubiquitous in the tissues of the body. Protons behave like small magnets, each with its own magnetic field which can be viewed as a vector with magnitude and direction (Figure 1.2A). Protons in a strong main magnetic field show a slight overall tendency to point in the direction of the field, and are randomly oriented in the direction perpendicular to the field [30] (Figure 1.2A). Furthermore, protons rotate about their own axis, and are therefore commonly referred to as spins. Spins in a magnetic field show an additional rotating motion called precession about the magnetic field [30] (Figure 1.2A). The frequency ω of precession is given by the Larmor equation $\omega = \gamma \cdot B_0$ where γ is the gyromagnetic ratio and B_0 is the magnetic field strength of the main magnetic field [30]. The vector sum of the magnetic fields of spins in a small neighborhood forms the net magnetization vector M which points in the direction of the main magnetic field (Figure 1.2A). By convention, the direction of the main magnetic field represents the z-axis of a three-dimensional coordinate system. The net magnetization vector from protons in water molecules in tissues provide the basis for magnetic resonance imaging for clinical applications. However, in order to measure that tissue magnetization, additional procedures are needed.

By applying a radiofrequency pulse, an oscillating magnetic field perpendicular to the main magnetic field is created. If the frequency of the radiofrequency pulse closely matches the frequency of precession of the spins in the tissues, these spins will begin to rotate down towards the xy-plane (Figure 1.2B) [30]. This tips the net magnetization vector (Figure 1.2B) [30]. When the net magnetization vector rotates down towards the xy-plane, it simultaneously precesses about the main magnetic field (Figure 1.2B). Furthermore, the net magnetization vector now has a non-zero projection M_{xy} on the xy-plane (Figure 1B). This creates an oscillating magnetic field in the xy-plane, which induces current in the receiver coils of the MR system. This current is the MR signal (Figure 1.2C).

A magnetization vector can be defined by its magnitude, frequency of precession and angle of precession (Figure 1.3). The angle of precession, also referred to as phase, is defined as the counter-clockwise angle of the magnetization vector in relation to the x-axis. These properties of magnetization vectors are important in the process of generating an image from the MR signal.

$T2^*$ relaxation

The MR signal described above decays over time (Figure 1.2C). The most rapid decay is due to inhomogeneities of the main magnetic field and spin-spin interactions which cause dephasing of magnetization vectors on the xy-plane. This process is called $T2^*$ relaxation (Figure 1.4) [31].

$T2$ relaxation

Even with a perfectly homogenous main magnetic field, the MR signal would decay due to spin-spin interactions. When the contribution of main magnetic field inhomogeneities are ignored, the MR signal decays with time according to the equation $M_{xy} = M_0 \cdot e^{-t/T2}$, where M_{xy} is the transverse magnetization at time t, M_0 is the transverse magnetization at time 0, and $T2$ is a tissue-specific constant (Figure 1.4). This is called $T2$ relaxation [32].

$T1$ relaxation

When the MR signal is generated, the net magnetization vector is rotated down towards the xy-plane. When the radiofrequency pulse is turned off, the net magnetization vector therefore has a reduced longitudinal component $M_z(0)$ along the z-axis. As spins return to their orientation in the direction of the main magnetic field, the longitudinal component of the net magnetization vector regrows. The regrowth of M_z is described by the equation $M_z = M_{eq} - (M_{eq} - M_z(0)) \cdot e^{-t/T1}$, where M_z is the longitudinal magnetization at time t, M_{eq} is the longitudinal magnetization at equilibrium and $T1$ is a tissue-specific constant (Figure 1.4). This is called $T1$ relaxation [32].

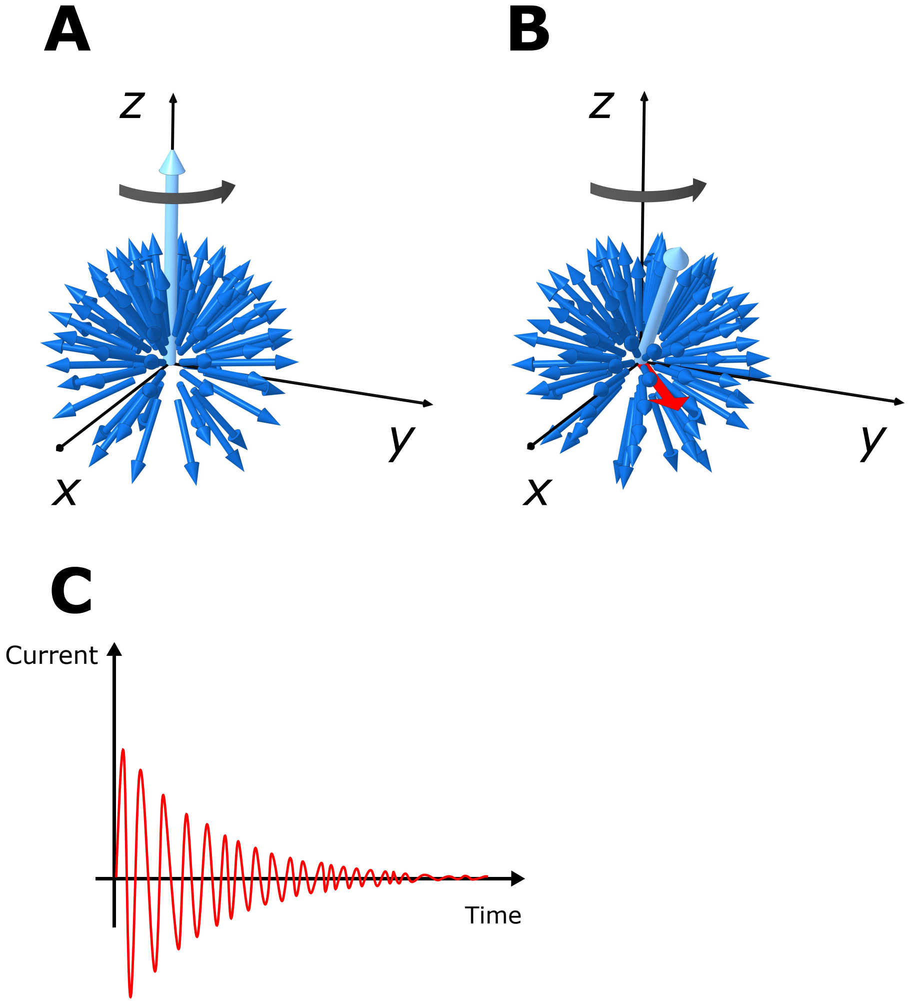

Figure 1.2: Generating the magnetic resonance signal. Spins from an object in a strong magnetic field are represented by the dark blue arrows, indicating the magnitude and direction of their magnetic fields. At equilibrium (**A**), spins are preferentially oriented in the direction of the main magnetic field (z-axis), as illustrated by the more dense distribution of arrows pointing in the z-direction versus in the opposite direction. The vector sum of all spins forms the net magnetization vector (bright blue larger arrow) pointing in the z-direction (**A**). Furthermore, spins rotate about the z-axis in a motion called precession, as indicated by the grey arrow. By applying a radiofrequency pulse at a frequency that closely matches the frequency of precession of the spins, the spins will begin to rotate down towards the xy-plane (**B**). This causes the net magnetization vector to rotate down towards the xy-plane (**B**). Furthermore, the net magnetization vector now has a non-zero projection M_{xy} on the xy-plane (red arrow) (**B**). This creates a rotating magnetic field in the xy-plane, which induces an oscillating current in the receiver coils of the MR system. This current is the MR signal (**C**).

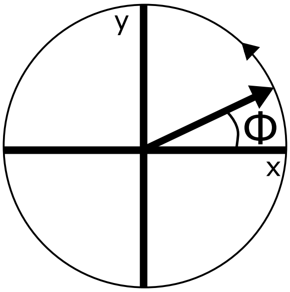

Figure 1.3: Characteristics of a magnetization vector. A magnetization vector is defined by its magnitude (length of the arrow), angle and frequency of precession. The phase Φ of the magnetization vector is defined as the counterclockwise angle with respect to the x-axis.

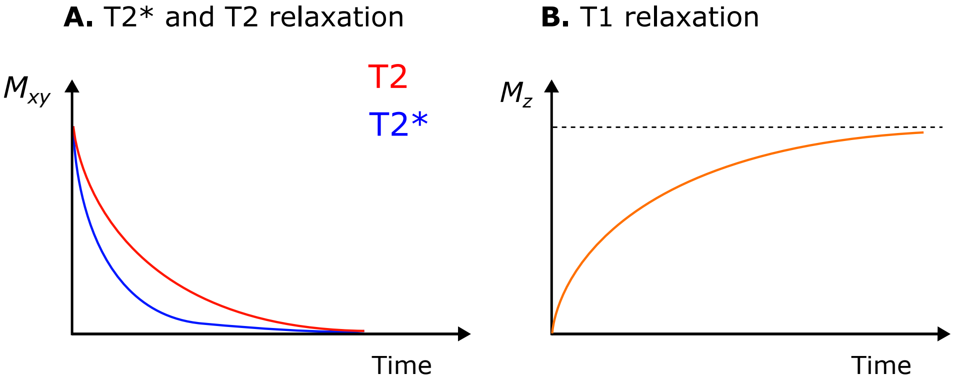

Figure 1.4: T1, T2 and T2* relaxation. After a radiofrequency pulse, the transverse magnetization M_{xy} decays over time ($T2^*$ decay) due to magnetic field inhomogeneities and spin-spin interactions (A). If the effects of field inhomogeneities are ignored, the signal decays due to spin-spin interactions, also referred to as $T2$ decay (**A**). If the net magnetization vector is rotated 90 degrees towards the xy-plane by the radiofrequency pulse, the longitudinal component of that vector is 0. As spins return to their orientation in the direction of the main magnetic field, the longitudinal component of the net magnetization vector regrows (**B**). The dashed line (**B**) indicates the magnitude of the net magnetization vector at equilibrium.

Image formation

The following sections describe the principles of forming an image from the MR signal. A magnetic resonance image can be thought of as a slice with a certain spatial resolution. Therefore, imaging requires defining the position, orientation and thickness of the slice from which the MR signal is generated, followed by localization of the signal components within the slice.

Slice selection

The first step in the spatial localization of the MR signal is to select the slice of interest (Figure 1.5A) [33]. This is done by applying a magnetic field gradient perpendicular to the slice of interest. For simplicity we will assume that the slice of interest is transversal and thus that the magnetic field gradient is applied in the z-direction. When a magnetic field gradient is applied in the z-direction, the magnetic field strength will vary linearly with position along the z-axis. This in turn will cause differences in the frequency of precession among spins which depend linearly on position along the z-axis, as described by the Larmor equation (Figure 1.5B). By applying a radiofrequency pulse with a frequency that matches a specific position along the z-axis, only spins near this z-position will be affected by the radiofrequency pulse (Figure 1.5C). Thus, the only spins that contribute to the transverse magnetization that generates the MR signal are those within the slice of interest (Figure 1.5C).

Spatial localization of the signal components within the slice

We have defined the slice that we would like to image using the slice selection process described above. To form a two-dimensional image, the components of the resulting MR signal have to be localized in the xy-plane. This is performed using two additional processes called phase encoding and frequency encoding [33, 34]. Phase encoding is performed by applying a magnetic field gradient in the phase-encoding direction (which for simplicity is assumed to be the y-axis). This causes the magnetic field strength, and thus the frequency of precession, to vary depending on position along the y-axis. With time, spins along the y-axis therefore acquire different amounts of phase depending on their position. The phase-encoding gradient is applied after the slice-selective radiofrequency pulse, but before frequency encoding.

Frequency encoding is a similar process which occurs simultaneously with sampling of the MR signal. A magnetic field gradient is applied along the frequency-encoding direction, perpendicular to the phase-encoding direction (which for simplicity is assumed to be the x-axis). This causes the magnetic field strength, and thus the frequency of precession, to vary depending on position along the x-axis. At a given point in time, spins along the x-axis will have acquired different amounts of phase due to the frequency-encoding gradient. As the MR signal is sampled multiple times during the application of the frequency-encoding

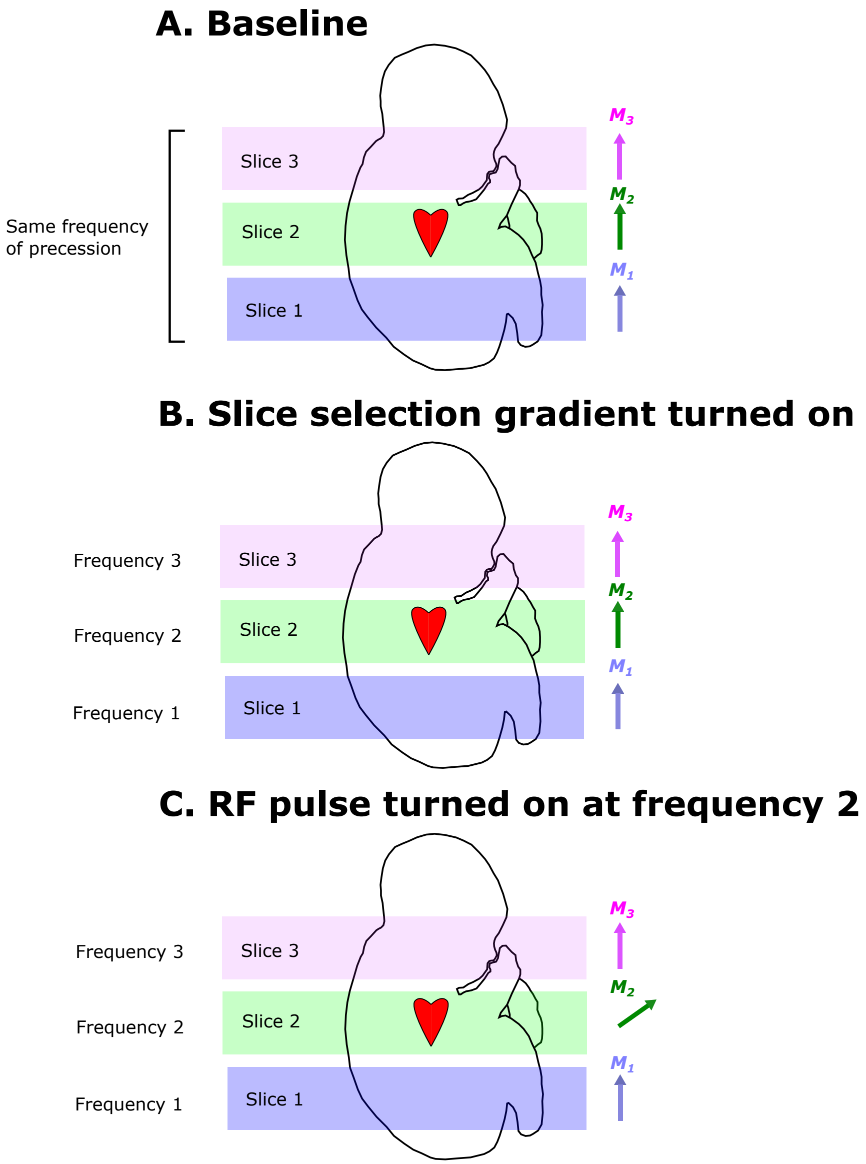

Figure 1.5: Slice slection. Figure **A** shows a fetus in the MR scanner, divided into three slices where slice 2 contains the heart. The net magnetization vectors of these slices are shown as M_1, M_2 and M_3 to the right. At baseline, the main magnetic field is homogenous and the frequency of precession of spins within all three slices are equal. When a magnetic field gradient is turned on in the z-direction, the magnetic field strength and thereby the frequency of precession is different for each slice (**B**). By applying a radiofrequency pulse at frequency 2, only spins with the same frequency will be affected (**C**). This will rotate M_2 down towards the xy-plane while leaving M_1 and M_3 unaffected (**C**). As a result, the generated MR signal will be derived only from slice 2 which contains the fetal heart.

gradient, each signal sample corresponds to a unique pattern of phase variation along the frequency-encoding direction. Furthermore, the preceding phase-encoding step defines a specific pattern of phase variation along the y-direction.

It can be shown that each signal sample corresponds to a specific *spatial frequency* of the MR image, defined by the specific phase variation patterns along the phase- and frequency-encoding directions respectively (Figure 1.6). While multiple spatial frequencies along the x-direction can be acquired during a single readout of the MR signal, each spatial frequency along the y-direction requires a separate generation of the MR signal with a different phase-encoding gradient strength. The acquired MR signal samples are stored in a matrix called k-space, which contains the spatial frequencies of the MR image. By applying an inverse Fourier transform to k-space data, the magnitude and phase of the net magnetization vector corresponding to each pixel in the MR image is obtained.

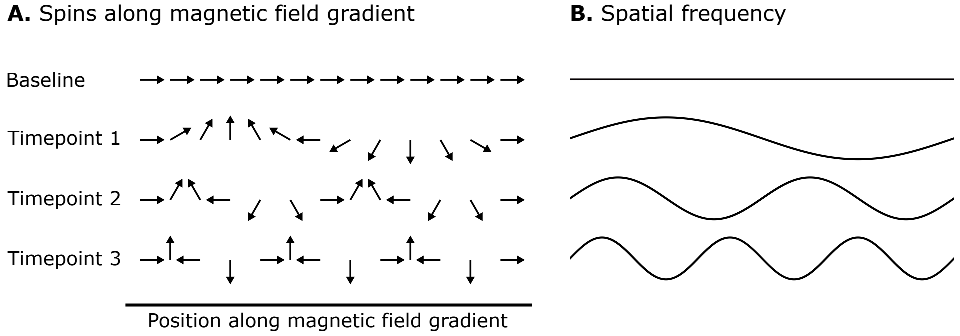

Figure 1.6: Spatial frequencies. At baseline, all spins have the same phase (**A**). When a linear magnetic field gradient is applied, the frequency of precession will vary linearly with position along the direction of the gradient. With time, spins therefore acquire different amounts of phase depending on position (**A**). Timepoints 1 – 3 in panel **A** represent successively increasing phase accumulation as the gradient magnetic field is applied. At each timepoint, the phase variation pattern along the direction of the gradient defines a spatial frequency, as illustrated in panel **B**. For phase-encoding, timepoints 1 – 3 correspond to generating the MR signal three separate times, each with a different strength of the phase-encoding gradient. For frequency-encoding, timepoints 1 – 3 correspond to three consecutive samples of the MR signal during the application of the frequency-encoding gradient.

Cardiovascular magnetic resonance imaging

In the cardiovascular system, motion occurs with every cardiac cycle. In order to generate high quality cardiovascular magnetic resonance (CMR) images of the heart and blood vessels, this motion has to be accounted for. In general, this is accomplished by dividing the cardiac cycle into short time frames and acquiring a separate image during each time frame. If such images are acquired throughout the cardiac cycle, the result is a cine image showing cardiac motion. The ability to depict cardiac motion depends on the temporal resolution, i.e., the time period that constitutes one cardiac phase. Typically, a temporal resolution of about 30 milliseconds is used. In order to acquire cine images, image information is acquired from several cardiac cycles.

Cardiac gating refers to the process of synchronizing acquired image data with the cardiac cycle. This is commonly performed by acquiring magnetic resonance image data while recording the cardiac rhythm using electrocardiography [35].

Flow measurements

Magnetic resonance imaging can be used to measure blood flow [36–38]. In this section, the basic principles of flow measurements by MRI will be described, followed by a discussion of the strengths and limitations of this technique.

In order to measure flow by MRI, a technique called phase-contrast imaging is used. The principle of this technique is to alter the phase of spins in such a way that phase becomes proportional to velocity. This is performed by applying a bipolar magnetic field gradient along the direction in which velocity is to be measured. Figure 1.7 illustrates how a bipolar magnetic field gradient affects the phase of stationary and moving spins respectively. As a first negative magnetic field gradient is turned on, stationary spins experience a weaker magnetic field strength and will therefore precess at a lower rate. This will cause the stationary spins to lose phase. As stationary spins experience a constant magnetic field strength throughout the application of the magnetic field gradient, the change in phase for stationary spins during the magnetic field gradient application is proportional to gradient amplitude and time. As the negative magnetic field gradient is turned off, and a positive magnetic field gradient of equal amplitude and duration is turned on, stationary spins will precess faster and regain the amount of phase that was previously lost. Thus, the application of a bipolar magnetic field gradient leads to no net change in phase for stationary spins.

As spins moving along a magnetic field gradient experience a continuously increasing (or decreasing) magnetic field strength over time, the relationship between change of phase, gradient amplitude and time is different compared with stationary spins. It can be shown that the change of phase for moving spins with a constant velocity is proportional to velocity, gradient amplitude and time squared. Therefore, moving spins will lose some amount of phase during the application of a first negative magnetic field gradient. However, with the following application of a positive magnetic field gradient of equal amplitude and duration, moving spins will experience a stronger magnetic field than during the negative gradient application, and will therefore gain more phase than was previously lost. Therefore, after the application of a bipolar magnetic field gradient, moving spins will have gained phase which can be measured. As phase is proportional to velocity, gradient amplitude and time squared, velocity can be calculated based on phase if gradient amplitude and time are known.

In order to quantify blood flow, the phase-contrast technique is used to measure flow velocity in each pixel of a cross section of the vessel of interest. By multiplying mean velocity with cross-sectional area, flow is obtained.

Strengths and limitations of flow quantification by magnetic resonance imaging

Magnetic resonance imaging can be used to quantify flow volumes with high accuracy [39–43]. Further strengths of this MRI-based technique include the possibility to image blood vessels in any direction. Clinical applications of flow volume measurements by MRI include quantification of valvular regurgitation and shunts [44, 45], which can be used to guide treatment. Furthermore, unlike ultrasound, MRI is not limited by acoustic windows. Therefore, quantification of blood flow by MRI is an important tool for studying cardiovascular physiology. However, there are important limitations to consider.

Spatial and temporal resolution

Spatial and temporal resolution are important considerations, particularly in fetal MRI as the fetal aorta typically has a cross sectional area of less than 1 cm^2 and the fetal heart rate is about 140 beats per minute. With insufficient spatial resolution, voxels at the interface between flowing blood and stationary tissue will receive MR signal from both. This is called partial volume effects. As the magnetization vector of a voxel equals the vector sum of all spins within that voxel, the phase of the magnetization vector from a voxel including stationary tissue and flowing blood will be affected by the stationary tissue [46, 47]. This leads to underestimation of peak velocity and may lead to incorrect estimation of average phase and hence total flow [38, 46, 47]. Similarly, when a voxel contains moving spins with different velocities, intravoxel phase dispersion can cause incorrect measurements of velocity. The minimum spatial resolution for accurate flow quantification has been shown to be 16 pixels over the vessel area [46, 47]. Sufficient temporal resolution is required to accurately capture the flow curve throughout the cardiac cycle. With insufficient temporal resolution, pulsatile flow is underestimated [38].

Turbulent flow

In turbulent flow, such as flow after a stenosis, flow velocities differ significantly even within a voxel. Turbulent flow leads to incorrect flow measurements [48], due to intravoxel phase dispersion.

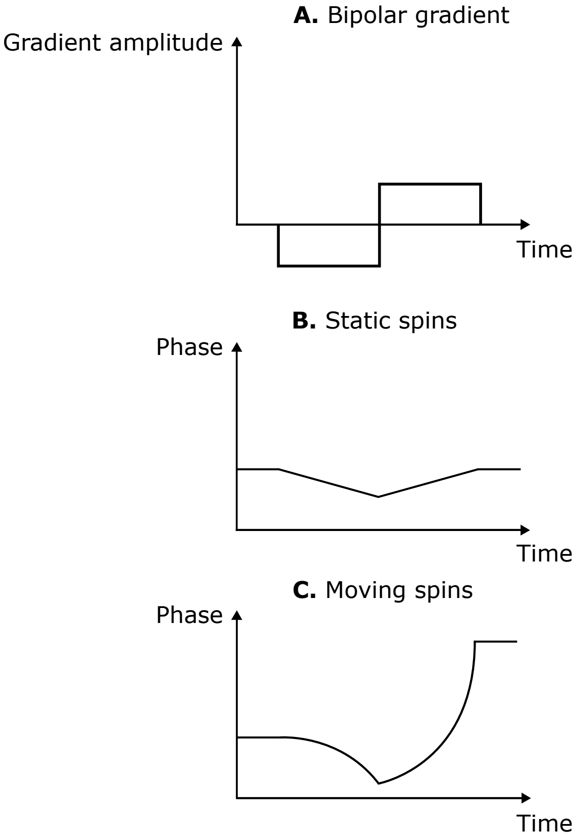

Figure 1.7: Phase-contrast imaging. A bipolar magnetic field gradient is applied. Diagram **A** illustrates this bipolar magnetic field gradient. Diagrams **B** and **C** show the effect of the bipolar gradient on the phase of stationary and moving spins respectively. For stationary spins, there is no net change in phase after the application of the bipolar gradient. For moving spins however, an amount of net phase is acquired that is proportional to the velocity of the spins. This acquired phase can be measured and used to derive the velocity of the moving spins.

Misalignment of the image plane

Flow quantification is most accurate when the imaging slice is perpendicular to the vessel [42, 47]. As velocity is encoded perpendicular to the slice, an oblique slice over a blood vessel will encode the projection of the blood velocity on the direction perpendicular to the slice rather than the true blood velocity [47]. This leads to underestimation of velocity. However, the vessel area over which flow is acquired increases. For thin slices, these effects cancel and cause no error in total flow, however as slice thickness increases, partial volume effects cause overestimation of flow [47]. This presents a particular challenge in fetal MRI as fetal movement may occur during imaging and resolution is relatively low compared to vessel size.

Phase offset errors

Rapid gradient coil activations can induce currents in the gradient coils themselves. This interferes with the magnetic field gradients, which in the case of phase-contrast imaging may cause phase offset errors [49]. Unless properly accounted for, phase offset errors may cause large errors in measured flow [49]. Correction methods include subtraction of the velocity error as estimated based on stationary tissue information in the same patient or in a stationary phantom scan performed in conjunction with the examination of the patient [50, 51].

Velocity encoding

If a small amount of phase is acquired at a given velocity, the measurement of that phase (and hence velocity) is prone to error due to noise [38]. On the other hand, if for a given velocity more than 180° phase is acquired, that velocity will be incorrectly interpreted as velocity in the opposite direction, commonly referred to as *aliasing* [38]. Therefore, a phase-contrast image acquisition should be designed to be optimally accurate to the flow velocity that can be expected in the vessel of interest. As phase shift is proportional to both velocity and gradient amplitude, the higher the amplitude of the bipolar gradient, the more phase will be acquired for a given velocity. Therefore, a strong gradient provides higher sensitivity to low velocities, whereas a weak gradient provides higher sensitivity to high velocities [38]. The velocity encoding parameter (VENC) is defined as the highest velocity that can be measured without aliasing and is adjusted depending on the expected flow velocity in the vessel of interest.

1.4 Machine learning

One of the first definitions of machine learning, attributed to Arthur Samuel in 1959, is that machine learning is the "Field of study that gives computers the ability to learn without being explicitly programmed". Subsequently in 1998, Tom Mitchell stated that "a computer program is said to learn from experience E with respect to some task T and some performance measure P, if its performance on T, as measured by P, improves with experience E". Machine learning is widely used and have become a very hot topic in the last five years. A few examples of situations where machine learning have proven to be successful is in image classification, image analysis, classification of emails as spam or non-spam, and for voice recognition.

General principles and considerations

Machine learning can be used to estimate a continuous-valued output based on an input, or to make classifications of an input into one of several classes. Two relatively simple machine learning algorithms for prediction of a continuous-valued output and classification respectively are linear regression and logistic regression. These models can be used as examples to demonstrate some of the main principles of machine learning.

Linear regression

In simple linear regression, a training set of data points (x_i, y_i) is used to estimate a straight line fit to the data (Figure 1.8). The goal of linear regression is to use the straight line equation to estimate the y-value corresponding to an x-value not included in the training set (Figure 1.8). A model of the form $y = ax + b$ is optimized to best fit the training data. In order to do this, for a given choice of the parameters a and b, we need a performance measure of the model. This performance measure, often called cost function, is a function that measures the overall error of the given model on the training data. The higher the error on the training data, the higher the value of the cost function. To optimize the model, the parameters a and b that minimize the cost function are chosen. In linear regression, the cost function F is defined as the mean of the squared errors of the model over the training set. If k is the number of training examples, then $F(a, b) = \frac{1}{k} \sum_{i=1}^{k} ((ax_i + b) - y_i)^2$, and the parameters a and b that minimize the cost function $F(a, b)$ will give the best straight line fit to the data. While this example assumes a linear model with one variable, the same principles can be used to estimate a more complex model with more linear terms and higher order polynomial terms.

Logistic regression

Logistic regression is another example of machine learning used for classification rather than prediction of a continuous-valued output. The simplest example is binary classification, i.e.,

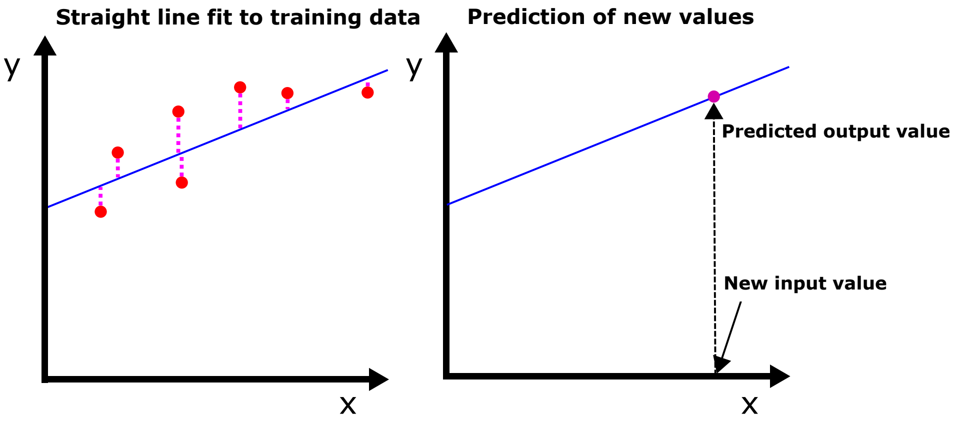

Figure 1.8: Linear regression. The left graph shows training data points (red circles) in the xy-plane. The best straight line fit to this training data can be achieved by minimizing the mean squared error between the straight line and the training data points, as shown by the pink dashed lines. The straight line equation can be used to estimate the y-value corresponding to a new x-value (**right**). This is called linear regression, which can be seen as a simple learning algorithm.

classification of an input variable into one of two possible classes. The training data consist of points (x_i, y_i), where each y_i is equal to either 0 or 1. The logistic function $g(z) = \frac{1}{1+e^{-z}}$ is used for classification, where the value of the logistic function is interpreted as the probability that a given input belongs to class 1. In order to optimize the model given the available training data, the variable z in the logistic function above is chosen as some parametrization of the input variable x, with parameters that can be optimized to give high probabilities for training examples belonging to class 1 and low probabilities for training examples belonging to class 0. A simple example of the variable $z = z(x)$ could be $z(x) = ax + b$. To optimize the logistic regression model, a cost function must be defined which penalizes incorrect classifications. If $h(x)$ denotes the output of the logistic function for a given parametrization $z = z(x)$, the cost of the classification algorithm can be defined as $Cost(h(x_i), y_i) = -log(h(x_i))$ if $y_i = 1$ and $Cost(h(x_i), y_i) = -log(1 - h(x_i))$ if $y_i = 0$. The cost function of the logistic regression model is given by the average cost over all training examples.

In order to perform more complex tasks such as image classification, logistic regression is insufficient. Instead, more complex models such as artificial neural networks are needed.

Artificial neural networks

An artificial neural network is a method of machine learning inspired by the brain, which can be viewed as an advanced learning machine. In the brain, each neuron receives information from other neurons. This information is in turn propagated forward.

An illustration of an artificial feed-forward neural network is provided in Figure 1.9. Each circle in the figure denotes an artificial neuron. Each column of artificial neurons is called a layer of the artificial neural network. The network contains an input layer, in which input data is provided to the network. After the input layer, several so-called hidden layers follow, each of which processes information from the previous layer. The final layer of the neural network is called the output layer. In an artificial neural network, each neuron in one layer contributes with information to neurons in the next layer.

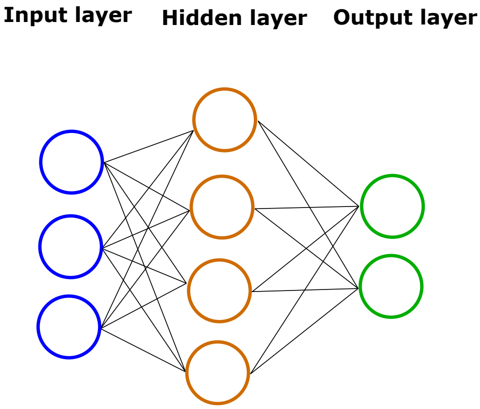

Figure 1.9: Schematic artificial neural network. An artificial neural network consists of artificial neurons, illustrated by circles. A column of artificial neurons is called a layer of the network. An artificial neural network has an input layer, one or more hidden layers, and an output layer. Each neuron in one layer forwards information to neurons in the next layer, illustrated by the black lines.

In order to demonstrate the calculations performed by the artificial neural network, consider Figure 1.10 which shows how information is propagated from one layer to the next. Each neuron in the first layer carries information to neurons in the next. Let $a_0 \dots a_k$ denote the outputs of the neurons of the first layer (Figure 1.10). Each neuron in the first layer is connected to neurons in the second layer by parameters which determine the contribution of the neuron in the first layer to the neurons in the second layer. Let $\theta_0 \dots \theta_k$ denote the parameters connecting the first layer to a specific neuron in the second layer (Figure 1.10). The output of the neuron in the second layer is calculated as $h(\theta_0 a_0 + \dots + \theta_k a_k)$ where h is some function defined as the activation function of the neuron.

Commonly used activation functions include a rectified linear unit function or a sigmoid function (Figure 1.10). Similar calculations are performed for each neuron in the artificial neural network until the output layer is reached. The error of the network output with regard to the desired output is measured by a cost function. The exact definition of the activation function and cost function respectively depends on the specific context in which the network is applied. By minimizing the cost function, the parameters of the neural network that best fit the training data are determined.

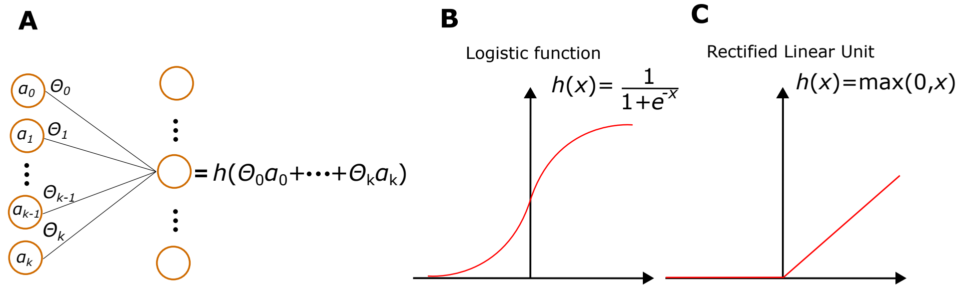

Figure 1.10: Computations performed by the artificial neural network. Each neuron in the first layer is linked to neurons in the second layer by parameters which determine the contribution of the neuron in the first layer to the neurons in the second layer (**A**). For a specific neuron in the second layer, the output of that neuron is calculated as a function of the weighted sum of parameters and neuron outputs from the previous layer (**A**). This function is called the activation function of the neuron. Two examples of such activation functions are a logistic function (**B**) and a rectified linear unit function (**C**).

Optimizing the cost function

The cost function of a learning algorithm is a function that measures the error of the model output versus the desired output. For image classification algorithms, the cross-entropy function is commonly used. This function returns high values i.e., high cost when the model outputs a low probability for the correct class label of the input image.

The performance of the learning algorithm is optimized by determining the model parameters that minimize the cost function given the available training data. As the minimum value of the cost function of a learning algorithm can be difficult to calculate explicitly, numerical optimization methods are often used. One such method is the gradient descent algorithm. It can be shown for a differentiable function f that at a given point $(\theta, f(\theta))$, the direction of steepest descent is the direction opposite to the gradient of f denoted ∇f. By choosing a random initial value of the input vector θ and iteratively changing θ to

$\theta - \alpha \cdot \nabla f(\theta)$ where α is some small positive number, θ can converge to a local minimum value of $f(\theta)$. Ideally, the cost function $f(\theta)$ should have only one local minimum which also is the global minimum. The number α is defined as the learning rate of the learning algorithm. It is not always easy to choose the number α appropriately. With a very small α, many computational steps are required to optimize the cost function, which can lead to a time-consuming training process for the learning algorithm. On the other hand, a too large α may cause the gradient descent algorithm to fail to converge to the local minimum of the cost function.

Model selection and evaluation

As we have already seen, learning algorithms are trained using training data to produce a desired output. While a trained model may perform well on the training data, this does not guarantee that it will perform well on new, previously unseen data. The generalizability of a learning algorithm is the ability to produce a desired output given a previously unseen input.

In order to evaluate how well a model generalizes, it must be tested on new data. Furthermore, it may be of interest to test different model structures rather than assuming that one particular structure is optimal. This is performed by adjusting the *hyperparameters* of the model. Examples of hyperparameters for an artificial neural network include the number of layers and neurons, the neuron connectivity pattern and the learning rate. To evaluate different model structures, each model structure is trained and tested on a validation data set. The model with the best performance on the validation data set is chosen. However, as the final model has been deliberately chosen based on its performance on the validation data, it is still not known how well it generalizes to new examples. Therefore, the final model should subsequently be evaluated on a test set consisting of new data.

Bias and variance

For a given machine learning problem, models of different complexity can be used. A too simple model may be unable to fit training data well. On the other hand, a too complex model may fit training data well, yet perform poorly on test data. These concepts can be illustrated using polynomial regression to fit a set of data points in the xy-plane (Figure 1.11). If a constant polynomial model is used to fit the data, this model will likely perform poorly on both training data and test data, and the model is said to be underfitted and to have high bias (Figure 1.11). On the other hand, if a high degree polynomial model is used, this model may fit the training data very well, but still perform poorly on test data, and the model is said to be overfitted and to have high variance (Figure 1.11). The optimal model has a complexity somewhere in between those extremes (Figure 1.11). If a learning algorithm turns out not to perform well, it may potentially be improved by increasing the training data set or by changing some aspect of the model itself. In order to determine which of these alternatives is likely more effective, it is useful to determine if the model has high bias or high variance. For a model with high bias, which underfits training data, adding more training data is unlikely to improve the model, and is likely a waste of time. Instead, changing the model itself so that it is able to fit the available training data may be useful. For a model with high variance on the other hand, which overfits the training data, adding more training data and/or modifying the model may be useful.

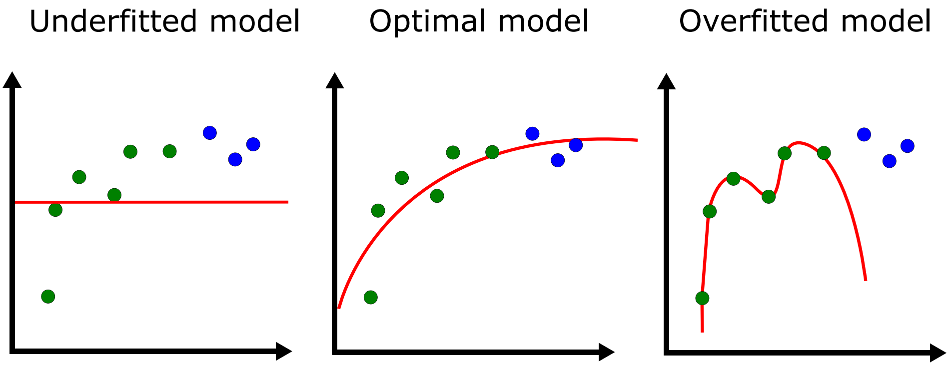

Figure 1.11: Bias and variance. Consider a set of training data points (green circles) and test data points (blue circles). Different polynomial models can be fitted to this data. If a too simple model is used, such as a constant polynomial (**left**), the model is unable to fit the training data well and performs poorly on both training and test data. This model is said to be underfitted and to have high bias. If on the other hand a too complex model is used, such as a high degree polynomial, this model fits training data well but still performs poorly on test data (**right**). This model is said to be overfitted and to have high variance. The optimal model has a complexity somewhere in between (**middle**).

Convolutional neural networks

A convolutional neural network (CNN) is an artificial neural network including layers which perform *convolution operations* on input data. Convolutional neural networks have proven to be highly successful in image analysis, as they can be used to deconstruct a complex image into simpler elements called feature maps, each containing specific features of the original image. A CNN can be trained to recognize a specific class of images by their feature maps using training data consisting of labeled images. When the trained CNN receives a new unseen input image, it deconstructs this image into feature maps and assesses the likelihood that those feature maps represent an image of the image class the CNN was trained to identify.

In order to understand how an input image is fed forward through a CNN, consider Figure 1.12 which illustrates the convolution operation for a 6x8 pixel input image. An image filter is a smaller image representing a specific feature (Figure 1.12). In Figure 1.12, the image filter is a 3x3 image containing a diagonal line of 3 pixels as a feature. This image filter is moved across the input image at every possible position. Each filter position over the input image is mapped to a third image called a feature map. If, at a given position, the feature of the filter matches the pattern of the input image, the corresponding pixel of the feature map receives a high value, illustrated by the bright green pixel in the feature map of Figure 1.12. If, on the other hand, the feature of the filter does not match the pattern of the input image, the corresponding pixel of the feature map receives a low value, illustrated by the black pixel in Figure 1.12. The feature map will thus be a feature representation of the input image, indicating where the pattern of the filter occurs in the input image. In a CNN, a convolutional layer may consist of several different filters, each deconstructing the input image into a feature representation of a specific feature. Typically, the filters in a CNN are part of the learning process, i.e., the network figures out what filters work best based on the training data. In order to simplify calculations, CNNs use layers which perform *pooling operations* on feature maps. Figure 1.13 illustrates an example of a pooling operation on a feature map. The left image shows a 4x4 feature map, where each pixel has a value corresponding to how well the input image pattern matched the filter pattern at a given filter position. The pooling operation maps this 4x4 feature map image into a 2x2 image according to Figure 1.13, where each pixel in the resulting 2x2 image is the maximum value of its corresponding part of the feature map. The pooling operation thus creates an image with slightly lower precision for the given feature, but which facilitates computations in the CNN. The filters of a CNN are learnable parameters, whereas the pooling operations must be defined beforehand.

Figure 1.14 shows an illustration of a convolutional neural network for image classification, which has been trained to classify input images as fetuses, cats, hats or boats. In the first step, a magnetic resonance image of a fetus is used as input. This image is passed through a convolutional layer with four different filters, creating four feature maps of the input image. In the next step, a pooling operation is performed on each feature map, resulting in four lower-dimensional images. The following layer is another convolutional layer with two filters, resulting in a total of 8 feature maps of the 4 input images from the previous layer. Subsequently, another pooling layer further reduces the image dimensions. The final layer is the output layer, which is commonly called the fully connected layer. Each artificial neuron of this layer receives input from each image in the previous layer. In the example in Figure 1.14, each neuron of the fully connected layer outputs a measure of how likely it is that the input image belongs to a certain class.

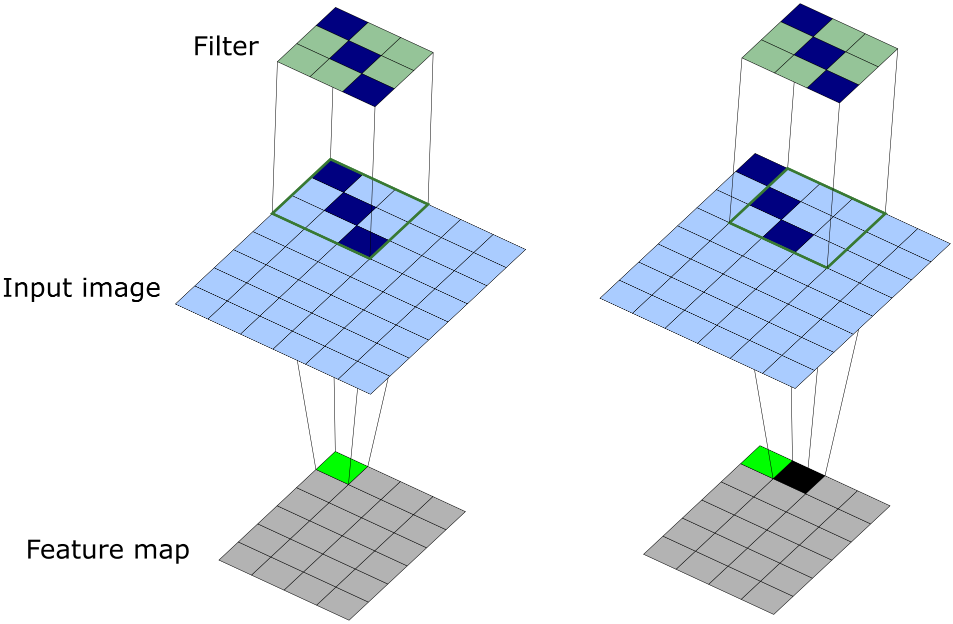

Figure 1.12: Convolution operation for a two-dimensional image. An image filter (top) is moved across the input image, and maps each position into a third image called a feature map. If the pattern of the input image matches the filter at a given position (**left**), the pixel of the feature map corresponding to this filter position receives a high value (bright green pixel in the bottom image). If on the other hand the pattern of the input image does not match the pattern of the filter at a given position (**right**), the pixel of the feature map corresponding to that position receives a low value (black pixel in the bottom image).

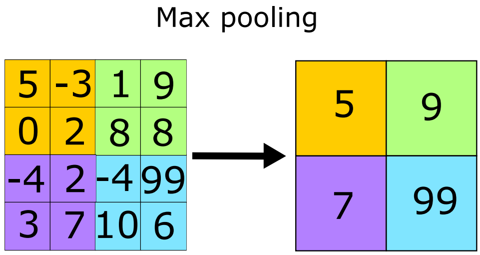

5	-3	1	9
0	2	8	8
-4	2	-4	99
3	7	10	6

5	9
7	99

Figure 1.13: Pooling operation. A 4x4 feature map (**left**) is divided into a 2x2 grid as shown by the four colours. A pooling operation reduces the dimension of the 4x4 feature map image to a 2x2 image, in this case replacing the four pixels in each quadrant with their maximum value (**right**). This operation facilitates computations in a convolutional neural network.

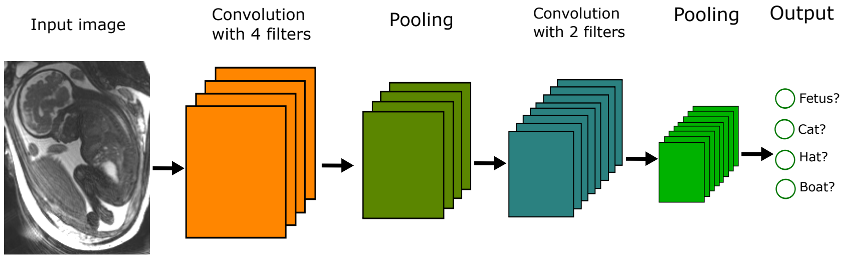

Figure 1.14: Convolutional neural network. An image of a fetus is used as input. The first layer is a convolutional layer with four filters, which creates four feature maps of the input image. The next layer is a pooling layer which reduces the dimensions of the feature maps. The next layer is a convolutional layer with two filters, creating a total of eight new feature maps. This is followed by another pooling layer, further reducing image dimensions. Finally, an output layer receives input from all images in the previous layer and uses this input to classify the original input image, in this case as either a fetus, a cat, a hat or a boat.

1.5 Study motivations

Study I - Quantification of fetal blood flow

Quantification of blood flow provide important insights into cardiovascular physiology. Blood flow measurements using MRI are considered accurate and have potential for improving blood flow assessment in fetuses. However, the lack of a fetal cardiac gating signal has hampered fetal blood flow assessment by MRI. While post-processing methods such as metric optimized gating [52] have partly overcome this issue, such methods require time-consuming offline image reconstruction and are potentially less accurate than direct cardiac gating. A recently developed MR-compatible Doppler ultrasound device has provided a solution for fetal cardiac gating [53, 54]. Therefore, evaluation of fetal flow quantification using this new gating technique is warranted.

Study II - Fetal volume quantification

While fetal blood flow measurements can provide information of cardiovascular pathophysiology, absolute flow values are expected to depend on fetal weight. Therefore, weight-indexed fetal flow values may more accurately depict underlying pathology compared to absolute values. While ultrasound-based fetal weight estimation is commonly used, this has been shown to be less accurate than MRI-based estimation [55]. Segmentation of the fetus in high-resolution MR images can provide accurate quantification of fetal volume which can be used to estimate fetal weight. However, manual segmentation requires 1 – 2 hours per case, and there is a need for automatic methods. Specifically, artificial neural networks for image segmentation could provide a solution.

Study III - Assessment of congenital heart defects

Recently developed CMR techniques allow for cardiovascular cine imaging in fetuses, providing information of the function and anatomy of the fetal heart. However, the role of fetal CMR for prenatal diagnosis of congenital heart defects is yet to be established. Ultrasound is and will likely continue to be the preferred imaging modality for initial assessment. However, as MRI is not limited by acoustic windows, the added value of fetal CMR in cases where fetal ultrasound is unable to answer all diagnostic questions warrants further study.

Study IV - Super-resolution image reconstruction for fetal CMR

While fetal CMR shows potential to improve prenatal assessment of congenital heart defects, an important limitation is the relatively long image acquisition times. This increases the risk of fetal movement during image acquisition, which results in motion artifacts and poor image quality. Therefore, shorter image acquisition times could increase the chance of successful fetal CMR examination. One way to decrease acquisition time is to decrease image resolution. However, a higher resolution must then be reconstructed to achieve high-quality images. This could be performed using so-called super-resolution image reconstruction.

Chapter 2

Aims

The overall aim of this thesis was to apply and develop fetal cardiovascular magnetic resonance imaging for assessment of fetal cardiovascular physiology.

The specific aims of studies I – IV were:

I To evaluate Doppler ultrasound gating for phase-contrast magnetic resonance flow measurements in fetal blood vessels, with the main hypothesis that quantification of fetal blood flow using Doppler ultrasound gating agree with metric optimized gating.

II To 1) apply artificial neural networks for automatic quantification of fetal volume in high-resolution magnetic resonance images; 2) Compare fetal weight measured by fetal segmentation in magnetic resonance images to fetal weight estimated by formulas developed for fetal ultrasound; and 3) index fetal blood flow values in the umbilical vein and descending aorta to fetal weight.

III To investigate the clinical utility of cardiovascular magnetic resonance imaging in fetuses with remaining diagnostic uncertainty after ultrasound examination.

IV To apply super-resolution image reconstruction methods to increase resolution in fetal CMR images acquired with a low resolution and reduced acquisition time.

Chapter 3

Materials and methods

3.1 Study populations

Study I

Twenty-two pregnant women in gestational week 36 (range 26 – 40) were included at Skåne University Hospital (Lund, Sweden). The study population consisted of both fetuses with and without known or suspected congenital heart defects. This study had a subject overlap of n=5 with study III and n=7 with study IV.

Study II

Forty-two pregnant women in gestational week 36 (range 29 – 39) were included at Skåne University Hospital (Lund, Sweden). The study population consisted of both fetuses with and without known or suspected congenital heart defects. This study had a subject overlap of n=4 with study III and n=6 with study IV.

Study III

Thirty-one pregnant women in gestational week 36 (range 31 – 39) were included at Skåne University Hospital (Lund, Sweden). All study participants had undergone fetal ultrasound screening, where a suspicion of congenital heart defect was raised. Subsequently all participants underwent at least one repeat fetal ultrasound examination performed by a pediatric cardiologist specialized in fetal cardiology. Patients with remaining diagnostic uncertainty after the second fetal ultrasound examination were referred for fetal cardiovascular magnetic resonance (CMR) examination and included in the study. This study had a subject overlap of n=5 with study I, n=4 with study II and n=9 with study IV.

Study IV

Twenty-eight pregnant women in gestational week 36 (26 – 40) were included at Skåne University Hospital (Lund, Sweden). The study population consisted of both fetuses with and without known or suspected congenital heart defects. This study had a subject overlap of n=7 with study I, n=6 with study II and n=9 with study III.

3.2 Fetal cardiovascular magnetic resonance imaging

All study participants underwent fetal CMR imaging using a 1.5T magnetic resonance (MR) scanner (Siemens Aera, Erlangen, Germany). To avoid compression of the inferior vena cava, the MR examination was performed with the pregnant woman in the left lateral decubitus position. A recently developed Doppler ultrasound (DUS) device (smart-sync, northh medical GmbH, Hamburg, Germany) was used for cardiac gating [53, 56]. Cardiac gating is necessary to acquire high-quality images of the heart and blood vessels, as described in the introduction section. The most commonly used method to acquire a cardiac gating signal is by electrocardiography. However, it is not yet possible to acquire a fetal electrocardiography signal of sufficient quality for cardiac gating during CMR examination. Instead of recording the electrical activity of the fetal heart, the DUS device records a velocity waveform from the fetal heart which can be used to identify each fetal heartbeat. This has enabled state-of-the-art CMR techniques for cardiovascular cine imaging and phase-contrast flow measurements in fetuses.

3.3 Study I - Quantification of fetal blood flow

Image acquisition

Phase-contrast images for flow quantification were acquired in the fetal descending aorta (DAo) and umbilical vein (UV) (Figure 3.1) using a 2D segmented gradient recalled echo sequence. Typical parameters were 1.41x1.41x5 mm spatial resolution, 30.18 ms temporal resolution, flip angle 20° and TE/TR 2.76/5.03 ms. Quantitative flow images were acquired using both the DUS gating method and the previous reference method metric optimized gating (MOG) for comparison [52]. While the DUS method directly identifies each fetal heartbeat for cardiac gating, the MOG method used in this study relies on mathematical optimization based on a two-parameter fetal heart rate model to identify the fetal heart rate. Potential disadvantages of the MOG method include the inability to fully account for the heart rate variability typically seen in fetuses [57, 58], and the long post-processing time required for image reconstruction.

The agreement between repeated measures of fetal blood flow using the DUS method was assessed by repeatedly acquiring phase-contrast flow images in six fetuses.

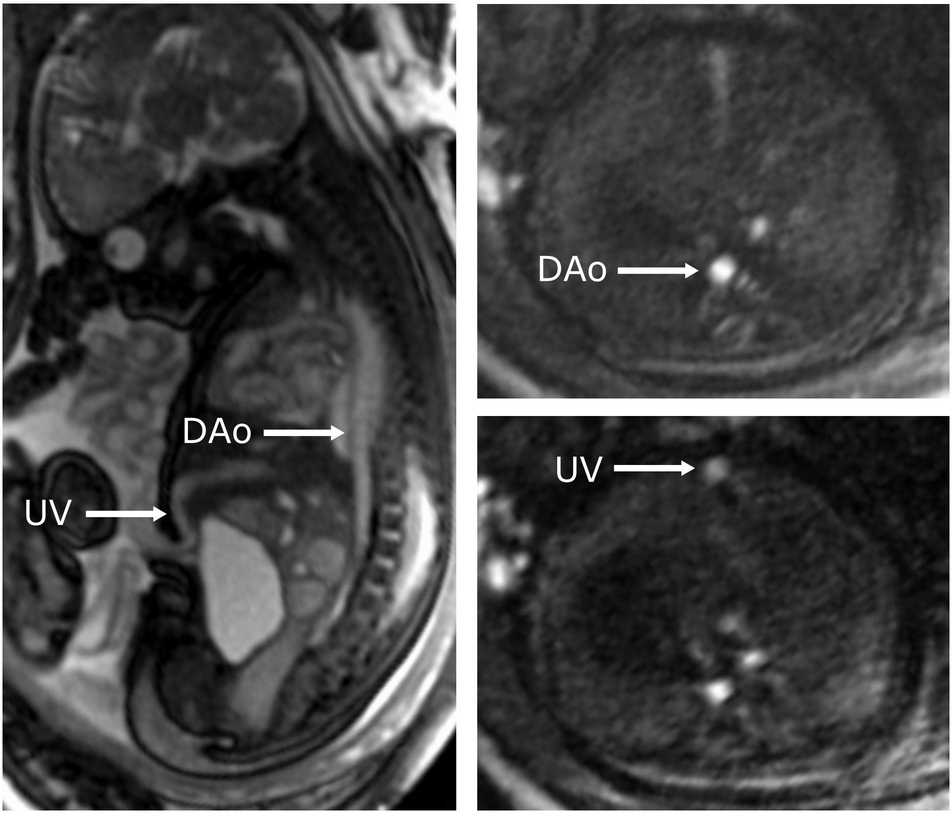

Figure 3.1: Acquisition of quantitative blood flow images. A sagittal fetal magnetic resonance image showing the fetal descending aorta (DAo) and umbilical vein (UV) is shown to the left. Corresponding cross-sectional images used for quantification of flow in the DAo and UV are shown to the right.

Image analysis

Four observers from two different centers quantified fetal blood flow by manual delineation in the phase-contrast images (Figure 3.2). Inter- and intra-observer variability were assessed for fetal flow measurements. Time-resolved vessel delineation with adjustment of the region of interest (ROI) to cover the vessel area in each time frame was compared with static delineation using the same ROI in all time frames. For static delineations, the ROI was defined to cover the vessel in the time frame with maximum vessel area. Furthermore, the effect of ROI size on measured flow was assessed using multiple circular ROIs with a diameter between 50 – 150% of the estimated vessel diameter.

Blood flow measurements were performed without background correction in general. For time-resolved delineations and for the effect of different ROI sizes on measured flow, measurements were performed both without and with linear background correction based on automatic identification of stationary tissue in the acquired flow images.

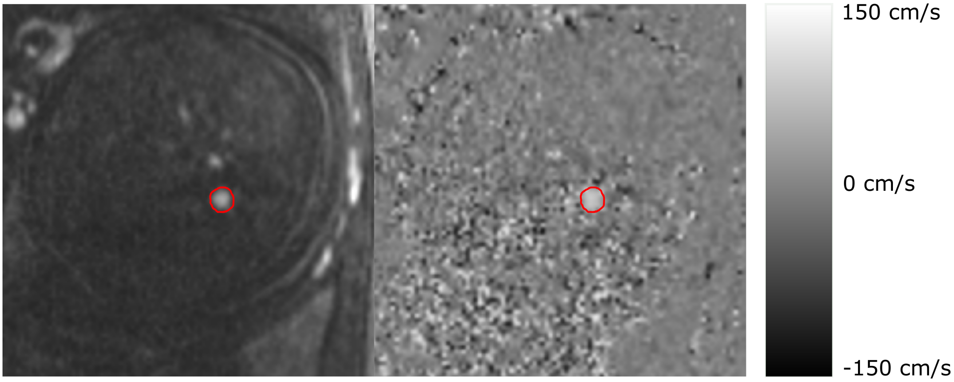

Figure 3.2: Measurement of fetal blood flow in quantitative flow images. Flow was measured by manually delineating the vessel of interest in the phase-contrast images. The figure shows the fetal descending aorta delineated in red, where the left image shows anatomy and the right image is the corresponding velocity map, where pixel intensity corresponds to velocity according to the velocity scale to the right.

Statistical analysis

Data are presented as median (range) or mean ± standard deviation. Bias and variability for DUS versus MOG differences and intra- and interobserver differences were defined as mean ± standard deviation and expressed in absolute values and in percent of average. Bland-Altman analysis was used to assess method and observer agreement. Coefficient of variation (CoV), defined as standard deviation divided by mean, was used to assess the agreement between repeated measurements of fetal blood flow by the DUS gating method.

3.4 Study II - Fetal volume quantification

Image acquisition and analysis

A 3D image slab covering the whole uterus was acquired for fetal volume quantification. Typical imaging parameters were 1.8x1.4x2.5 mm spatial resolution, TE/TR = 1.77/4.08 ms and flip angle=50°. All intrauterine structures (fetus, umbilical cord, placenta, and amniotic fluid) were manually delineated using a 3D pen tool with 3 – 4 mm diameter in Segment 3D print v 3.1 (Medviso AB, Lund, Sweden) (Figure 3.3). Manual segmentations were used as ground truth for neural network training and evaluation.

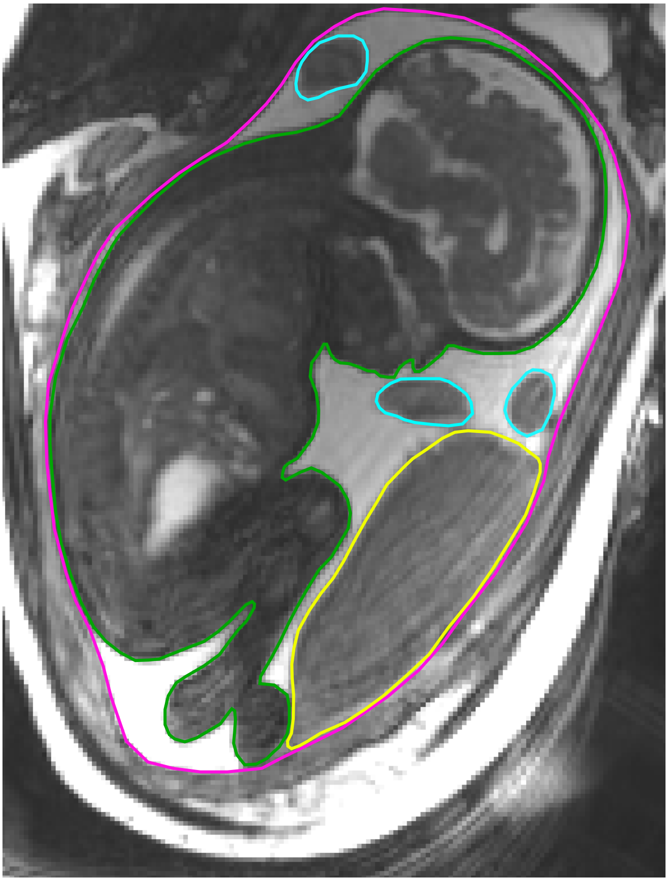

Figure 3.3: Delineation of intrauterine structures for volume quantification in magnetic resonance images. The image shows the fetus (green), placenta (yellow), umbilical cord (blue) and amniotic fluid (pink).

Artificial neural networks for fetal segmentation

A convolutional neural network with U-net structure was used, as previously suggested for automatic segmentation in medical images [59, 60]. The neural network used in this study was developed in a previous project, which contains a detailed description of the algorithm [60]. In short, the network was trained to classify each voxel in the input image as fetus, placenta, umbilical cord or amniotic fluid. A multi-task learning process including all intrauterine structures was used as this has been suggested to improve network performance by providing more information compared with a binary classification task of each pixel as fetus or non-fetus [61]. The two-dimensional U-net used in this study analyzes input images slice by slice in three orthogonal directions. The final classification of each voxel is determined by voxel-wise voting based on the outputs of all three orthogonal images containing the voxel. Training and hyperparameter optimization were performed by four-fold cross-validation using 15 datasets for training and 5 for validation for each iteration. A total of 42 fetuses were included, of which 20 were used for training and validation, and 22 for testing network performance. One of the 22 test datasets consisted of twin fetuses, and was used to assess the generalizability of the model, without comparison to manual segmentation.

Comparison with weight-estimation formulas commonly used in fetal ultrasound

Fetal volume by 3D magnetic resonance imaging (MRI) was multiplied with an assumed fetal density of 1.04 kg/dm^3 to estimate fetal weight [55]. Fetal weight was also estimated by Hadlock's formulas 1 – 4 [62, 63] and compared with 3D MRI-based measurements. Hadlock's formulas use measurements of fetal head circumference, biparietal diameter, abdominal diameter and femur length to estimate fetal weight, and were originally developed for ultrasound-based fetal weight estimation [62, 63]. In the current study, fetal biometric measurements were made using MR images instead (Figure 3.4).

Fetal blood flow indexed to fetal weight

Blood flow was measured in the umbilical vein and descending aorta in 15 and 20 fetuses respectively, and indexed to fetal weight measured by manual segmentation of the fetus.

Statistical analyses

Bland-Altman analysis was used to assess differences between manual and automatic fetal volume measurements and differences between fetal weight estimated using Hadlock's formulas and fetal weight measured by segmentation in magnetic resonance images respectively. The agreement between manual and automatic fetal segmentation was also assessed using Dice similarity coefficient, which is defined as as $\frac{2 \cdot |A| \cap |B|}{|A| + |B|}$ where A and B are two sets.

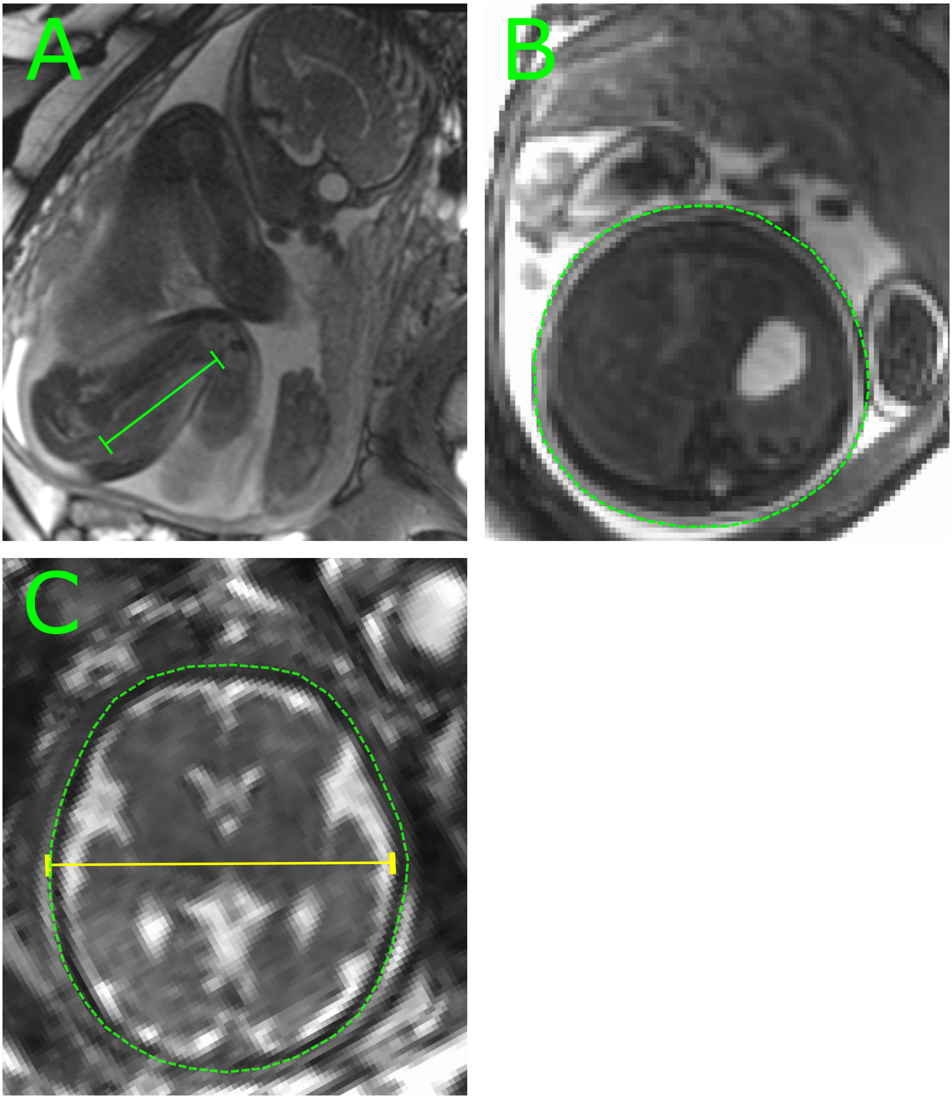

Figure 3.4: Measurement of fetal biometric parameters for weight estimation using Hadlock's formulas. The image shows measurements of femur length (**A**), abdominal circumference (**B**), and head circumference and biparietal diameter (**C**).

3.5 Study III - Assessment of congenital heart defects

Image acquisition

Cine images were acquired using a balanced steady-state free precession sequence with parameters 1.4 x 1.4 x 4 mm spatial resolution, 38 ms temporal resolution, flip angle 45°, and TE/TR 1.38/3.16 ms. The anatomy and function of the left and right ventricles were assessed using cine images (Figure 3.5). The anatomy of the great vessels was assessed using cine images and anatomical overview images (Figure 3.5). A T2-weighted image stack covering the fetal lungs was acquired, for assessment of the so-called nutmeg pattern which indicates pulmonary lymphangiectasia and a poor prognosis [64]. While this T2-weighted sequence is not a cardiovascular MR sequence per se, it is readily acquired during fetal CMR examination and provides valuable complementary information in cases of congenital heart defects with suspected restrictive or intact atrial septum.

Image evaluation

Images were evaluated in consensus by three observers including the referring pediatric cardiologist. The observers together had extensive experience in CMR and fetal cardiac ultrasound and had access to ultrasound images and reports. Fetal CMR was considered to have clinical utility if CMR examination provided additional diagnostic information. Findings by fetal CMR were compared with findings by postnatal cardiac ultrasound.

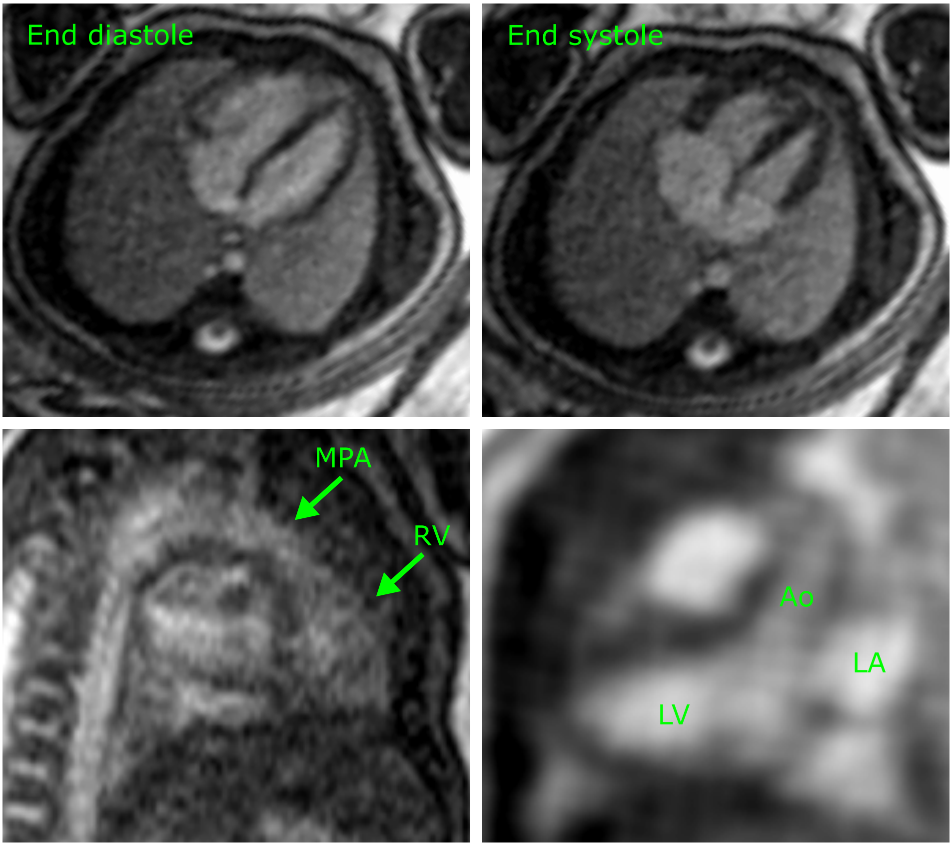

Figure 3.5: Assessment of cardiovascular anatomy and function. The top images show a fetal four-chamber view in end-diastole (**left**) and end-systole (**right**), in this case showing a normal systolic function. The bottom images show the right and left ventricular outflow tracts. Normal connections of the main pulmonary artery to the right ventricle (**left**) and aorta to the left ventricle (**right**) are seen. *Ao, aorta; LA, left atrium; LV, left ventricle; MPA, main pulmonary artery; RV, right ventricle.*

3.6 Study IV - Super-resolution image reconstruction for fetal CMR

Data for network training, validation and testing

Two types of datasets were used for neural network training and testing; 1) fully sampled standard clinical images and acquired low-resolution images in the same fetus; and 2) low-resolution images synthesized from fully sampled standard clinical images. Low-resolution images with a spatial resolution in the phase-encoding direction (phase resolution) of 25%, 33% and 50% of that of the standard clinical sequence were used. The training dataset consisted of 36 cine image slices from 14 fetuses, resulting in a total of 1080 images. The validation dataset consisted of three cine image slices from 3 fetuses, resulting in a total of 90 images. The test dataset consisted of 67 cine image slices from 11 fetuses, resulting in a total of 2010 images. The datasets used for training, validation and testing had no overlap.

Reconstruction methods

Proportions in low-resolution input images were restored using nearest neighbor interpolation. Two super-resolution neural networks were used, called phasrresnet and phasrGAN [65]. The phasrresnet is based on a single convolutional neural network, whereas the phasrGAN consists of multiple neural networks in a *generative adversarial network model*, as described below. In addition, the common reconstruction methods bicubic interpolation and k-space zeropadding were used for comparison.

Generative adversarial model

The details of the artificial neural networks used in this study are described in *paper IV* [65]. This section will describe the main principles of the phasrGAN model. A generative adversarial neural network was used to generate high-resolution images from the low-resolution input images described above. This model consists of two different main networks. One of those networks is called the generator. The generator is a neural network which creates new information. In this case, the goal of the generator is to add information to a low-resolution fetal CMR image, to make the image appear as a true high-resolution fetal CMR image. However, in order to learn this task, the generator needs feedback on its performance. This is provided by the second network, called the discriminator. The discriminator is a classifier network which receives labeled generator-produced images and true high-resolution fetal CMR images as training data and is trained to classify those images accordingly.

In the network training process, low-resolution fetal CMR input images are processed by the generator (Figure 3.6). The generator outputs forged images with high resolution which are used as input to the discriminator network. The discriminator also receives true acquired high-resolution fetal CMR images as input. For each input image, the discriminator outputs a probability that the input image is a true high-resolution fetal CMR image.

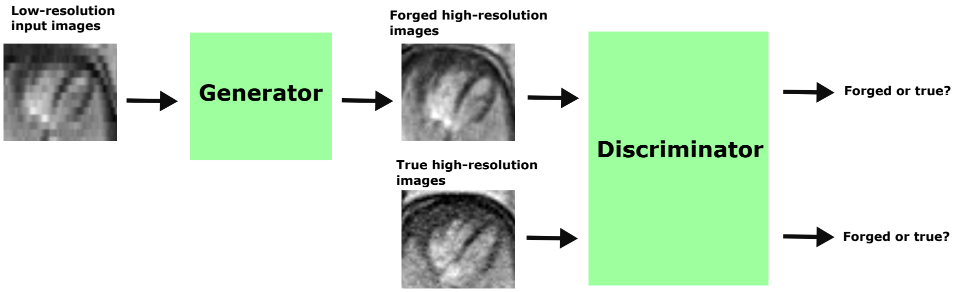

Figure 3.6: Generative adversarial network for increasing image resolution. Low-resolution images are used as input to the generator network, which adds information in these images, resulting in forged high-resolution images. Forged and true high-resolution images are used as input to the discriminator. The discriminator is a classifier neural network which is trained to classify input images as forged or true. The training process can be seen as a competition between the generator and discriminator, where the generator is trained to fool the discriminator, and the discriminator is trained to correctly identify forged images produced by the generator.

The discriminator has a cost function which returns a high cost if the discriminator outputs a low probability for the correct class of the input image. The generator on the other hand has a cost function which returns higher values the more confidently the discriminator predicts that the generator-produced image is indeed a forged high-resolution image. The generator and discriminator are therefore trained in a competitive way; the parameters of the generator network are optimized to fool the discriminator, while the parameters of the discriminator network are optimized to recognize the forged images from the generator.

Image evaluation

Images in the test set were qualitatively assessed by three observers. Each observer scored the images from 1 – 10 based on image quality, taking into account the visibility of cardiac structures throughout the cardiac cycle and any potential artifacts interfering with the assessment of cardiac anatomy and function. Any pathology in reconstructed images which was not present in the fully sampled standard clinical images was noted, as well as pathology in the fully sampled standard clinical images which was not present in the reconstructed images.

In addition to qualitative assessment, the reconstruction of low-resolution images were assessed objectively using mean squared error (MSE), peak signal to noise ratio (PSNR) and structural similarity index measure (SSIM). This was performed by down-sampling the fully sampled test set data and subsequently reconstructing the down-sampled images using the methods described above. Mean squared error, PSNR and SSIM were calculated for the reconstructed images versus the fully sampled images.

Statistical analyses

For each reconstruction method, image scores were compared to the standard clinical images using Mann-Whitney's non-parametric test. Each reconstruction method was compared to the phasrGAN method with respect to MSE, PSNR and SSIM using Mann-Whitney's non-parametric test. P-values < 0.05 were considered statistically significant. Data are presented as median (interquartile range).

Chapter 4

Results and comments

4.1 Study I - Quantification of fetal blood flow

Flow curve profiles

Figure 4.1 shows typical flow curves in the descending aorta (DAo) and umbilical vein (UV) for the Doppler ultrasound (DUS) and metric optimized gating (MOG) methods respectively, acquired in the same fetus. The DAo shows a pulsatile flow profile while the UV shows a constant flow profile, as can be expected [66, 67]. Moreover, a higher peak flow is seen in the DAo using the DUS method. Underestimation of peak flow occurs with imperfect gating, and has previously been reported for the MOG method in phantom experiments [68]. Thus, the DUS gating method could potentially be more accurate than MOG in measuring peak flow and capturing the flow curve profile.

DUS gating versus MOG for fetal blood flow quantification

Flow in the DAo was 726 (348 – 1130) ml/min using DUS gating and 708 (440 – 1170) ml/min using MOG. Flow in the UV was 366 (150 – 782) ml/min using DUS gating and 404 (147 – 697) ml/min using MOG. Measurements without and with linear background correction showed a bias and variability for the DUS and MOG methods respectively of – 17 ± 42 ml/min (– 3 ± 6%) and – 17 ± 43 ml/min (– 3 ± 6%) in the DAo, and 33 ± 41 ml/min (8 ± 12%) and 43 ± 42 ml/min (14 ± 17%) in the UV. Figure 4.2 shows Bland-Altman plots for flow quantified in the DAo and UV using the DUS and MOG methods respectively. Bias and variability for DAo flow using the DUS and MOG methods were – 45 ± 122 ml/min (– 6 ± 15%) for time-resolved delineations and – 23 ± 112 ml/min (– 2 ± 14%) for static delineations. Bias and variability for UV flow using the DUS and MOG methods were 19 ± 136 ml/min (2 ± 24%) for time-resolved delineations and 9 ± 103 ml/min (0 ± 23%) for static delineations.

The agreement between the DUS and MOG methods was thus good in terms of bias, although measurements showed a high variability. One potential reason for the observed

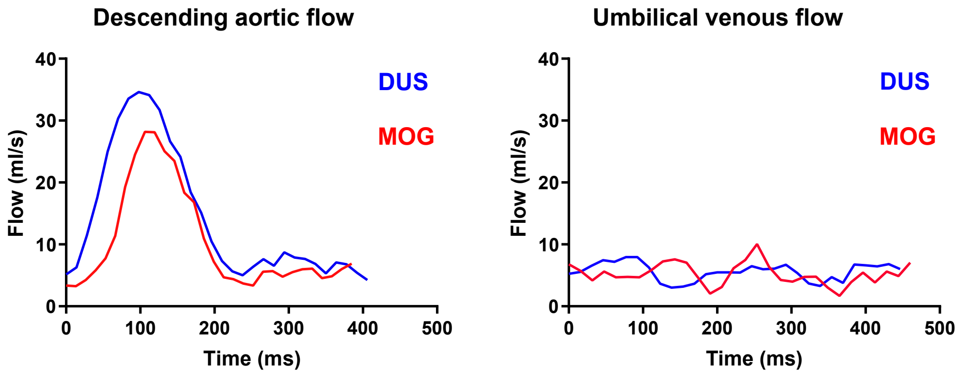

Figure 4.1: Flow curves. The graphs show flow curves in the fetal descending aorta (**left**) and umbilical vein (**right**) using Doppler ultrasound gating (DUS) and metric optimized gating (MOG). *Modified and used with permission from Salehi et al. Journal of Cardiovascular Magnetic Resonance 2019. Springer Nature. https://doi.org/10.1186/s12968-019-0586-8 – Creative commons attribution 4.0 international license (http://creativecommons.org/licenses/by/4.0/)*

variability is that it was not possible to record the DUS gating signal simultaneously with acquisition of MOG data. Instead, image acquisition using DUS gating was performed after image acquisition using MOG. This may have caused differences in measured flow due to physiological fetal blood flow variation over time or due to measurement error caused by fetal movement between acquisitions. While bias and variability were low for flow measurements without and with linear background correction in this study, the optimal method for background correction in fetal flow measurements is unknown. In the current study, pixels with a phase variation over the cardiac cycle below a certain threshold were automatically classified as stationary tissue and used for background correction. However, the choice of stationary tissue for background correction presents a challenge in fetal cardiovascular magnetic resonance (CMR). Specifically, fetal movement could potentially affect the phase of fetal static tissue or amniotic fluid. Therefore, future studies are warranted to elucidate if and how background correction should be performed in fetal phase-contrast flow images.

Agreement of repeated fetal blood flow measurements using DUS gating

Figure 4.3 shows repeated fetal blood flow measurements in the DAo and UV in six fetuses. Figure 4.4 shows CoV for repeated measurements in each fetus. Repeated flow measurements generally showed similar values however in some cases with substantial variability, particularly in the UV.

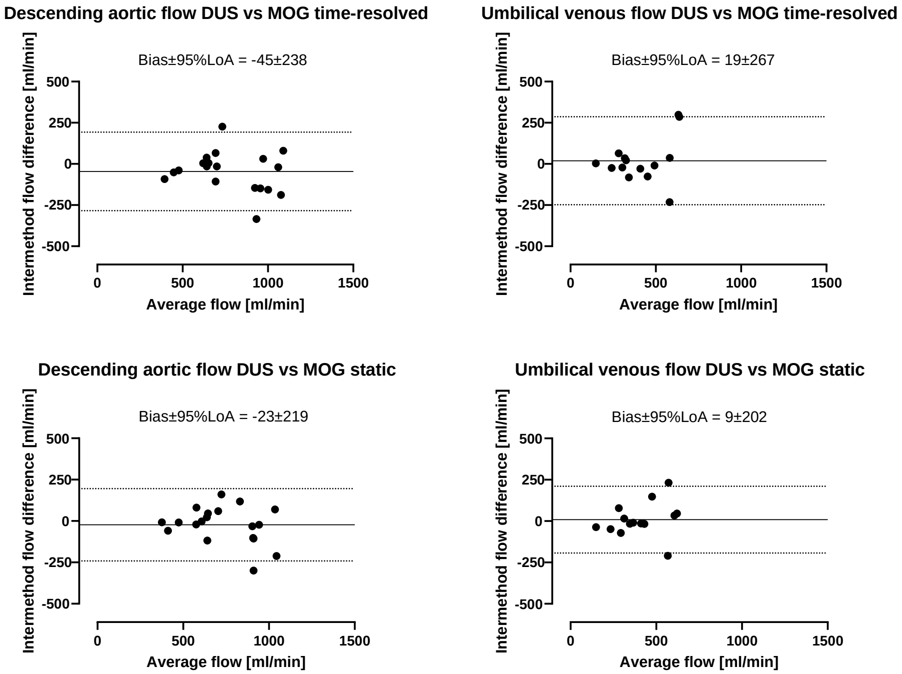

Figure 4.2: Flow quantification using Doppler ultrasound (DUS) gating versus metric optimized gating (MOG). The graphs show Bland-Altman plots for quantification of fetal blood flow using DUS gating versus MOG in the descending aorta (**left**) and umbilical vein (**right**) using time-resolved (**top**) and static (**bottom**) vessel delineations. Bias and 95% limits of agreement (LoA) are indicated by solid and dashed lines respectively. *Used with permission from Salehi et al. Journal of Cardiovascular Magnetic Resonance 2019. Springer Nature. https://doi.org/10.1186/s12968-019-0586-8 – Creative commons attribution 4.0 international license (http://creativecommons.org/licenses/by/4.0/).*

The variability in measured flow can be explained both by physiological variability in flow and by measurement error e.g. due to fetal movement or background phase errors. Heating of gradient coils during prolonged activation has been shown to cause temperature-dependent background phase errors in phase-contrast flow images [69]. Therefore, the repeating of phase-contrast flow acquisitions in this study could potentially have introduced increasing background phase errors, thereby confounding the assessment of physiological flow variability. However, previous experimental studies on the fetal lamb have shown

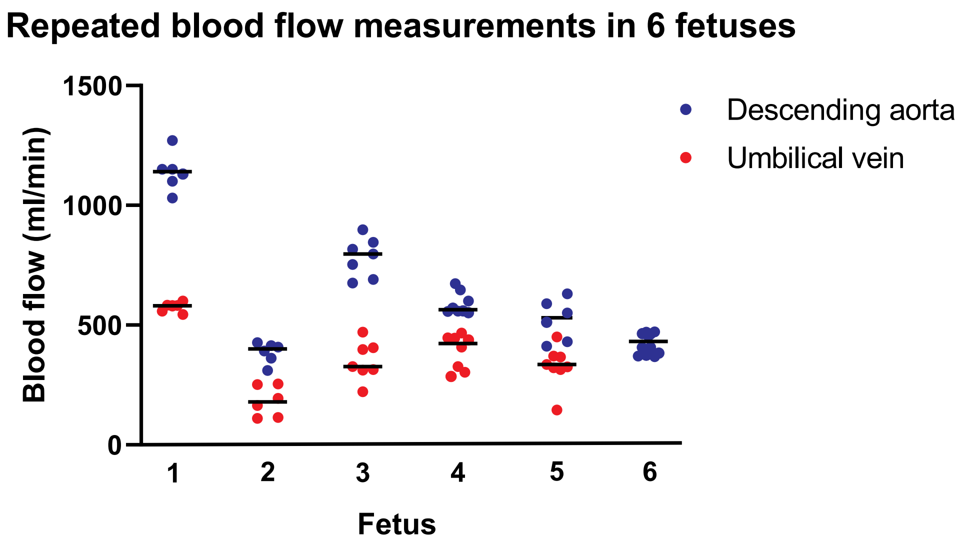

Figure 4.3: Repeated blood flow measurements in six fetuses. Flow images were acquired between 6 and 12 times in six fetuses. For each image acquisition, blue circles show flow values in the descending aorta (DAo) and red circles show flow values in the umbilical vein (UV). Medians are indicated by solid lines. Flow acquisition in the UV was not successful in fetus 6. *Modified and Used with permission from Salehi et al. Journal of Cardiovascular Magnetic Resonance 2019. Springer Nature. https://doi.org/10.1186/s12968-019-0586-8 – Creative commons attribution 4.0 international license (http://creativecommons.org/licenses/by/4.0/)*

significant fetal DAo flow variability, occurring in conjunction with fetal respiratory movements [70]. Furthermore, marked decreases in UV flow have been demonstrated in conjunction with certain patterns of respiratory movements in the fetal lamb [71]. Therefore, by averaging flow over multiple acquisitions in the same fetus, more representative flow values could potentially be obtained. This should be considered in future studies aiming to compare physiology in different patient categories.

The effect of region of interest size

Figure 4.5 shows the effect of ROI size on measured flow. An ROI smaller than vessel size underestimated flow, whereas an ROI larger than vessel size overestimated flow, both without and with linear background correction. The underestimation caused by a smaller ROI was relatively larger than the overestimation caused by a larger ROI.

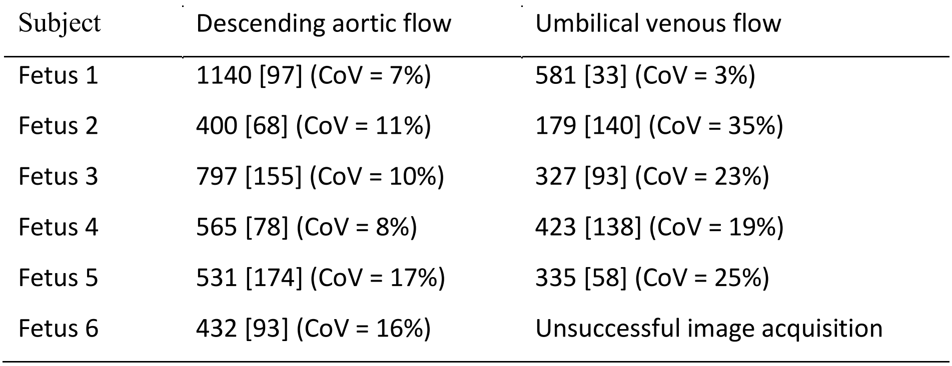

Subject	Descending aortic flow	Umbilical venous flow
Fetus 1	1140 [97] (CoV = 7%)	581 [33] (CoV = 3%)
Fetus 2	400 [68] (CoV = 11%)	179 [140] (CoV = 35%)
Fetus 3	797 [155] (CoV = 10%)	327 [93] (CoV = 23%)
Fetus 4	565 [78] (CoV = 8%)	423 [138] (CoV = 19%)
Fetus 5	531 [174] (CoV = 17%)	335 [58] (CoV = 25%)
Fetus 6	432 [93] (CoV = 16%)	Unsuccessful image acquisition

Figure 4.4: Repeatability of blood flow measurements. Flow values are presented as median [IQR] and CoV. *Modified and Used with permission from Salehi et al. Journal of Cardiovascular Magnetic Resonance 2019. Springer Nature. https://doi.org/10.1186/s12968-019-0586-8 – Creative commons attribution 4.0 international license (http://creativecommons.org/licenses/by/4.0/)*

These results are in agreement with a previous study by Arheden et al [42]. In that study, the effect of ROI size on measured flow was assessed in a small-vessel flow phantom where the true vessel size and flow was known from the experimental setup. Flow quantification was accurate when ROI size equaled vessel size. With increasing ROI sizes up to several times larger than vessel area, the overestimation of flow was approximately 20%. On the other hand, ROI sizes smaller than vessel area resulted in larger underestimation of flow.

These results highlight the challenges of flow quantification in small vessels, where partial volume effects may introduce measurement error [46, 47]. Ideally, the ROI size should be equal to vessel size. If there is uncertainty of vessel size, it may be recommended to use a slightly larger ROI for flow quantification, as this results in relatively smaller error compared to a smaller ROI.

Time-resolved versus static vessel delineation

Figure 4.6 shows Bland-Altman plots for time-resolved versus static vessel delineations for measurement of fetal DAo and UV flow. For the DAo, bias and variability for time-resolved versus static vessel delineations were 33 ± 39 ml/min (4 ± 6%) for the DUS method and 56 ± 55 ml/min (7 ± 7%) for the MOG method. For the UV, bias and variability for time-resolved versus static vessel delineations were 11 ± 84 ml/min (2 ± 15%) for the DUS method and 1 ± 44 ml/min (0 ± 10%) for the MOG method.

Both bias and variability for static versus time-resolved delineations were low. However, time-resolved manual delineations are time-consuming compared to static delineations.

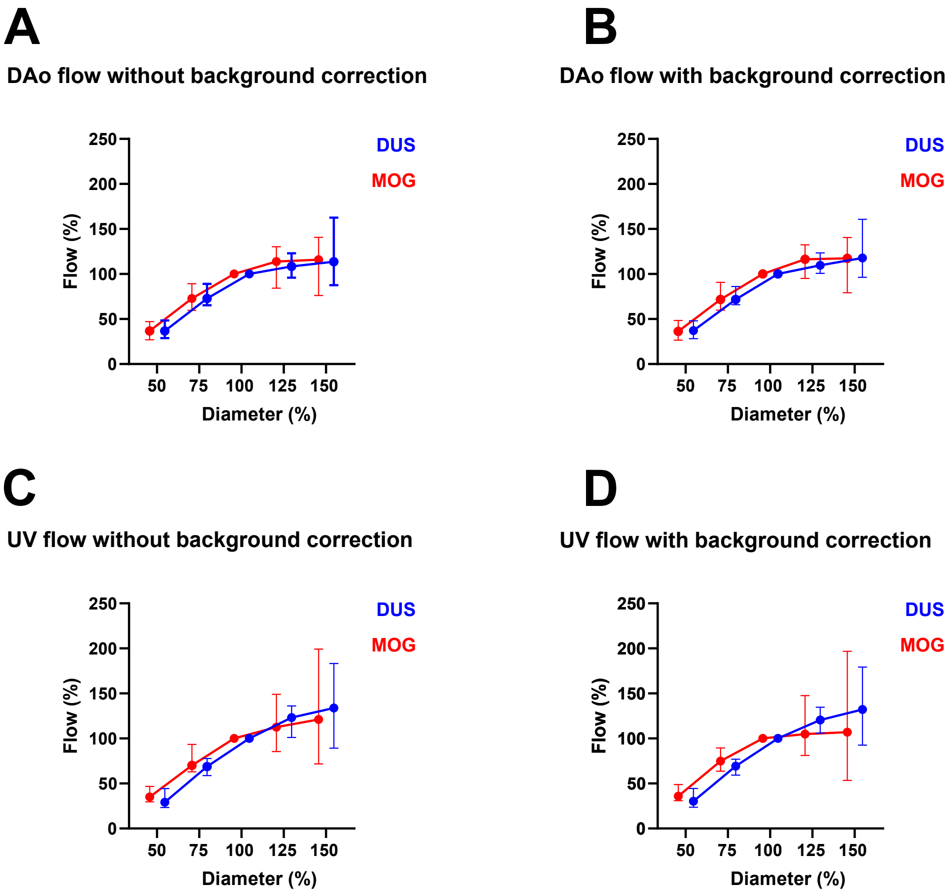

Figure 4.5: Graphs show flow in the descending aorta (**top**) and umbilical vein (**bottom**) using Doppler ultrasound gating (DUS) and metric optimized gating (MOG) measured with region of interest sizes from 50% to 150% of estimated vessel diameter, without background correction (**left**) and with linear background correction (**right**). For each vessel diameter, circles and error bars represent median and range. Flow is overestimated when the region of interest size is larger than estimated vessel size, and underestimated when region of interest size is smaller than estimated vessel size. *Modified and Used with permission from Salehi et al. Journal of Cardiovascular Magnetic Resonance 2019. Springer Nature, https://doi.org/10.1186/s12968-019-0586-8 – Creative commons attribution 4.0 international license (http://creativecommons.org/licenses/by/4.0/).*

Therefore, static delineations may be recommended for quantification of blood flow in the fetal DAo and UV.

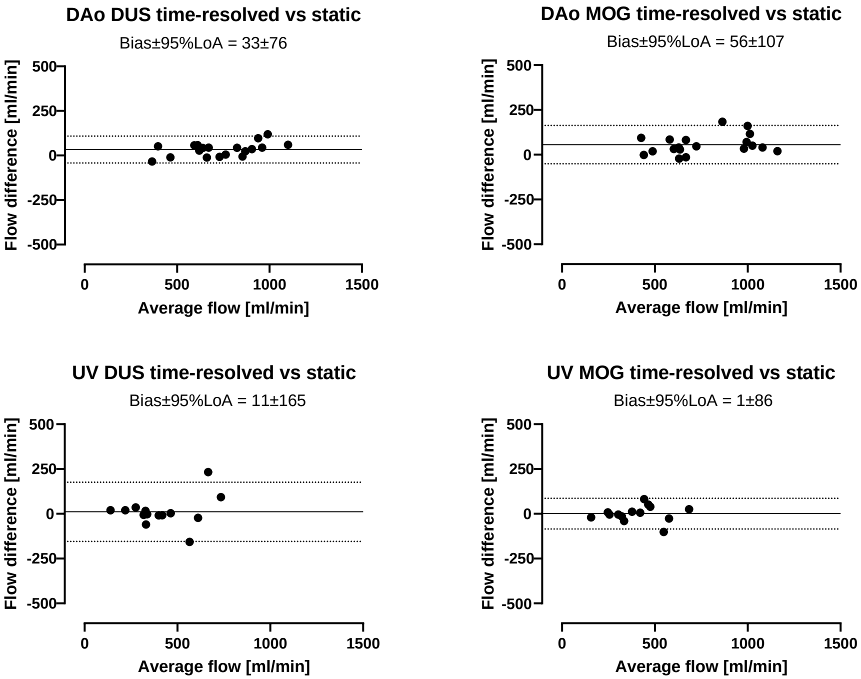

Figure 4.6: Time-resolved versus static vessel delineations. Bland-Altman plots for fetal blood flow measurements in the descending aorta (**top**) and umbilical vein (**bottom**) using Doppler ultrasound (DUS) gating (**left**) and metric optimized gating (**right**) for time-resolved versus static vessel delineations. Solid and dashed lines indicate bias and 95% limits of agreement (LoA) respectively. *Used with permission from Salehi et al. Journal of Cardiovascular Magnetic Resonance 2019. Springer Nature. https://doi.org/10.1186/s12968-019-0586-8 – Creative commons attribution 4.0 international license (http://creativecommons.org/licenses/by/4.0/).*

Intra- and interobserver variability for fetal blood flow measurements

Figure 4.7 shows intraobserver variability of blood flow measurements in the fetal DAo and UV. Figure 4.8 shows interobserver variability of blood flow measurements in the fetal DAo and UV. Intraobserver variability was low. Interobserver variability was low for observers

1 – 3 whereas observer 4 systematically underestimated flow compared to observers 1 – 3. This highlights the need for consensus on vessel delineation between observers and centers.

Vessel and gating method	Time-resolved delineations	Static delineations
Descending aorta DUS	19 ± 54 ml/min (2 ± 7%)	-15 ± 96 ml/min (-2 ± 13%)
Descending aorta MOG	32 ± 55 ml/min (4 ± 6%)	17 ± 59 ml/min (2 ± 9%)
Umbilical vein DUS	-10 ± 73 ml/min (-3 ± 13%)	-31 ± 62 ml/min (-5 ± 11%)
Umbilical vein MOG	-2 ± 26 ml/min (-1 ± 8%)	25 ± 67 ml/min (8 ± 17%)

Figure 4.7: Intraobserver variability. Intraobserver variability is presented as mean differences ± standard deviation in absolute values and in percent of average measured flow.

Time-resolved delineations

Vessel and method	Observer 1 vs 2	Observer 1 vs 3	Observer 1 vs 4	Observer 3 vs 4
Descending aorta DUS	37 ± 65 (5 ± 8%)	0 ± 64 (0 ± 9%)	175 ± 87 (26 ± 9%)	175 ± 80 (26 ± 8%)
Descending aorta MOG	35 ± 62 (4 ± 8%)	-3 ± 80 (0 ±9%)	198 ± 99 (28 ± 10%)	201 ± 111 (28 ± 10%)
Umbilical vein DUS	16 ± 98 (4 ± 20%)	2 ± 84 (-2 ± 23%)	69 ± 71 (17 ± 14%)	67 ± 43 (19 ± 14%)
Umbilical vein MOG	26 ± 71 (4 ± 21%)	-9 ± 48 (-3 ± 13%)	75 ± 61 (18 ± 19%)	85 ± 71 (20 ± 15%)

Static delineations

Vessel and method	Observer 1 vs 2	Observer 1 vs 3	Observer 1 vs 4	Observer 3 vs 4
Descending aorta DUS	-17 ± 66 (-2 ± 11%)	-43 ± 55 (-5 ± 7%)	98 ± 107 (15 ± 17%)	142 ± 125 (21 ± 17%)
Descending aorta MOG	-13 ± 64 (-2 ± 8%)	-85 ± 88 (-10 ± 9%)	63 ± 114 (9 ± 14%)	148 ± 152 (20 ± 16%)
Umbilical vein DUS	4 ± 66 (2 ± 16%)	-30 ± 69 (-9 ± 23%)	24 ± 83 (6 ± 19%)	53 ± 61 (15 ± 20%)
Umbilical vein MOG	17 ± 86 (2 ± 22%)	7 ± 88 (2 ± 21%)	45 ± 88 (13 ± 24%)	38 ± 64 (11 ± 19%)

Figure 4.8: Interobserver variability for flow quantified using time-resolved and static vessel delineations. Interobserver variability is presented as mean differences ± standard deviation in absolute values and in percent of average. DUS, Doppler ultrasound gating; MOG, metric optimized gating. *Modified and used with permission from Salehi et al. Journal of Cardiovascular Magnetic Resonance 2019. Springer Nature. https://doi.org/10.1186/s12968-019-0586-8 – Creative commons attribution 4.0 international license (http://creativecommons.org/licenses/by/4.0/)*

Summary

Study I evaluated fetal blood flow quantification by phase-contrast CMR using a recently developed Doppler ultrasound device for cardiac gating. This method is feasible and shows a low bias compared to the previous CMR reference method metric optimized gating. Repeated flow measurements in the same fetus generally show similar values, however with substantial variability in some cases. The size of the region of interest affects measured flow, and a region of interest size similar to or slightly larger than vessel size can be recommended. Consensus on vessel delineation is needed for reproducible measurements between observers.

4.2 Study II - Fetal volume quantification

Automatic versus manual fetal segmentation

Median fetal volume was 2759 ml (range 1824 – 3895 ml). Figure 4.9 shows examples of 3D models by automatic and manual fetal segmentation respectively. Figure 4.10 shows 3D models from automatic segmentation of twin fetuses as a test of the generalizability of the model. Figure 4.11 shows a Bland-Altman plot for automatic versus manual quantification of fetal volume. Bias and 95% limits of agreement were -4.5±351 ml (0.01%±11%). Dice similarity index for automatic and manual segmentation was 0.94 ±0.02. The time required for manual segmentation was approximately 1 – 2 hours per case. In contrast, the time required for automatic segmentation typically was 45 seconds per case. The agreement between automatic and manual fetal segmentation was good. Furthermore, automatic segmentation typically saves approximately 1 – 2 hours per case. Therefore, the automatic method makes fetal volume quantification using high-resolution magnetic resonance (MR) images clinically feasible.

Hadlock's formulas versus fetal segmentation

Figure 4.12 shows Bland-Altman plots for fetal weight estimated by Hadlock's formulas 1 – 4 versus fetal weight estimated by fetal segmentation. Bias and limits of agreement for Hadlock's formulas 1 – 4 versus fetal segmentation were 108±435g (3%±14%), 211±468g (7%±15%), 106±425g (4%±14%) and 179±472g (6%±15%), respectively.

The agreement between Hadlock's formulas and fetal segmentation was generally good, however with significant differences in individual cases. In particular, previous studies have found Hadlock's formulas to be less accurate for small and large fetuses [72]. Therefore, there is a need for improved methods for fetal weight estimation. Estimation of fetal weight using high-resolution MR images could potentially improve the detection of small and large fetuses and thereby have an impact on clinical decision-making.

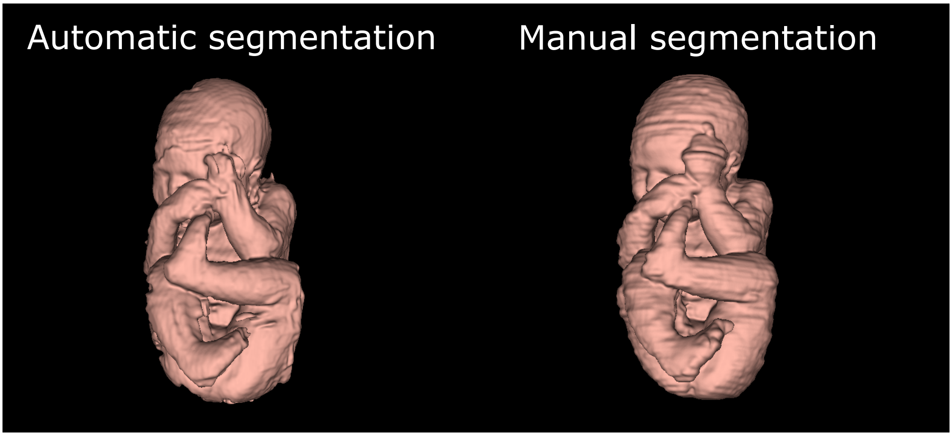

Figure 4.9: Automatic versus manual segmentation of the fetus.

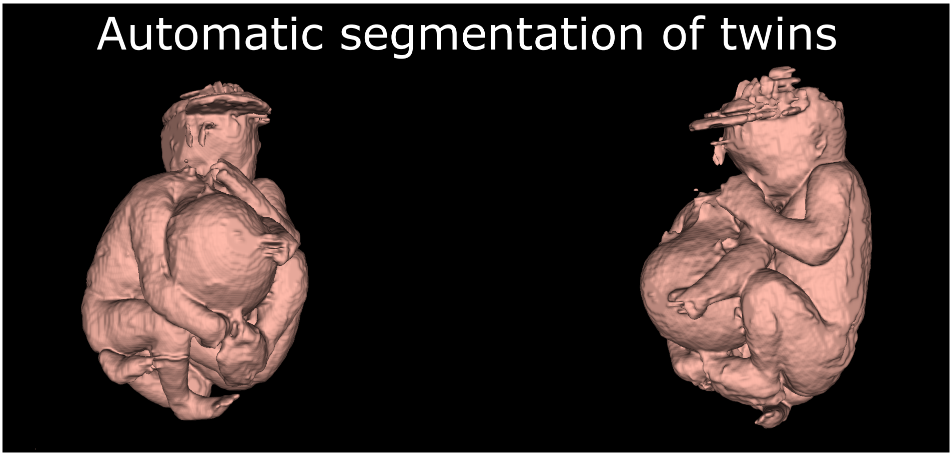

Figure 4.10: Automatic segmentation of twin fetuses. The 3D models show automatic segmentations of twin fetuses from two different angles. The incorrect segmentation at the fetal head is caused by artifacts in the MR images.

Fetal blood flow indexed to fetal weight

Absolute and indexed fetal blood flow values are shown in Figure 4.13. Median umbilical venous flow was 406 ml/min (range 151 – 650 ml/min) in absolute values and 162 ml/min/kg (range 52 – 220 ml/min/kg) indexed to fetal weight. Median descending aortic

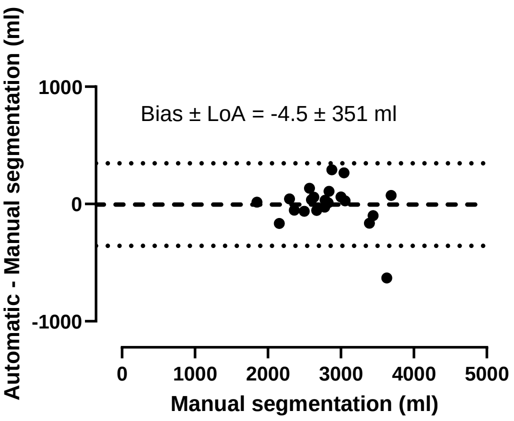

Figure 4.11: Automatic versus manual fetal segmentation. Bland-Altman plot for automatic versus manual fetal segmentation, with manual segmentation used as reference. The dashed and dotted lines indicate bias and 95% limits of agreement (LoA) respectively

flow was 763 ml/min (range 481 – 1160 ml/min) in absolute values and 276 ml/min/kg (range 189 – 386 ml/min/kg) indexed to fetal weight.

Note the different relationship between absolute blood flow versus fetal weight and indexed blood flow versus fetal weight (Figure 4.13). This illustrates how indexed fetal flow may reduce the confounding effects of fetal weight on flow. As blood flow may be dependent on both weight and pathology, indexed flow measurements could potentially more accurately depict underlying pathology.

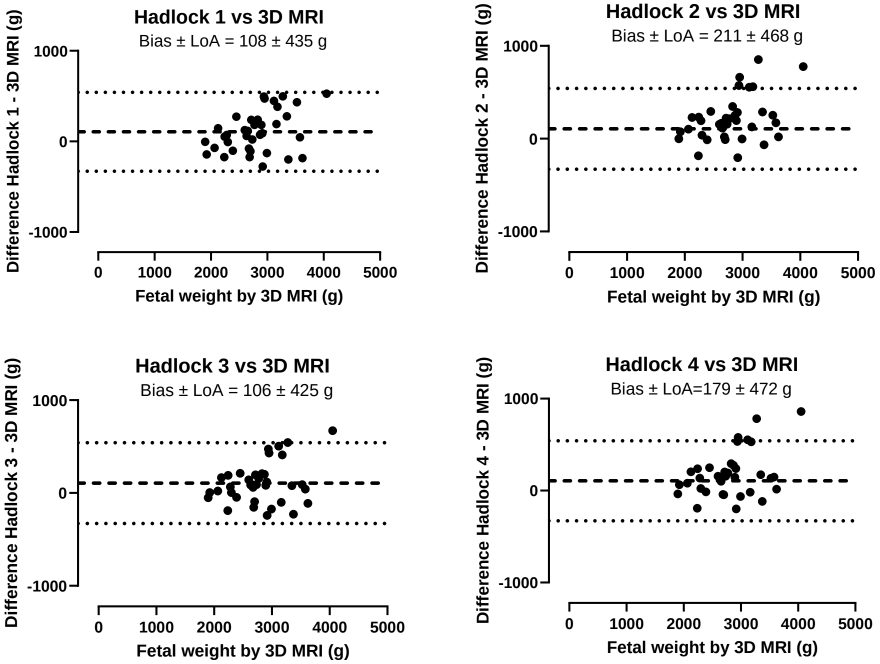

Figure 4.12: Hadlock's formulas 1 – 4 versus fetal segmentation. Bland-Altman plots for fetal weight estimated using Hadlock's formulas 1 – 4 versus fetal weight estimated using 3D magnetic resonance imaging (MRI) as reference. Dashed and dotted lines indicate bias and 95% limits of agreement (LoA) respectively.

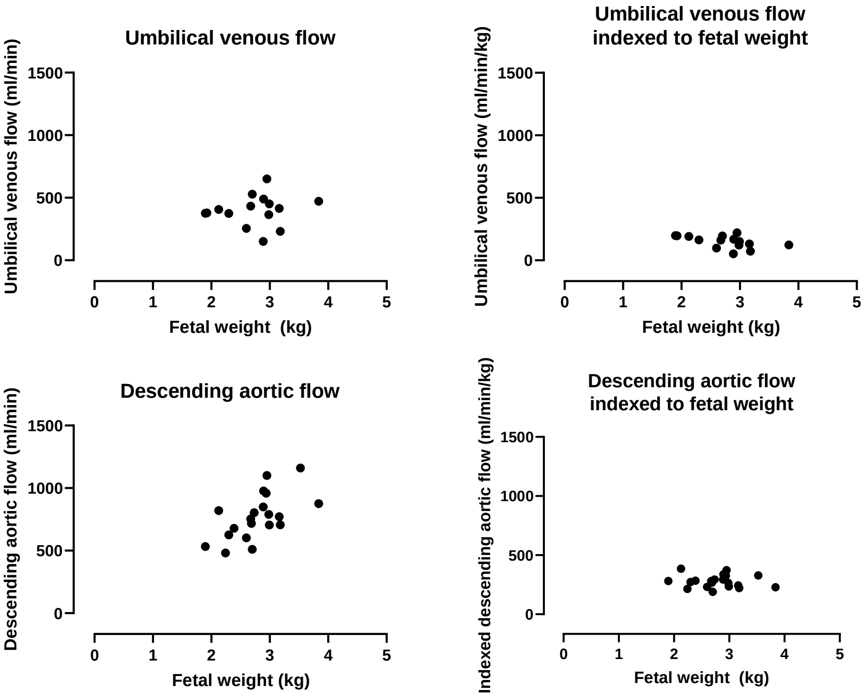

Figure 4.13: Fetal blood flow indexed to fetal weight. Graphs show fetal blood flow in the umbilical vein (**top**) and descending aorta (**bottom**) in absolute values (**left**) and indexed by weight (**right**) on the y-axis and fetal weight on the x-axis. Note the different relationships between absolute and indexed blood flow versus fetal weight.

Summary

Study II applied artificial neural networks for automatic quantification of fetal volume in high-resolution MR images. The automatic method is accurate and requires approximately 45 seconds per fetus, whereas manual measurements require 1 – 2 hours. Therefore, automatic fetal volume measurements with the suggested method are clinically feasible. Fetal volume can be used to estimate fetal weight, which is an important factor for interpretation of blood flow measurements and delivery planning.

4.3 Study III - Assessment of congenital heart defects

A detailed case by case description of all included patients is provided in the Appendix. Four main non-exclusive categories of cases referred for fetal CMR were identified. Fetuses in the first category were referred for assessment of aortic arch anatomy. The second category included fetuses with borderline left ventricle, unbalanced atrioventricular septal defect or pulmonary atresia with intact ventricular septum referred for prediction of biventricular versus univentricular outcome. The third category consisted of fetuses with hypoplastic left heart syndrome referred for assessment of signs of restrictive or intact atrial septum. The fourth and final category included cases where fetal CMR provided information for parental counseling. Typical case descriptions and a general discussion for each category are provided below.

Assessment of aortic arch anatomy

This category included 20 patients referred mainly for risk assessment regarding aortic coarctation (see cases 3, 6-10, 12-13, 18-27, 28 and 31 in Supplementary Table 1 in the Appendix). In 16 of those cases, fetal CMR added diagnostic information. In four of those 16 cases, fetal CMR showed normal aortic anatomy and the suspicion of aortic coarctation could be dismissed. Although fetal CMR provided additional information in the remaining twelve cases, aortic coarctation could not be ruled out. Figure 4.14 shows a case where fetal CMR showed a normal aortic anatomy in a fetus where aortic arch hypoplasia and coarctation was suspected at fetal ultrasound examination.

Aortic coarctation is a potentially duct dependent congenital heart defect and can be life-threatening for the newborn [73]. If aortic coarctation is suspected in a fetus, it is crucial that delivery take place in a tertiary hospital with specialized pediatric cardiac care readily available. Prenatal risk assessment regarding aortic coarctation presents a challenge as coarctation can develop after birth without being apparent in the fetus [74, 75]. Currently known prenatal risk factors for aortic coarctation include a narrow aortic arch and/or isthmus and a small left ventricle [74, 75]. However, current risk stratification methods show suboptimal results [74, 75]. Therefore, improved methods for prenatal diagnosis are needed. Future studies will determine whether new fetal CMR biomarkers including blood flow measurements can improve prenatal detection of incipient aortic coarctation.

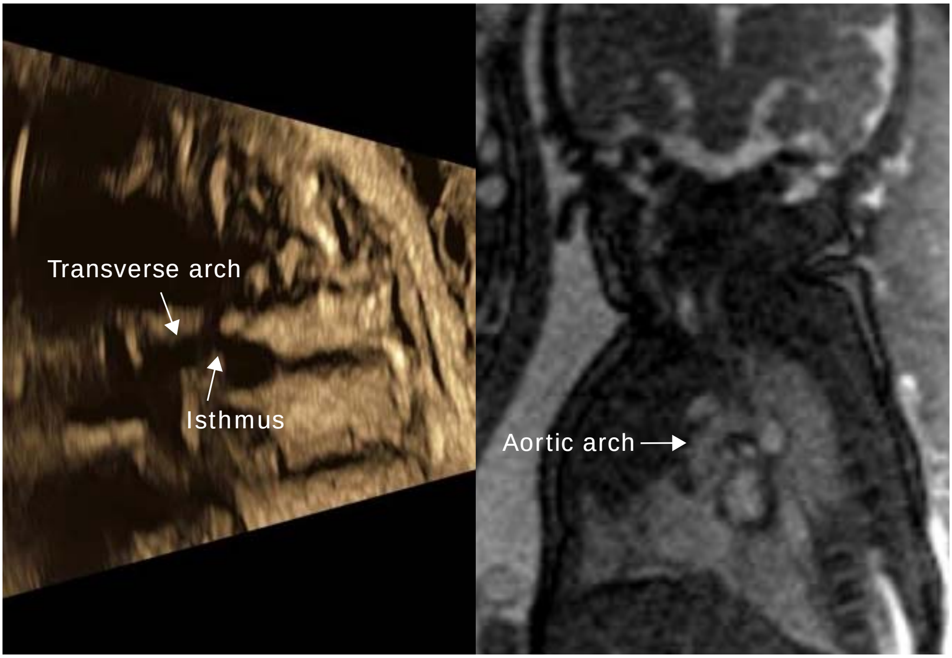

Figure 4.14: Assessment of the fetal aortic arch. Aortic arch hypoplasia and coarctation was suspected at fetal ultrasound examination (**left**). A normal anatomy of the aorta was demonstrated by fetal CMR (**right**). Cardiovascular magnetic resonance imaging findings were confirmed by postnatal ultrasound examination. *Modified and used with permission from Ryd et al. "Utility of Fetal Cardiovascular Magnetic Resonance for Prenatal Diagnosis of Complex Congenital Heart Defects". JAMA Network Open 2021. American medical association. https://doi.org/10.1001/jamanetworkopen.2021.3538 – CC-BY license.*

Prediction of biventricular versus univentricular outcome

This category included a total of 15 patients with borderline left ventricle, unbalanced atrioventricular septal defect or pulmonary atresia with intact ventricular septum (see cases 3-4, 6, 8, 13-17, 20, 24-27 and 29 in Supplementary Table 1 in the Appendix). Prediction of biventricular versus univentricular outcome requires estimation of atrioventricular valve annulus diameter and assessment of ventricular function and morphology. Atrioventricular valve annulus diameter could be assessed in 13 of 15 cases. Ventricular function and morphology could be assessed in all cases. In one case where fetal CMR could adequately visualize cardiac anatomy and function, there was still uncertainty regarding outcome due to an underdeveloped mitral valve and left ventricular lateral wall hypokinesia. The assessment of biventricular versus univentricular outcome was correct in 11 of the 12 remaining cases. Figure 4.15 shows a case from this category.

In borderline left ventricle, unbalanced atrioventricular defect and pulmonary atresia with intact ventricular septum, one of the cardiac ventricles is underdeveloped and may not be able to sustain adequate postnatal circulation [76–80]. Therefore, surgical establishment of a functionally univentricular circulation may be necessary. The decision to proceed with univentricular or biventricular circulation is based on the function and morphology of the underdeveloped ventricle [76, 77, 79, 81]. While this decision is based on postnatal examination, prenatal prediction of biventricular versus univentricular outcome can provide valuable information for parental counseling. Furthermore, current prediction models are not perfect, which may explain the incorrect prediction in one case in this study. Future studies are warranted to find improved prediction models.

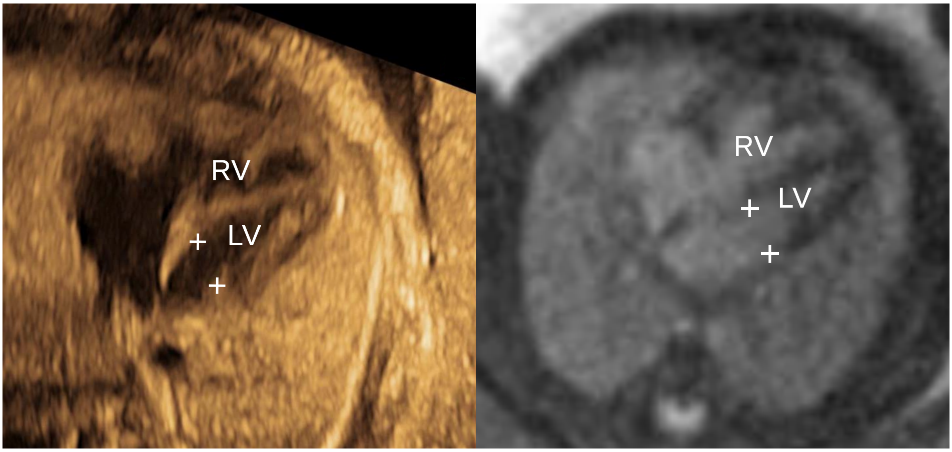

Figure 4.15: Prediction of uni- versus biventricular outcome. Borderline left ventricle was suspected at fetal ultrasound examination **(left)**¸ where mitral valve annulus diameter was estimated to be 5.6 mm. Fetal CMR estimated mitral valve annulus diameter to be 9.4 mm **(right)**. Therefore, biventricular outcome was suggested based on CMR findings and was confirmed postnatally. Crosses indicate the diameter of the mitral annulus. LV, left ventricle; RV, right ventricle. *Modified and used with permission from Ryd et al. "Utility of Fetal Cardiovascular Magnetic Resonance for Prenatal Diagnosis of Complex Congenital Heart Defects". JAMA Network Open 2021. American medical association. https://doi.org/10.1001/jamanetworkopen.2021.3538 – CC-BY license.*

Assessment of signs of restrictive atrial septum

This category included four patients with hypoplastic left heart syndrome (see cases 5, 11, 28 and 31 in Supplementary Table 1 in the Appendix). In one case, the interatrial communication could not be assessed by ultrasound due to poor acoustic windows. A large interatrial communication was demonstrated by fetal CMR, and no signs of the nutmeg lung pattern were present. Delivery was originally planned as caesarean section with preparedness for cardiac catheterization, however the information from fetal CMR changed delivery planning to vaginal delivery without preparedness for cardiac catheterization (Figure 4.16). In another case, fetal CMR similarly showed a sufficient interatrial communication and no signs of the nutmeg lung pattern, which led to a similar change in delivery planning. In the third case, fetal ultrasound showed signs of restrictive atrial septum. Fetal CMR showed no signs of the nutmeg lung pattern. Postnatally, a restrictive atrial septum was confirmed, although without signs of pulmonary vascular disease. In the fourth and final case, fetal ultrasound showed a univentricular heart, raising suspicion for hypoplastic left heart syndrome. However, maternal obesity hampered ultrasound examination, and neither the interatrial communication nor the connections of the great vessels to the heart could be visualized. Fetal CMR confirmed the suspicion of hypoplastic left heart syndrome. Furthermore, fetal CMR showed a sufficient interatrial communication, at least two pulmonary veins connecting normally to the left atrium, and normal connections of the main pulmonary artery to the right ventricle and aorta to the left ventricle respectively. In this case, fetal CMR changed the plan for delivery from caesarean section with preparedness for cardiac catheterization to vaginal delivery without preparedness for cardiac catheterization.

In hypoplastic left heart syndrome, the survival of the newborn requires a left-to-right atrial shunt and patency of the arterial duct [82]. If the atrial shunt is insufficient due to restrictive or intact atrial septum, immediate cardiac intervention is needed after birth [82–84]. In those cases, it is critical to perform a planned caesarean section with preparedness for cardiac catheterization. However, if there are signs of pulmonary lymphangiectasia as indicated by the nutmeg lung pattern, the infant is unlikely to survive, and vaginal delivery may be recommended to avoid unnecessary risks associated with caesarean section. This study demonstrates that fetal CMR can provide important diagnostic information with direct impact on clinical management in fetuses with hypoplastic left heart syndrome.

Parental counseling

In 21 cases, parental counseling was improved due to diagnostic information from fetal CMR (see cases 2-4, 6, 8, 11-13, 16, 18, 19-21, 23-29 and 31 in Supplementary Table 1 in the Appendix). With a more definitive diagnosis, parents were given more accurate expectations regarding outcome and postnatal clinical management. In hypoplastic left heart syndrome with suspected restrictive atrial septum, a better prognosis was suggested by the absence of the nutmeg lung pattern. This offered hope and was important for the decision to recommend caesarean section with the cardiac catheterization team on standby.

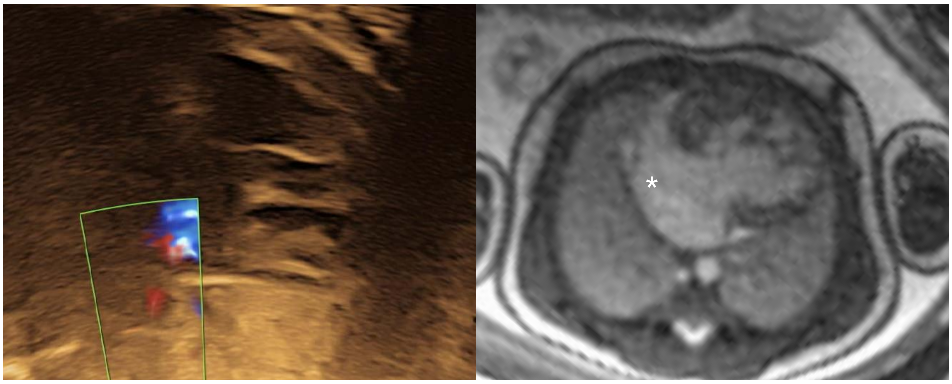

Figure 4.16: Evaluation of the interatrial communication in hypoplastic left heart syndrome. Neither the atrial septum nor Doppler flow across could be visualized by fetal ultrasound (**left**). A large interatrial communication (asterisk) was demonstrated by fetal CMR (**right**). *Modified and used with permission from Ryd et al. "Utility of Fetal Cardiovascular Magnetic Resonance for Prenatal Diagnosis of Complex Congenital Heart Defects". JAMA Network Open 2021. American medical association. https://doi.org/10.1001/jamanetworkopen.2021.3538 – CC-BY license.*

Furthermore, additional diagnostic information could potentially allow parents to feel more comfortable with the choice of delivery center whether delivery is planned at a tertiary center or a local hospital.

Summary

This study investigated the clinical utility of fetal CMR in cases where diagnostic questions remained after fetal cardiac ultrasound performed by a pediatric cardiologist. Fetal CMR added diagnostic information in the majority of cases, in some cases with a direct impact on clinical management.

4.4 Study IV - Super-resolution image reconstruction for fetal CMR

Figure 4.17 shows reconstructed low-resolution fetal cardiac cine images compared to the fully sampled standard image. Figure 4.18 shows qualitative image scores by observers 1 – 3 for each reconstruction method versus the fully sampled standard clinical images. For observers 1 and 2, the phasrGAN and phasrresnet methods showed no statistically significant difference in image quality versus the fully sampled standard clinical images for phase-resolutions down to 33%. For observer 3, the phasrGAN method showed no statistically significant difference in image quality versus the fully sampled standard clinical images for phase-resolutions down to 33%, whereas the phasrresnet method showed statistically significantly lower image quality for 33% phase-resolution but not for 50% phase-resolution. No unexpected pathology was found in any of the reconstructed images, and pathology in the standard clinical images was also found in all reconstructed images. Artifacts were seen in the descending aorta in 4% of images, and in one case, the atrial septum showed an unrealistic motion in all reconstructed images. There were no statistically significant differences between the phasrGAN and phasrresnet methods with respect to MSE or PSNR, whereas for SSIM the phasrresnet method showed statistically significantly higher values compared to the phasrGAN method at 25% and 33% phase resolution (Figures 15-17).

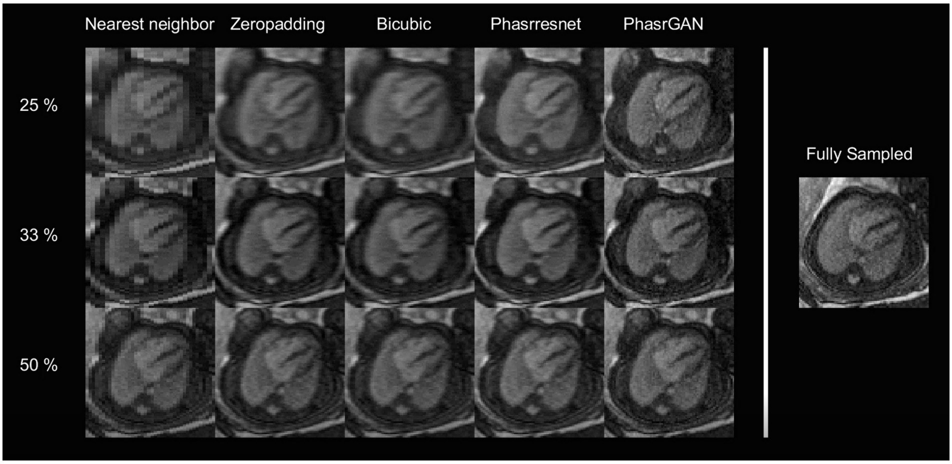

Figure 4.17: Reconstructed low-resolution fetal CMR images. The four leftmost columns show reconstruction methods, and rows represent low-resolution input images with 25%, 33% and 50% phase resolution respectively. The rightmost column shows the fully sampled standard clinical image. *Used with permission from Berggren et al. "Super-Resolution Cine Image Enhancement for Fetal Cardiac Magnetic Resonance Imaging". Journal of Magnetic Resonance Imaging 2021. John Wiley and Sons. https://doi.org/10.1002/jmri.27956 – CC BY-NC 4.0 license (https://creativecommons.org/licenses/by-nc/4.0/).*

This study proposed two models based on artificial neural networks to increase image resolution in fetal CMR images with a shortened acquisition time. For the phasrGAN method, no statistically significant differences in image quality were seen in reconstructed images for phase resolutions down to 33% of the fully sampled standard clinical images, corresponding to a threefold accelerated image acquisition. While beyond the scope of this study, it would be of interest to compare the performance of the proposed methods to alternative accelerated imaging methods such as compressed sensing, as has been suggested for fetal CMR [85, 86]. The accelerated image acquisition achieved using the proposed methods may lead to increased chances of successful fetal CMR examination, as fetal motion during image acquisition is less likely with a shorter acquisition time. However, the risk of neural networks introducing nonexistent pathology or removing pathology should be considered. Even small perturbations of input images previously unseen by the network, such as pathology or artifacts, can cause significant errors in reconstructed images [87]. In the absence of an acquired high-resolution image for comparison, such errors may be difficult to detect. Therefore, clinical implementation requires prior validation in a large number of cases including a variety of congenital heart defects.

	Phase-encoding resolution			
	25%	33%	50%	100%
Enhancement method and observer	Speed-up: 4 x	Speed-up: 3 x	Speed-up:2 x	Reference
Observer 1				
phasrGAN	7 [5–7]*	8 [6.5–8]$^{p=0.27}$	7 [7–8]$^{p=0.26}$	
phasrresnet	7 [6–7]*	8 [7–8]$^{p=0.43}$	7 [7–8]$^{p=0.19}$	
bicubic interpolation	5 [4.5–6.5]*	7 [6–8]*	7 [6.25–7.75]$^{p=0.06}$	
k-space zero-padding	5 [5–6.5]*	7 [6–8]*	7 [6.25–8]$^{p=0.10}$	
nearest neighbor interpolation	4 [3–5]*	6 [4.5–6.5]*	6.5 [6–7]*	
standard clinical acquisition (fully sampled)				8 [7–8.5]
Observer 2				
phasrGAN	7 [6–8]*	8 [6.5–8]$^{p=0.06}$	8 [7–9]$^{p=0.96}$	
phasrresnet	7 [6–7]*	8 [7–8.5]$^{p=0.32}$	8 [7–9]$^{p=0.38}$	
bicubic interpolation	6 [5–6.5]*	7 [6.5–8]*	8 [7–9]$^{p=0.62}$	
k-space zero-padding	6 [5–7]*	8 [7–8]*	8 [7–9]$^{p=0.55}$	
nearest neighbor interpolation	4 [3.5–4.5]*	5 [4.5–7]*	7.5 [7–8]*	
standard clinical acquisition (fully sampled)				8 [8–9]
Observer 3				
phasrGAN	6 [5.5–7]*	7 [7–8]$^{p=0.29}$	7 [6.25–8]$^{p=0.83}$	
phasrresnet	5 [4–6]*	6 [5–7]*	7 [6–8]$^{p=0.71}$	
bicubic interpolation	4 [3.5–4]*	5 [4–6]*	7 [5.25–7]$^{p=0.18}$	
k-space zero-padding	4 [3–4.5]*	5 [5–6]*	6.5 [6–7.75]$^{p=0.38}$	
nearest neighbor interpolation	2 [2–3]*	3 [3–4]*	5 [4–6]*	
standard clinical acquisition (fully sampled)				7 [6 – 8]

Figure 4.18: Image scores. The table shows image scores for observers 1 – 3, for each reconstruction method and phase resolution. Data are presented as median [IQR]. For each reconstruction method and phase resolution, image scores were compared to the fully sampled reference images using Mann-Whitney's non-parametric test. P-values < 0.05 are denoted by *. *Modified and used with permission from Berggren et al. "Super-Resolution Cine Image Enhancement for Fetal Cardiac Magnetic Resonance Imaging". Journal of Magnetic Resonance Imaging 2021. John Wiley and Sons, https://doi.org/10.1002/jmri.27956 – CC BY-NC 4.0 license (https://creativecommons.org/licenses/by-nc/4.0/).*

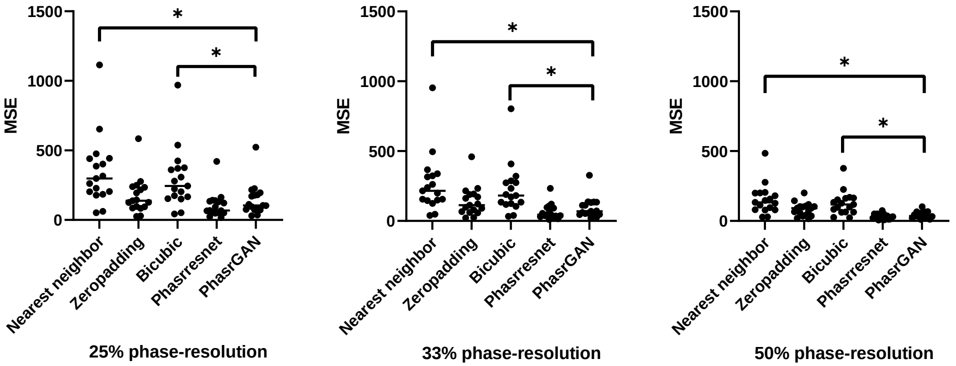

Figure 4.19: Mean squared error. Graphs show mean squared error (MSE) calculated for reconstructed synthetically created low-resolution images versus the fully sampled original images. No reconstruction method showed statistically significantly lower MSE than the phasrGAN method. Solid lines indicate medians. *Used with permission from Berggren et al. "Super-Resolution Cine Image Enhancement for Fetal Cardiac Magnetic Resonance Imaging". Journal of Magnetic Resonance Imaging 2021. John Wiley and Sons. https://doi.org/10.1002/jmri.27956 – CC BY-NC 4.0 license (https://creativecommons.org/licenses/by-nc/4.0/).*

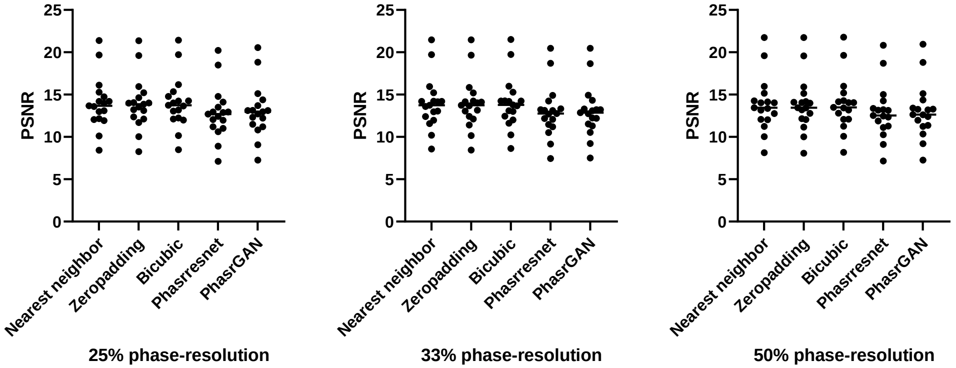

Figure 4.20: Peak signal to noise ratio. Graphs show peak signal to noise ratio (PSNR) calculated for reconstructed synthetically created low-resolution images versus the fully sampled original images. No reconstruction method showed statistically significantly higher PSNR than the phasrGAN method. Solid lines indicate medians. *Used with permission from Berggren et al. "Super-Resolution Cine Image Enhancement for Fetal Cardiac Magnetic Resonance Imaging". Journal of Magnetic Resonance Imaging 2021. John Wiley and Sons. https://doi.org/10.1002/jmri.27956 – CC BY-NC 4.0 license (https://creativecommons.org/licenses/by-nc/4.0/).*

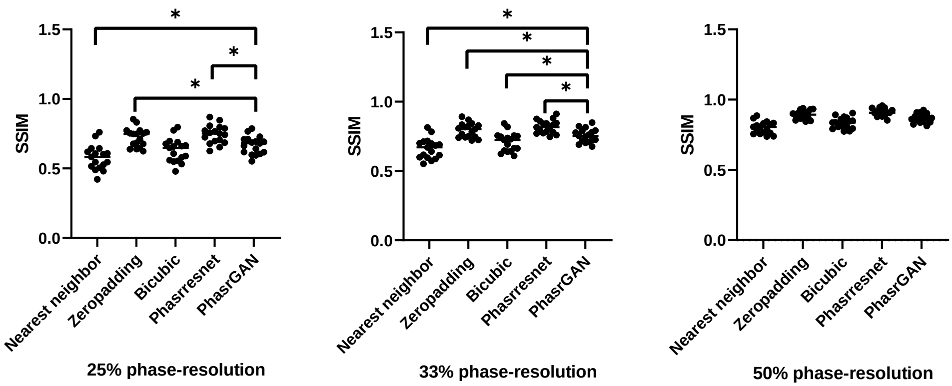

Figure 4.21: Structural similarity index measure. Graphs show structural similarity index measure (SSIM) calculated for reconstructed synthetically created low-resolution images versus the fully sampled original images. The phasrresnet method showed statistically significantly higher SSIM than the phasrGAN method at 25% and 33% phase resolution. Solid lines indicate medians. *Used with permission from Berggren et al. "Super-Resolution Cine Image Enhancement for Fetal Cardiac Magnetic Resonance Imaging". Journal of Magnetic Resonance Imaging 2021. John Wiley and Sons. https://doi.org/10.1002/jmri.27956 – CC BY-NC 4.0 license (https://creativecommons.org/licenses/by-nc/4.0/).*

Summary

This study applied two artificial neural networks to increase resolution in fetal CMR images acquired with a reduced resolution and acquisition time. For the phasrGAN method, reconstructed low-resolution images showed no statistically significant differences in image quality compared to fully sampled standard clinical images for phase resolutions down to 33%, corresponding to a threefold increase in acquisition speed. The proposed methods could potentially increase the chances of successful fetal CMR examination as fetal movement is less likely during a short image acquisition.

Chapter 5

Conclusions

In this thesis, fetal cardiovascular magnetic resonance imaging techniques were applied and developed for assessment of fetal cardiovascular physiology.

The main conclusions for *Studies I - IV* are:

- I Fetal blood flow quantification using phase-contrast cardiovascular magnetic resonance gated by Doppler ultrasound is feasible.
- II Automatic fetal volume quantification from high-resolution magnetic resonance images using artificial neural networks provide accurate results versus manual measurements and saves considerable amounts of analysis time.
- III Fetal cardiovascular magnetic resonance imaging can provide additional diagnostic information with impact on clinical management and parental counseling in fetuses with congenital heart defects where diagnostic questions remain after fetal ultrasound examination.
- IV Super-resolution image reconstruction can be used to increase resolution in low-resolution fetal cardiovascular magnetic resonance cine images, thereby allowing a shorter acquisition time.

Bibliography

[1] J. M. Goplerud and M. Delivoria-Papadopoulos. “Physiology of the Placenta - Gas Exchange”. In: *Annals of clinical and laboratory science* 15 (1985).

[2] B. Y. G. S. Dawes, J. C. Mott, and J. G. Widdicombe. “The foetal circulation in the lamb”. In: *J. Physiol.* 126 (1954), pp. 563–587.

[3] A. M. Rudolph and M. A. Heymann. “Fetal and neonatal circulation and respiration.” In: *Annu. Rev. Physiol.* 36 (1974), pp. 187–207.

[4] P. J. Murphy. “The fetal circulation”. In: *Continuing Education in Anaesthesia, Critical Care and Pain* 5.4 (2005), pp. 107–112.

[5] T. Kiserud and G. Acharya. “The fetal circulation”. In: *Prenatal Diagnosis* 24.13 (2004), pp. 1049–1059.

[6] K. G. Schmidt, N. H. Silverman, and A. M. Rudolph. “Assessment of flow events at the ductus venosus-inferior vena cava junction and at the foramen ovale in fetal sheep by use of multimodal ultrasound”. In: *Circulation* 93.4 (1996), pp. 826–833.

[7] H. Nagasawa, C. Hamada, M. Wakabayashi, Y. Nakagawa, S. Nomura, and Y. Kohno. “Time to spontaneous ductus arteriosus closure in full-term neonates”. In: *Open Heart* 3.1 (2016), e000413.

[8] M. Kondo, S. Itoh, T. Kunikata, T. Kusaka, T. Ozaki, K. Isobe, and S. Onishi. “Time of closure of ductus venosus in term and preterm neonates”. In: *Archives of Disease in Childhood* 85.1 (2001), pp. 57–59.

[9] S. U. Morton and D. Brodsky. “Fetal Physiology and the Transition to Extrauterine Life”. In: *Clinics in Perinatology* 43.3 (2016), pp. 395–407.

[10] Y. Singh and C. Tissot. “Echocardiographic evaluation of transitional circulation for the neonatologists”. In: *Frontiers in Pediatrics* 6.May (2018).

[11] A. M. Rudolph. “The changes in the circulation after birth. Their importance in congenital heart disease.” In: *Circulation* 41.2 (1970), pp. 343–359.

[12] D. van der Linde, E. E. Konings, M. A. Slager, M. Witsenburg, W. A. Helbing, J. J. Takkenberg, and J. W. Roos-Hesselink. “Birth Prevalence of Congenital Heart Disease Worldwide A Systematic Review and Meta-Analysis”. In: *Journal of the American College of Cardiology* 58.21 (2011), pp. 2241–2247.

[13] M. S. Minette and D. J. Sahn. “Ventricular Septal Defects”. In: *Circulation* 114 (2006), pp. 2190–2197.

[14] R. J. Sommer, Z. M. Hijazi, and J. F. Rhodes. “Pathophysiology of congenital heart disease in the adult part I: Shunt lesions”. In: *Circulation* 117.8 (Feb. 2008), pp. 1090–1099.

[15] G. Howlett. “Lung mechanics in normal infants and infants with congenital heart disease”. In: *Archives of Disease in Childhood* 47.255 (1972), pp. 707–715.

[16] P. Stanger, L. V. Russell, and J. E. Edwards. “Anatomic factors causing respiratory distress in acyanotic congenital cardiac disease”. In: *pediatrics* 43 (1969), pp. 760–769.

[17] M. Cucerea, M. Simon, E. Moldovan, M. Ungureanu, R. Marian, and L. Suciu. “Congenital Heart Disease Requiring Maintenance of Ductus Arteriosus in Critically Ill Newborns Admitted at A Tertiary Neonatal Intensive Care Unit”. In: *The Journal of Critical Care Medicine* 2.4 (2016), pp. 185–191.

[18] D. M. Bardo, D. G. Frankel, K. E. Applegate, D. J. Murphy, and R. P. Saneto. “Hypoplastic Left Heart Syndrome”. In: *RadioGraphics* 21 (2001), pp. 705–717.

[19] S. Akkinapally, S. G. Hundalani, M. Kulkarni, C. J. Fernandes, A. G. Cabrera, B. Shivanna, and M. Pammi. “Prostaglandin E1 for maintaining ductal patency in neonates with ductal-dependent cardiac lesions”. In: *Cochrane Database of Systematic Reviews* 2018.2 (2018).

[20] A. Levery, J. S. Glickstein, C. S. Kleinman, S. M. Levasseur, J. Chen, W. M. Gersony, and I. A. Williams. “The Impact of Prenatal Diagnosis of Complex Congenital Heart Disease on Neonatal Outcomes”. In: *Pediatr Cardiol.* 31 (2010), pp. 587–597.

[21] G. Satomi, S. Yasukochi, T. Shimizu, K. Takigiku, and T. Ishii. “Has fetal echocardiography improved the prognosis of congenital heart disease ? Comparison of patients with hypoplastic left heart syndrome with and without prenatal diagnosis”. In: *Pediatrics international* 41 (1999), pp. 728–732.

[22] A. Chakraborty, S. R. Gorla, and S. Swaminathan. “Impact of prenatal diagnosis of complex congenital heart disease on neonatal and infant morbidity and mortality”. In: *Prenatal Diagnosis* 38 (2018), pp. 958–963.

[23] B. Holland, J. Myers, and C. W. Jr. “Prenatal diagnosis of critical congenital heart disease reduces risk of death from cardiovascular compromise prior to planned neonatal cardiac surgery : a meta-analysis”. In: *Ultrasound Obstet Gynecol* 45 (2015), pp. 631–638.

[24] O. Franklin, M. Burch, N. Manning, K. Sleeman, S. Gould, and N. Archer. “Prenatal diagnosis of coarctation of the aorta improves survival and reduces morbidity”. In: *Heart* 87 (2002), pp. 67–69.

[25] L. D. Allan and I. C. Huggon. “Counselling following a diagnosis of congenital heart disease”. In: *Prenatal Diagnosis* 24.13 (2004), pp. 1136–1142.

[26] R. Lytzen, N. Vejlstrup, and J. Bjerre. “Live-Born Major Congenital Heart Disease in Denmark Incidence, Detection Rate, and Termination of Pregnancy Rate From 1996 to 2013”. In: *JAMA cardiology* 3.9 (2018), pp. 829–837.

[27] R. W. Gill. “Measurement of blood flow by ultrasound: Accuracy and sources of error”. In: *Ultrasound in Medicine & Biology* 11.4 (July 1985), pp. 625–641.

[28] B. Gruber, M. Froeling, T. Leiner, and D. W. Klomp. “RF coils: A practical guide for nonphysicists”. In: *Journal of Magnetic Resonance Imaging* 48.3 (2018), pp. 590–604.

[29] S. S. Hidalgo-Tobon. “Theory of gradient coil design methods for magnetic resonance imaging”. In: *Concepts in Magnetic Resonance Part A: Bridging Education and Research* 36.4 (2010), pp. 223–242.

[30] L. G. Hanson. “Is Quantum Mechanis Necessary for Understanding Magnetic Resonance?” In: *Concepts in Magnetic Resonance Part A: Bridging Education and Research* 32A (2008), pp. 329–340.

[31] G. B. Chavhan, P. S. Babyn, B. Thomas, M. M. Shroff, and E. Mark Haacke. “Principles, techniques, and applications of T2*-based MR imaging and its special applications”. In: *Radiographics* 29.5 (2009), pp. 1433–1449.

[32] F. Bloch. “Nuclear induction”. In: *Physical Review* 70.7-8 (1946), pp. 460–474.

[33] P. Mansfield and A. A. Maudsley. “Medical imaging by NMR”. In: *British Journal of Radiology* 50.591 (1977), pp. 188–194.

[34] W. A. Edelstein, J. M. Hutchison, G. Johnson, and T. Redpath. “Spin warp NMR imaging and applications to human whole-body imaging”. In: *Physics in Medicine and Biology* 25.4 (1980), pp. 751–756.

[35] P. Lanzer, C. Barta, E. H. Botvinick, H. U. Wiesendanger, G. Modin, and C. B. Higgins. “ECG-synchronized cardiac MR imaging: method and evaluation.” In: *Radiology* 155.3 (June 1985), pp. 681–686.

[36] D. J. Bryant, J. A. Payne, D. N. Firmin, and D. B. Longmore. “Measurement of flow with nmr imaging using a gradient pulse and phase difference technique”. In: *Journal of Computer Assisted Tomography* 8.4 (1984), pp. 588–593.

[37] G. L. Nayler, D. N. Firmin, and D. B. Longmore. “Blood flow imaging by cine magnetic resonance”. In: *Journal of Computer Assisted Tomography* 10.5 (1986), pp. 715–722.

[38] J. Lotz, C. Meier, A. Leppert, and M. Galanski. “Cardiovascular Flow Measurement with Phase-Contrast MR Imaging: Basic Facts and Implementation”. In: *RadioGraphics* 22.3 (2002), pp. 651–671.

[39] H. Körperich, J. Gieseke, P. Barth, R. Hoogeveen, H. Esdorn, A. Peterschröder, H. Meyer, and P. Beerbaum. “Flow Volume and Shunt Quantification in Pediatric Congenital Heart Disease by Real-Time Magnetic Resonance Velocity Mapping: A Validation Study”. In: *Circulation* 109.16 (2004), pp. 1987–1993.

[40] P. Beerbaum, H. Körperich, J. Gieseke, P. Barth, M. Peuster, and H. Meyer. “Blood flow quantification in adults by phase-contrast MRI combined with SENSE - A validation study”. In: *Journal of Cardiovascular Magnetic Resonance* 7.2 (2005), pp. 361–369.

[41] J. Lotz, R. Döker, R. Noeske, M. Schüttert, R. Felix, M. Galanski, M. Gutberlet, and G. P. Meyer. “In vitro validation of phase-contrast flow measurements at 3 T in comparison to 1.5 T: Precision, accuracy, and signal-to-noise ratios”. In: *Journal of Magnetic Resonance Imaging* 21.5 (2005), pp. 604–610.

[42] H. Arheden, M. Saeed, E. Trnqvist, G. Lund, M. F. Wendland, C. B. Higgins, and F. Sthlberg. “Accuracy of segmented MR velocity mapping to measure small vessel pulsatile flow in a phantom simulating cardiac motion”. In: *Journal of Magnetic Resonance Imaging* 13.5 (2001), pp. 722–728.

[43] H. Arheden, C. Holmqvist, U. Thilen, K. Hanséus, G. Björkhem, O. Pahlm, S. Laurin, and F. Ståhlberg. “Left-to-right cardiac shunts: comparison of measurements obtained with MR velocity mapping and with radionuclide angiography.” In: *Radiology* 211.2 (1999), pp. 453–458.

[44] Z. J. Wang, G. P. Reddy, M. B. Gotway, B. M. Yeh, and C. B. Higgins. “Cardiovascular Shunts: MR Imaging Evaluation”. In: *Radiographics* 23 (2003), pp. 181–194.

[45] P. Garg, A. J. Swift, L. Zhong, C. J. Carlhäll, T. Ebbers, J. Westenberg, M. D. Hope, C. Bucciarelli-Ducci, J. J. Bax, and S. G. Myerson. “Assessment of mitral valve regurgitation by cardiovascular magnetic resonance imaging”. In: *Nature Reviews Cardiology* 17.5 (2020), pp. 298–312.

[46] C. Tang, D. D. Blatter, and D. L. Parker. “Accuracy of phase⌧contrast flow measurements in the presence of partial⌧volume effects”. In: *Journal of Magnetic Resonance Imaging* 3.2 (1993), pp. 377–385.

[47] R. L. Wolf, R. L. Ehman, S. J. Riederer, and P. J. Rossman. “Analysis of systematic and random error in MR volumetric flow measurements”. In: *Magnetic Resonance in Medicine* 30.1 (1993), pp. 82–91.

[48] K. R. O'Brien, B. R. Cowan, M. Jain, R. A. Stewart, A. J. Kerr, and A. A. Young. "MRI phase contrast velocity and flow errors in turbulent stenotic jets". In: *Journal of Magnetic Resonance Imaging* 28.1 (2008), pp. 210–218.

[49] M. P. Rolf et al. "Sequence optimization to reduce velocity offsets in cardiovascular magnetic resonance volume flow quantification - A multi-vendor study". In: *Journal of Cardiovascular Magnetic Resonance* 13.1 (2011), pp. 1–10.

[50] J. W. Lankhaar, M. B. Hofman, J. T. Marcus, J. J. Zwanenburg, T. J. Faes, and A. Vonk-Noordegraaf. "Correction of phase offset errors in main pulmonary artery flow quantification". In: *Journal of Magnetic Resonance Imaging* 22.1 (2005), pp. 73–79.

[51] J. Nickander, M. Lundin, G. Abdula, J. Jenner, E. Maret, P. Sörensson, E. Heiberg, A. Sigfridsson, and M. Ugander. "Stationary tissue background correction increases the precision of clinical evaluation of intra-cardiac shunts by cardiovascular magnetic resonance". In: *Scientific Reports* 10.1 (2020), pp. 1–8.

[52] M. S. Jansz, M. Seed, J. F. P. Van Amerom, D. Wong, L. Grosse-Wortmann, S. J. Yoo, and C. K. MacGowan. "Metric optimized gating for fetal cardiac MRI". In: *Magnetic Resonance in Medicine* 64.5 (2010), pp. 1304–1314.

[53] F. Kording, J. Yamumura, C. Much, G. Adam, B. Schoennagel, U. Wedegärtner, and F. Ueberle. "Evaluation of an MR compatible Doppler-ultrasound device as a new trig- ger method in Cardiac MRI: a quantitative comparison to ECG". In: *Biomed Tech* 58.1 (2013).

[54] F. Kording et al. "Dynamic fetal cardiovascular magnetic resonance imaging using Doppler ultrasound gating". In: *Journal of Cardiovascular Magnetic Resonance* 20.1 (2018), pp. 1–10.

[55] Y. Kacem et al. "Fetal Weight Estimation : Comparison of Two-dimensional US and MR Imaging Assessments". In: *Radiology* 267.3 (2013).

[56] F. Kording, B. P. Schoennagel, M. Tavares De Sousa, K. Fehrs, G. Adam, J. Yamamura, and C. Ruprecht. "Evaluation of a Portable Doppler Ultrasound Gating Device for Fetal Cardiac MR Imaging: Initial Results at 1.5T and 3T". In: *Magn Reson Med Sci* XX (2018), pp. 1–10.

[57] P. Van Leeuwen, L. Werner, Z. Hilal, S. Schiermeier, W. Hatzmann, and D. Grönemeyer. "Fetal electrocardiographic measurements in the assessment of fetal heart rate variability in the antepartum period". In: *Physiological Measurement* 35.3 (2014), pp. 441–454.

[58] P. Van Leeuwen, K. M. Gustafson, D. Cysarz, D. Geue, L. E. May, and D. Grönemeyer. "Aerobic exercise during pregnancy and presence of fetal-maternal heart rate synchronization". In: *PLoS ONE* 9.8 (2014).

[59] O. Ronneberger, P. Fischer, and T. Brox. “U-Net: Convolutional Networks for Biomedical Image Segmentation”. In: *Medical Image Computing and Computer-Assisted Intervention – MICCAI 2015*. Ed. by N. Navab, J. Hornegger, W. M. Wells, and A. F. Frangi. Cham: Springer International Publishing, 2015, pp. 234–241.

[60] A. Nilsson. “Quantification of fetal volume in magnetic resonance images using deep learning”. In: *Master’s Theses in Mathematical Sciences. 2021. Mathematics. Faculty of Engineering, Lund University. URL: http://lup.lub.lu.se/student-papers/record/9043734* ().

[61] F. Navarro, S. Shit, I. Ezhov, J. Paetzold, A. Gafita, J. C. Peeken, S. E. Combs, and B. H. Menze. “Shape-Aware Complementary-Task Learning for Multi-organ Segmentation”. In: *Lecture Notes in Computer Science (including subseries Lecture Notes in Artificial Intelligence and Lecture Notes in Bioinformatics)* 11861 LNCS (2019), pp. 620–627.

[62] F. P. Hadlock, R. B. Harrist, R. S. Sharman, R. L. Deter, and S. K. Park. “Estimation of fetal weight with the use of head, body, and femur measurements-A prospective study”. In: *American Journal of Obstetrics and Gynecology* 151.3 (1985), pp. 333–337.

[63] F. P. Hadlock, R. B. Harrist, R. J. Carpenter, R. L. Deter, and S. K. Park. “Sonographic estimation of fetal weight. The value of femur length in addition to head and abdomen measurements”. In: *Radiology* 150.2 (1984), pp. 535–540.

[64] D. Saul, K. Degenhardt, S. D. Iyoob, L. F. Surrey, A. M. Johnson, M. P. Johnson, J. Rychik, and T. Victoria. “Hypoplastic left heart syndrome and the nutmeg lung pattern in utero : a cause and effect relationship or prognostic indicator ?” In: *Pediatr radiol* 46 (2016), pp. 483–489.

[65] K. Berggren, D. Ryd, E. Heiberg, A. H. Aletras, and E. Hedström. “Super-Resolution Cine Image Enhancement for Fetal Cardiac Magnetic Resonance Imaging”. In: *Journal of Magnetic Resonance Imaging* (2021).

[66] S. M. E. Boito, N. T. C. Ursem, P. C. Struijk, T. Stijnen, and J. W. Wladimiroff. “Umbilical venous volume flow in the normally developing and growth-restricted human fetus”. In: *Ultrasound in Obstetrics and Gynecology* 19 (2002), pp. 344–349.

[67] Y. Nakai, M. Imanaka, J. Nishio, and S. Ogita. “Umbilical cord venous pulsation in normal fetuses and its incidence after 13 weeks of gestation”. In: *Ultrasound in Med. & Biol.* 21.4 (1995), pp. 443–446.

[68] S. Bidhult, J. Töger, E. Heiberg, M. Carlsson, H. Arheden, A. H. Aletras, and E. Hedström. “Independent validation of metric optimized gating for fetal cardiovascular phase-contrast flow imaging”. In: *Magnetic Resonance in Medicine* 81.1 (2018), pp. 495–503.

[69] J. Busch, S. J. Vannesjo, C. Barmet, K. P. Pruessmann, and S. Kozerke. “Analysis of temperature dependence of background phase errors in phase-contrast cardiovascular magnetic resonance”. In: *Journal of cardiovascular magnetic resonance : official journal of the Society for Cardiovascular Magnetic Resonance* 16 (2014), p. 97.

[70] G. S. Dawes, H. E. Fox, B. M. Leduc, G. C. Liggins, and R. T. Richards. “Respiratory movements and rapid eye movement sleep in the foetal lamb”. In: *The Journal of Physiology* 220.1 (1972), pp. 119–143.

[71] T. H. Hasaart and J. de Haan. “Effects of fetal breathing movements on umbilical venous blood flow in fetal lambs”. In: *European Journal of Obstetrics and Gynecology and Reproductive Biology* 20.2 (1985), pp. 121–129.

[72] A. Hammami, A. Mazer Zumaeta, A. Syngelaki, R. Akolekar, and K. H. Nicolaides. “Ultrasonographic estimation of fetal weight: development of new model and assessment of performance of previous models”. In: *Ultrasound in Obstetrics and Gynecology* 52.1 (2018), pp. 35–43.

[73] S. N. Sinha, M. L. Kardatzke, R. B. Cole, A. J. Muster, H. U. Wessel, and M. H. Paul. “Coarctation of the aorta in infancy”. In: *Circulation* 40.September (1969), pp. 385–398.

[74] I. Durand, G. Deverriere, C. Thill, A. S. Lety, C. Parrod, N. David, E. Barre, and T. Hazelzet. “Prenatal Detection of Coarctation of the Aorta in a Non-selected Population: A Prospective Analysis of 10 Years of Experience”. In: *Pediatric Cardiology* 36.6 (2015), pp. 1248–1254.

[75] A. Buyens, W. Gyselaers, A. Coumans, S. Al Nasiry, C. Willekes, D. Boshoff, J. Frijns, and I. Witters. “Difficult prenatal diagnosis : fetal coarctation”. In: *FVV IN OBGYN* 4.4 (2012), pp. 230–236.

[76] C. W. Baird, P. O. Myers, G. Marx, M. Nathan, B. T. Kalish, W. Tworetzky, P. Banka, S. M. Emani, J. E. Mayer, and P. J. Nido. “Biventricular Repair in Patients with a Borderline Left Heart”. In: *Pediatric and Congenital Cardiology, Cardiac Surgery and Intensive Care* (2014), pp. 1765–1785.

[77] A. F. Corno. “Borderline left ventricle *”. In: *European Journal of Cardio-Thoracic Surgery* 27 (2005), pp. 67–73.

[78] B. Craig. “Atrioventricular septal defect: From fetus to adult”. In: *Heart* 92.12 (2006), pp. 1879–1885.

[79] N. Yoshimura, M. Yamaguchi, H. Ohashi, Y. Oshima, S. Oka, M. Yoshida, H. Murakami, and T. Tei. “Pulmonary atresia with intact ventricular septum: Strategy based on right ventricular morphology”. In: *Journal of Thoracic and Cardiovascular Surgery* 126.5 (2003), pp. 1417–1426.

[80] J. Zheng, B. Gao, Z. Zhu, G. Shi, Z. Xu, J. Liu, and X. He. “Surgical results for pulmonary atresia with intact ventricular septum : a single-centre 15-year experience and medium-term follow-up”. In: *European Journal of Cardio-Thoracic Surgery* 50.July (2016), pp. 1083–1088.

[81] D. M. Overman, K. B. Dummer, F. X. Moga, and D. B. Gremmels. “Unbalanced Atrioventricular Septal Defect : Defining the Limits of Biventricular Repair The uAVSD Challenge : Matching”. In: *Pediatric Cardiac Surgery Annal* 16.1 (2013), pp. 32–36.

[82] U. Theilen and L. Shekerdemian. “The intensive care of infants with hypoplastic left heart syndrome”. In: *Arch Dis Child Fetal Neonatal Ed* June 2004 (2005), pp. 97–102.

[83] A. P. Vlahos, J. E. Lock, D. B. McElhinney, and M. E. van der Velde. “Hypoplastic Left Heart Syndrome With Intact or Highly Restrictive Atrial Septum Outcome After Neonatal Transcatheter Atrial Septostomy”. In: *Circulation* 109 (2004), pp. 2326–2330.

[84] Y. Kawahira, H. Kishimoto, H. Kawata, S. Ikawa, H. Ueda, T. Ueno, and T. Nakada. “Surgical Atrial Septostomy Without Cardiopulmonary Bypass”. In: *Ann Thorac Surg* 4975.95 (1996), pp. 7–9.

[85] C. W. Roy, M. Seed, and C. K. Macgowan. “Accelerated MRI of the fetal heart using compressed sensing and metric optimized gating”. In: *Magnetic Resonance in Medicine* 77.6 (2017), pp. 2125–2135.

[86] C. W. Roy, M. Seed, J. C. Kingdom, and C. K. Macgowan. “Motion compensated cine CMR of the fetal heart using radial undersampling and compressed sensing”. In: *Journal of Cardiovascular Magnetic Resonance* 19.1 (2017), pp. 1–14.

[87] V. Antun, F. Renna, C. Poon, B. Adcock, and A. C. Hansen. “On instabilities of deep learning in image reconstruction and the potential costs of AI”. In: *Proceedings of the National Academy of Sciences of the United States of America* 117.48 (2020), pp. 30088–30095.

Appendix

Supplementary Table 1. Clinical cases of fetuses with suspected complex congenital heart defects referred for fetal CMR. *Used with permission from Ryd et al. "Utility of Fetal Cardiovascular Magnetic Resonance for Prenatal Diagnosis of Complex Congenital Heart Defects". JAMA Network Open 2021. American medical association. https://doi.org/10.1001/jamanetworkopen.2021.3538 - CC BY license*

Patient	Prenatal echocardiography diagnosis	Remaining diagnostic questions to be clarified by fetal CMR	What fetal CMR answered to remaining diagnostic questions	Postnatal diagnoses	CMR was correct compared with postnatal diagnoses	Impact of fetal CMR on patient care
1	- Situs inversus. - Pulmonary atresia. - Unbalanced AVSD. -Interrupted IVC. - Bowel obstruction.	1. Infracardiac TAPVR? 2. Pulmonary lymphganciectasia? 3. Confirmation of systemic venous anomalies.	1. Not visualized (extensive fetal movement; polyhydramniosis). 2. No pulmonary lymphangiectasia or signs of severe	- Mildly obstructed TAPVR. - Pulmonary atresia. - Unbalanced AVSD.	1. – 2. Yes 3. –	Due to suspicion of already poor prognosis, an additional diagnosis of pulmonary lymphangiectasia would have led to possible delivery at hospital near home and

	- Suspected ipsilateral hepatic veins and TAPVR.		obstruction. 3. Not visualized. - Duodenal obstruction.	- Dextrocardia with situs inversus. - Extracardiac malformations (bowel obstruction).		a plan for primary palliative care would have been considered. Since no lymphangiectasia was identified, patient was delivered at tertiary care center.
2	- TGA/VSD-PS (suboptimal acoustic windows)	1. Measurement of pulmonary valve annulus to determine if arterial switch operation vs Rastelli to be performed.	1. Mildly underdeveloped pulmonary valve annulus.	- Valvular PS. - TGA - VSD	1. Yes	- Rastelli performed. - No change in patient management but improved counseling.
3	- Borderline LV (suboptimal	1. Aortic arch anatomy (hypoplasia, isthmus size).	1. Aortic arch not visualized.	- LV slightly hypoplastic with normal function.	1. – 2. Yes	Counseling concerning likelihood of biventricular outcome,

	projection of MV annulus). - VSD - Aortic arch hypoplasia? (no sagittal view by echocardiography)	2. MV annulus size (uni- vs biventricular outcome?).	2. MV annulus slightly underdeveloped (z score -2.7). → Biventricular repair may be possible. Unable to assess risk of CoA.	- MV annulus slightly underdeveloped (z score -2.3). - Aortic arch hypoplasia and CoA. (Biventricular outcome)		no further information concerning arch anatomy. No change in patient management.
4	- Aortic stenosis. - Aortic arch hypoplasia. - Borderline LV with small MV annulus and LV size.	1. MV annulus size? 2. LV size and function? (Uni- vs biventricular outcome?)	1. MV annulus normal size (z score -1.7). 2. Narrow, almost apex-forming LV with good function.	- Aortic stenosis. - CoA - No aortic arch hypoplasia. - Well functioning LV.	1. Yes 2. Yes	Counseling regarding high probability of biventricular outcome.

	(suboptimal projection)		→ Likely biventricular repair.	- Normal-sized MV annulus. (Biventricular outcome)		
5	- HLHS (difficult to visualize intracardiac anatomy)	1. Restrictive atrial septum? 2. Lymphangiectasia?	1. Large interatrial communication. 2. No lymphangiectasia.	- HLHS with large interatrial communication.	1. Yes 2. Yes	Standard-risk HLHS: vaginal delivery without cath lab on standby.
6	- Borderline LV with small MV annulus (suboptimal projection). - Unclear if arch hypoplasia/CoA	1. MV annulus size (uni- vs biventricular outcome?). 2. Aortic arch anatomy? (hypoplasia/size isthmus aortae).	1. MV annulus slightly underdeveloped (z score -2.4). 2. Arch hypoplasia (transverse arch z score -3.4). Isthmic hypoplasia (z score	- CoA - Moderate aortic arch hypoplasia. - Perimembranous VSD of moderate size.	1: Yes 2: Yes	Counseling regarding high probability of biventricular outcome and need of CoA repair.

	(no sagittal view of aortic arch obtained).		sagittal view -2.7, 3VT - 3.5). Aortic valve annulus normal-sized. → Likely aortic arch surgery. Likely biventricular repair.	- Slightly underdeveloped left-sided cardiac structures. (Biventricular outcome)		Vaginal delivery in tertiary centre with prostaglandins (standby).
7	- Suspected vascular ring (right aortic arch and left arterial duct). - However aberrant right subclavian artery not visualized.	1. Double aortic arch?	1. Right-sided arch visualized as well as left-sided duct. No visualized left arch.	- Double aortic arch with dominant right arch, diminutive left arch with atretic portion of posterior left arch. - Left-sided duct.	1. No (However, this variant of double aortic arch with atresia of the left posterior arch and a left-sided arterial	No

	- No sagittal aortic arch view obtained.				duct is challenging to differentiate from a right aortic arch with a left-sided arterial duct).	
8	Suspicion of aortic valve stenosis with stiff, echogenic left ventricular myocardium. Slightly underdeveloped	1. Aortic arch anatomy? 2. Aortic stenosis (annulus, morphology, jet)? 3. LV morphology and function? (uni- vs biventricular outcome?)	1. No arch hypoplasia or CoA. 2. Near normal aortic annulus size, central jet visualized – cannot rule out mild stenosis.	- Mildly underdeveloped MV annulus. - Mildly underdeveloped bicuspid aortic valve without stenosis.	1. Yes 2. Yes 3. Yes	Improved counseling regarding good chance for no need of intervention.

	isthmic region (suspected CoA).		3. Prominent LV wall. LV nearly apex-forming with good function. → May not require postnatal intervention.	- No arch hypoplasia or CoA. - Echogenic LV endocardium. - LV nearly apex-forming. - No need for surgery. (Biventricular outcome)		
9	- DILV - TGA - Poor visualization of	1. Subaortic stenosis (duct dependent)? 2. Aortic arch size?	1. Subaortic area not visualized. 2. No suspicion of CoA.	- DILV - TGA - No subaortic stenosis. - No CoA.	1. – 2. Yes	Prostaglandins not administered prior to first echo.

	subaortic region and arch.					
10	- VSD - Slight ventricular disproportion. - No aortic arch hypoplasia but suspected narrowing in isthmic region with flow acceleration (CoA?).	1. CoA?	1. Ascending aorta normal-sized. Difficult to visualize the transverse aortic arch and isthmus. → Unable to assess CoA.	- No CoA or arch hypoplasia.	1. –	No change in patient management.
11	- HLHS with echocardiographic suspicion of RAS	1. Pulmonary lymphangiectasia?	1. No pulmonary lymphangiectasia.	- HLHS - RAS without significant clinical	1. Yes	C-Section recommended with cath lab on standby. If

	(pathologic PV Doppler and pathologic hyperoxygenation test with decreased reactivity).			pulmonary disease.		lymphangiectasia had been seen, vaginal delivery with no standby would be recommended. Important for counseling regarding prognosis.
12	- Slight ventricular disproportion. - No arch hypoplasia. - Suspected slight narrowing in isthmus.	1. CoA?	1. No CoA.	- No aortic arch hypoplasia. - No CoA.	1. Yes	Counseling + risk stratification. Delivery at hospital closest to patient’s home.

13	- Borderline LV with underdeveloped MV annulus (suboptimal projection). - Suspected aortic arch hypoplasia and hypoplastic aortic isthmus.	1. MV annulus diameter? 2. LV size and function? (Uni- vs biventricular outcome?) 3. Aortic arch anatomy?	1. Normal-sized MVannulus (z score -0.8). 2. Good LV function. → Likely biventricular outcome. Likely no need of aortic arch intervention. 3. No aortic arch hypoplasia or CoA.	-Mildly underdeveloped left-sided cardiac structures. - No aortic arch hypoplasia. - CoA (Biventricular outcome)	1. Yes 2. Yes 3. No	Counseling regarding biventricular outcome and low risk for postnatal CoA. However, CoA did develop (false safety?).
14	- Isomerism - Dextrocardia - Unbalanced AVSD favouring the right.	1. Diameter of the left component of the common AV valve? 2. LV size	1. Left component of the common AV valve z score -2.3). 2. LV almost	- Unbalanced AVSD. - Apex-forming LV.	1. Yes 2. Yes - However, biventricular outcome not	No

	- Left SVC. - Interrupted IVC. (Poor acoustic windows, progressive increase in ventricular unbalance)	(uni- vs biventricular outcome?)	completely apex-forming. → Biventricular circulation possible.	- Left component of the common AV valve with z score -2.7. - Structural left AV valve abnormality. - Aortic valve hypoplasia. - CoA - Interrupted IVC. - Left SVC. (Univentricular outcome)	possible mainly due to structural left AV valve abnormality but also due to aortic valve hypoplasia.	
15	Suspected aortic valve stenosis	1. Aortic valve annulus?	1. Normal-sized aortic valve annulus.	- Normal-sized aortic valve.	1. Yes 2. –	No

	(narrow annulus, thickened valve). - Borderline LV. - No aortic arch hypoplasia or CoA.	2. MV annulus size (uni- vs biventricular outcome)?	2. MV annulus not visualized. → Unable to predict uni- vs biventricular outcome.	- No aortic arch hypoplasia or CoA. - Slightly underdeveloped MV annulus (Biventricular outcome).		
16	- PA-IVS - Challenging fetal position in late pregnancy.	1. Tricuspid valve annulus size? 2. RV-anatomy? (uni-vs biventricular outcome?)	1. Tricuspid valve annulus (z score -2.7). 2. Bipartite RV. → Likely biventricular outcome.	- PA-IVS - TV annulus (z score -2.1). - Hypoplastic, bipartite RV. - Normal pulmonary valve annulus.	1. Yes 2. Yes	Improved counseling regarding likely biventricular outcome.

				- No RV dependent coronary circulation demonstrated during postnatal cardiac catheterization. (Biventricular outcome)		
17	- Borderline LV with suspected marked underdevelopment of the MV annulus	1. MV annulus diameter? (uni- vs biventricular outcome?)	1. Not visualized. → Unable to predict uni- vs biventricular outcome.	- Slightly underdeveloped left-sided cardiac structures.	1. –	No change in patient management (Uncertainty regarding uni- vs biventricular outcome).

	(suboptimal projection). - Aortic arch hypoplasia and narrow isthmus (high suspicion of CoA).			- Bicuspid aortic valve. - Arch hypoplasia. - CoA (Biventricular outcome)		
18	- Slight ventricular disproportion. No arch hypoplasia but contraductal shelf (suspected CoA).	1. Aortic arch anatomy (hypoplasia/CoA)?	1. No aortic arch hypoplasia or CoA.	- No aortic arch hypoplasia or CoA.	1. Yes	Counseling Delivery in hospital closest to patient’s home possible option.
19	- Slight ventricular disproportion.	1. Aortic arch anatomy (hypoplasia/isthmic size): CoA?	1. No aortic arch hypoplasia, nomal-sized isthmus.	- Normal size of left-sided cardiac structures.	1. Yes	Counseling and planning of delivery.

	- Aortic valve, ascending aorta and aortic arch slightly underdeveloped. - Suspected narrowing in isthmic region.		→ Low risk of postnatal CoA.	- No arch hypoplasia. - Normal-sized aortic isthmus.		Delivery in hospital closest to patient’s home possible option.
20	- Unbalanced AVSD. (Poor acoustic windows due to late pregnancy and maternal obesity)	1. Degree of ventricular unbalance (uni- vs biventricular outcome?) 2. CoA? 3. VSD?	1. Mildly unbalanced AVSD with RV dominance. 2. Marked aortic arch hypoplasia. 3. No large VSD component.	- Mildly unbalanced AVSD with RV dominance. - Left component of the common AV valve with z score -2.2.	1. Yes 2. Yes 3. Yes	Counseling regarding CoA, confirmation of need of delivery at surgical center with prostaglandins available.

			- LV apex-forming with 2 papillary muscles. → Biventricular outcome likely. High risk of CoA/need for aortic surgery.	- Almost apex-forming LV with preserved function. - Small VSD. - Aortic arch hypoplasia. - CoA (Biventricular outcome)		
21	- DORV-TGA - Suspected aortic arch hypoplasia and narrow isthmus.	1. Aortic arch hypoplasia? 2. CoA?	1. Mild to moderate aortic arch hypoplasia. 2. Hypoplastic isthmus.	- DORV-TGA - Aortic arch hypoplasia. - CoA	1. Yes 2. Yes	Improved counseling regarding complexity and need for complicated biventricular repair.

	(Unable to visualize entire aortic arch)		→ High risk of postnatal CoA requiring arch reconstruction.			
22	- Mild LV hypoplasia. - Mild aortic arch hypoplasia. - Suspected narrowing of aortic isthmus.	1. Size of the aortic isthmus?	1. Narrow isthmus with potential postnatal development of CoA (z score -3.5). → May need postnatal CoA surgery.	- Slight narrowing in aortic isthmus. - No CoA. - No aortic arch hypoplasia.	1. Yes (narrowing but no CoA).	Echocardiography findings confirmed. No change in patient management.
23	- Mild LV hypoplasia. - No aortic arch hypoplasia. - Suspected narrow isthmus.	1. Aortic arch anatomy? (focus isthmic size)	1. No aortic arch hypoplasia. Slight narrowing of the aortic isthmus with low suspicion of postnatal CoA.	- Slight LV hypoplasia including MV annulus size.	1. Yes	Counseling: low suspicion of postnatal CoA. No change in patient management.

			→ Likely no need of postnatal intervention.	- No aortic arch hypoplasia or CoA.		
24	- Borderline LV with narrow MV annulus. - Suspected slight arch hypoplasia with underdeveloped isthmus. - Difficult to assess aortic arch (no sagittal arch view obtained).	1. Aortic arch anatomy? (hypoplasia, isthmic size) 2. Size of left-sided structures (MV annulus size + LV size/function)? (uni- vs biventricular outcome?).	1. No aortic arch hypoplasia, isthmus slightly hypoplastic (z score -2.1). 2. Mild LV hypoplasia (MV annulus size z score -3.4, narrow LV with good function). → Low risk of postnatal CoA. Biventricular outcome may be possible.	- No aortic arch hypoplasia. - No CoA, but slight narrowing in isthmic region. - Mild LV hypoplasia. (Biventricular outcome)	1. Yes 2. Yes	Counseling: low suspicion of CoA, biventricular outcome. Clinical assessment before discharge possible. No prostaglandins.

25	- Borderline LV with suspected postnatal univentricular outcome. - Uncertain if RAS. - Pulmonary venous return to LA not visualized. - Uncertain if aortic arch hypoplasia and/or CoA.	1. LV size and function. 2. MV annulus diameter (uni-vs biventricular outcome?). 3. Aortic arch anatomy (arch hypoplasia/isthmic size). 4. Pulmonary venous return to LA? 5. Interatrial communication: a) Diameter (RAS?) and if small b) Pulmonary lymphangiectasia?	1. Narrow LV with reduced lateral wall contractility. 2. MV annulus z score -5.4. 3. Aortic arch hypoplasia, isthmic z score -3, (high suspicion of CoA). 4. At least 2 pulmonary veins drain into LA. 5. No indirect signs of RAS. No pulmonary lymphangiectasia.	- Borderline LV with moderately underdeveloped left-sided cardiac structures. - Aortic arch hypoplasia and CoA with need of arch repair. - Bicuspid aortic valve. - Normal pulmonary venous return to LA.	1. Yes 2. Yes 3. Yes 4. Yes 5. Yes	Parental counseling: uncertain uni- vs biventricular outcome; high likelihood for postnatal CoA repair; no RAS nor lymphangiectasia nor TAPVR (improved outcome). No high-risk delivery. Vaginal delivery without cath lab on standby.

	(Late referral from other center, very poor acoustic windows)		→ Uncertainty regarding uni- vs biventricular outcome. High risk of postnatal CoA.	(Biventricular outcome)		
26	- Borderline LV with suspected moderately underdeveloped mitral and aortic valve annulus (suboptimal projection). - Suspected aortic arch hypoplasia	1. Aortic arch anatomy? (hypoplasia/isthmic size) 2. MV annulus size? 3. LV size and function? (uni- vs biventricular outcome?)	1. No arch hypoplasia, hypoplastic isthmus (z score -3) (suspicion of postnatal CoA). 2. MV annulus mildly underdeveloped (not optimally visualized). 3. Near apex-forming LV with good function.	- Mildly underdeveloped left-sided cardiac structures. - Mild aortic arch hypoplasia. - Mild CoA (follow-up: no operation yet).	1. Yes (mild CoA: but no need of postnatal operation). 2. Yes but not optimally visualized. 3. Yes	Parental counseling: high likelihood of biventricular outcome; postnatal CoA likely. No change in postnatal clinical assessment.

	and isthmal narrowing.		→ Biventricular outcome likely.	(Biventricular outcome)		
27	- Borderline LV with moderately hypoplastic mitral and aortic valve annulus: uncertain postnatal uni- vs biventricular outcome. - Aortic arch hypoplasia. - Suspected CoA.	1. MV annulus size (uni- vs biventricular outcome)? 2. CoA?	1. MV annulus mildly hypoplastic (z score -2.2). → Biventricular outcome likely. 2. Isthmus not optimally visualized, sagittal arch not visualized. → Unable to assess risk of CoA.	- Mild LV hypoplasia. - Aortic arch hypoplasia with CoA. (Biventricular outcome)	1. Yes 2. –	Counseling concerning risk of CoA but with biventricular outcome.

28	- HLHS - Unclear if RAS. - Unable to visualize aortic arch. (Poor acoustic windows)	1. Restrictive atrial communication? 2. Pulmonary lymphangiectasia? 3. Aortic arch anatomy?	1. Atrial communication with diameter 3 mm and left-to-right shunt. 2. No Pulmonary lymphangiectasia. 3. Aortic arch hypoplasia. → Low risk of restrictive atrial septum.	- HLHS without RAS. - Aortic arch hypoplasia.	1. Yes 2. Yes 3. Yes	Parental counseling. Standard-risk HLHS: vaginal delivery without cath lab on standby.
29	In another center suspected: - Unbalanced AVSD with left dominance.	1. Degree of ventricular unbalance? (uni- vs biventricular outcome?) 2. Underdeveloped PV annulus?	1. Complete AVSD with slight unbalance (favoring the left). 2. PV annulus almost normal-sized. 3. Normal-sized MPA.	- Slightly unbalanced AVSD (left dominance). - No pulmonary atresia.	1. Yes 2. Yes 3. Yes 4. – 5. –	Counseling: biventricular outcome likely. No change in patient management because

	- Pulmonary atresia with underdeveloped pulmonary branches. (poor acoustic window due to late gestation and high BMI)	3. Underdeveloped pulmonary trunk? 4. And pulmonary branch arteries? 5. Pulmonary atresia? (need of prostaglandins?)	4. Pulmonary branch arteries not visualized. 5. Flow from RV to MPA could not be confirmed. → Biventricular outcome likely.	- Well developed MPA and pulmonary branch arteries. (Biventricular outcome)		pulmonary atresia could not be ruled out prior to delivery (otherwise no prostaglandins stand-by).
30	- Heart not visualized due to high maternal BMI and anterior placenta.	1. Basic anatomical and functional assessment to rule out major CHD.	1. Normal-sized ventricles with normal systolic function. No inflow anomalies. No anomalies of outflow tracts.	- Normal cardiovascular anatomy and function.	1. Yes	Allows for delivery at hospital closest to patient’s home with non-urgent postnatal assessment.

	- Multiple risk factors for CHD.		No anomalies of great vessels. One (possibly two) visible pulmonary vein to LA.			
31	- Univentricular heart with good single ventricular function (suspected HLHS). - Impossible to visualize outflow tracts, atrial septum or connection of	1. Type of univentricular heart? 2. Pulmonary veins to LA? 3. RAS/IAS? 4. Pulmonary lymphangiectasia? 5. Anatomy and connection of outflow tracts? 6. Anatomy of aortic arch?	1. HLHS with narrow LV and VSD. 2. At least two pulmonary veins connected to LA. 3. Adequate interatrial communication. 4. No pulmonary lymphangiectasia. 5. Moderately hypoplastic aorta	- HLHS with narrow LV (aortic stenosis, mitral atresia and VSD). - Normally connected pulmonary veins to LA. - No RAS/IAS. - Moderately hypoplastic aortic	1. Yes 2. Yes 3. Yes 4. Yes 5. Yes 6. Yes	Standard risk HLHS: vaginal delivery without cath lab on standby. Improved counseling.

	pulmonary veins to LA. (Poor acoustic windows due to high maternal BMI)		connected to the LV and dilated pulmonary artery connected to the RV. 6. Moderately hypoplastic aortic arch with posterior shelf. 7. Extracardiac malformations.	valve and aortic arch with posterior shelf. - Extracardiac malformations (VACTERL association).		

Supplementary Table 1 shows prenatal echocardiography diagnosis, diagnostic questions included in the fetal CMR referral, information obtained from fetal CMR and how this compared to postnatal diagnosis. For clarity, the second to last column lists to what extent fetal CMR was correct compared with postnatal diagnoses, and the last column lists impact on patient care. *AV=atrioventricular; AVSD=atrioventricular septal defect; BMI=body mass index; CHD=congenital heart defect; CMR=cardiovascular magnetic resonance; CoA=Coarctation of the aorta; DILV=double-inlet left ventricle; DORV=double-outlet right ventricle; HLHS=hypoplastic left heart syndrome; IVC=inferior vena cava; LA=left atrium; LV=left ventricle; MPA=main pulmonary artery; MV=mitral valve; PA-IVS=pulmonary atresia with intact ventricular septum;*

PS=pulmonary stenosis; PV=pulmonary valve; RAS=restrictive atrial septum; RV=right ventricle; SVC=superior vena cava; TAPVR=total anomalous pulmonary venous return; TGA=transposition of the great arteries; VACTERL=vertebral defects, anal atresia, cardiac defects, tracheo-esophageal fistula, renal anomalies, and limb abnormalities; VSD=ventricular septal defect

Part II

Research Papers

Author contributions

	Study design	Ethical application	Data collection	Data analysis	Statistical analysis	Figures and tables	Interpretation of results	Preparation of manuscript	Revision of manuscript	Reply to reviewers
Study I	2	2	2	3	3	3	3	3	3	3
Study II	2	2	3	3	3	3	3	3	-	-
Study III	3	2	3	2	3	3	3	3	3	3
Study IV	2	2	3	3	3	2	3	3	3	3

Not applicable	-
No contribution	0
Limited contribution	1
Moderate contribution	2
Significant contribution	3